



University of
Massachusetts
Amherst

Organic Photovoltaics Based on P3HT/ PCBM: Correlating Efficiency and Morphology

Item Type	dissertation;article;dissertation
Authors	Chen, Dian
DOI	https://doi.org/10.7275/2387337
Download date	2024-08-15 16:22:01
Link to Item	https://hdl.handle.net/20.500.14394/38880

**ORGANIC PHOTOVOLTAICS BASED ON P3HT/PCBM: CORRELATING
EFFICIENCY AND MORPHOLOGY**

A Dissertation Presented

by

DIAN CHEN

Submitted to the Graduate School of the
University of Massachusetts Amherst in partial fulfillment
of the requirements for the degree of

DOCTOR OF PHILOSOPHY

September 2011

Polymer Science and Engineering

© Copyright by Dian Chen 2011

All Rights Reserved

**ORGANIC PHOTOVOLTAICS BASED ON P3HT/PCBM: CORRELATING
EFFICIENCY AND MORPHOLOGY**

A Dissertation Presented

by

DIAN CHEN

Approved as to style and content by:

Thomas P. Russell, Chair

Todd Emrick, Member

Dhandapani Venkataraman, Member

David A. Hoagland, Department Head
Polymer Science and Engineering

DEDICATION

I dedicate this dissertation to my Husband, Zhong Wang; Dad, Zhongbo Chen; Mom, Yueluo Si; Brother, Jubo Chen and his family, and my parents-in-law for their everlasting love and enthusiastic encouragement to support me in life and career.

ACKNOWLEDGMENTS

I am deeply thankful to the assistance I received from many people who have supported and contributed to my research and make this work possible.

First, I would love to thank my advisor, Prof. Thomas P. Russell, for his insightful suggestions and terrific guidance through my research projects. Tom is an outstanding advisor and he generously offered me with freedom in pursuit of various research interests and abundant research resources and collaboration opportunities, which plays a key role in the learning and progress in my career as a graduate student. His enthusiasm for research has invigorated me to investigate and complete lots of interesting topics. He is a thoughtful and energetic person, and he is an excellent role model for me in pursuit of being a great scientist.

Additionally, I would love to thank my committee members, Prof. Todd Emrick and Prof. Dhandapani Venkataraman (DV), for their thoughtful feedback and invaluable advices on my research. Their suggestions and criticisms have added substantial values to my research. I regard their sapient insight into my projects most treasurable, which helps me to advance in identification and solvation of problems.

I would also like to express my gratitude towards all the previous and current members at Russell research group for their assistance and friendship at work and in life over the past five years. I really enjoy my precious time in Russell group, which is like a big family. For my research projects, I would like to thank Jiun-tai, Wei, Yu, Feng, Atsuhiko, Soojin, Yunxia, Bokyoung, Le, Xinyu, Priyanka, Ali and *etc.*, who have been very kind and helpful in the research discussion.

I am proud and honored to study and perform research as a graduate student in the world-famous Department of Polymer Science and Engineering (PSE) at University of Massachusetts Amherst. I would like to express many thanks to all the faculty, staff and students. They are always available and willing to help. Particularly, I would like to thank Lou for the electron microscopies measurements.

I would also like to thank all the collaborators: Dr. Dongguang Wei at Carl Zeiss, Dr. Serkan Yurt, Dr. Bongsoo Kim, Brent and Zak for their valuable discussion on the projects. In addition, I would express many thanks to the beamline scientists at ALS, ORNL, APS, BNL, who gave keen support in my research projects. Especially, I would like thank Dr. Cheng Wang at ALS.

At last, I am grateful to my family, relatives and friends both in China and USA for their incessant encouragement throughout my pursuit of doctorate degree in love of science and technology.

ABSTRACT

ORGANIC PHOTOVOLTAICS BASED ON P3HT/PCBM: CORRELATING EFFICIENCY AND MORPHOLOGY

SEPTEMBER 2011

DIAN CHEN

B.E., ZHEJIANG UNIVERSITY UNIVERSITY, CHINA

M.S., ZHEJIANG UNIVERSITY UNIVERSITY, CHINA

M.S., UNIVERSITY OF MASSACHUSETTS AMHERST

Ph.D., UNIVERSITY OF MASSACHUSETTS AMHERST

Directed by: Professor Thomas P. Russell

Controlling the morphology of thin films is key in optimizing the efficiency of polymer-based photovoltaic (PV) devices. The morphology and interfacial behavior of the multicomponent active layers confined between electrodes are strongly influenced by the preparation conditions. Results obtained in this work quantitatively show the photovoltaic device performance is strongly affected by the nanoscopic morphology, crystal orientation, composition distribution and the interdiffusion behavior of the photoactive layer. To better understand the physics of the photoactive layer in the organic photovoltaic devices, it is necessary to gain a quantitative understanding of the morphology and the manner in which it develops. A key element in the kinetics associated with the structure development is the interdiffusion of the components. To that end we used poly(3-hexylthiophene)

(P3HT) / [6,6]-phenyl C₆₁-butyric acid methyl ester (PCBM) bilayers as a model to investigate the interdiffusion of the components and its role in the development of the morphology. A detailed description of the diffusion behavior and the morphology developed from a layer of P3HT in contact with a layer of PCBM during thermal annealing is given. Amorphous P3HT and PCBM are shown to be highly miscible and PCBM can penetrate into the P3HT layer through the P3HT amorphous region and form the bulk heterojunction structure within a few second of annealing at 150 °C. The results indicated that one phase is a pure P3HT crystal domain and the other phase is the mixture of amorphous P3HT and PCBM, which is not consistent with a phase separation of the components by a spinodal decomposition mechanism. We put forth an alternative mechanism, namely a competitive crystallization/diffusion argument, to describe the origin of the morphology. These findings provide new insights and guidance in the generation of active layers in organic photovoltaics that are crucial in enhancing the device performance. Textured organic solar cells were also studied, providing another route to fabricate higher performance devices.

TABLE OF CONTENT

	Page
ACKNOWLEDGMENTS	v
ABSTRACT	vii
LIST OF TABLES	xii
LIST OF FIGURES.....	xiii
LIST OF SCHEMES.....	xvii
CHAPTERS	
1. BACKGROUND	1
1.1 Overview.....	1
1.2 Polymer Semiconductors for Organic Photovoltaic Applications	1
1.3 Physics of Organic Photovoltaic Solar Cells	3
1.4 Characterization Organic Photovoltaic Solar Cells	6
1.5 Organic Solar Cell Device Structures	7
1.6 Morphology.....	12
1.7 Reference	15
2. P3HT/PCBM BULK HETEROJUNCTION ORGANIC PHOTOVOLTAICS: CORRELATING EFFICIENCY AND MORPHOLOGY	19
2.1 Introduction.....	19
2.2 Experimental.....	21
2.2.1 Materials and Methods	21
2.2.2 Organic Solar Cell Devices Making and Testing.....	21
2.2.3 Focus Ion Beam (FIB) and TEM.....	22
2.2.4 Electron Energy Loss Spectroscopy (EELS).....	23
2.2.5 Small-angle Neutron Scattering (SANS)	23
2.2.6 Grazing Incidence X-ray Ddiffraction (GIXD).....	24
2.2.7 Near Edge X-ray Absorption Fine Structure (NEXAFS)	24
2.2.8 Dynamic Secondary Ion Mass Spectrometry (DSIMS).	25
2.2.9 Differential Scanning Calorimetry (DSC)	25

2.3 Results and Discussion	25
2.3.1 UV-Vis Absorption and Device Performance at Different Preparation Conditions	25
2.3.2 Bulk Morphology of the Active Layer Thin Film and the Interfacial Behavior between the Active Layer and the Electrodes	28
2.3.3 Crystal Orientation and Size of P3HT in the Photoactive Layer.....	34
2.3.4 P3HT Crystal Orientation and PCBM Segregation at the Interface.....	38
2.3.5 Miscibility of P3HT and PCBM Measured by DSC.....	47
2.4 Conclusion	49
2.5 References.....	51
3. BULK HETEROJUNCTION PHOTOVOLTAIC ACTIVE LAYERS VIA BILAYER INTERDIFFUSION.....	55
3.1 Introduction.....	55
3.2 Experimental.....	57
3.2.1 Materials and Methods	57
3.2.2 Forward Devices	58
3.2.3 Inverted Devices	58
3.2.4 Organic Solar Cell Devices Testing.....	59
3.2.5 BF-STEM and TEM-EELS	59
3.2.6 Dynamic Secondary Ion Mass Spectrometry (DSIMS)	60
3.2.7 Small-angle Neutron Scattering (SANS)	60
3.2.8 Grazing Incidence Small Angle X-ray Scattering (GI- SAXS) and Grazing Incidence X-ray Diffraction (GIXD).....	60
3.2.9 Resonant Soft X-ray Scattering (RSoXS).....	61
3.2.10 Resonant Soft X-ray Reflectivity (RSoXR).....	61
3.3 Results and Discussion	62
3.3.1 P3HT/PCBM Bilayer Preparation.....	62
3.3.2 Interdiffusion Behavior of P3HT/PCBM Bilayer	63
3.3.3 Morphology Development from P3HT/PCBM Bilayer Diffusion	65
3.3.4 Device Performance Based on P3HT/PCBM Bilayer.....	76
3.3.5 Mechanism of P3HT/PCBM Bilayer Diffusion.....	79
3.4 Conclusion	82
3.5 References.....	83

4. P3HT NANOPILLARS AND SAWTOOTHED SURFACES FOR ORGANIC PHOTOVOLTAIC DEVICES NANOIMPRINTED BY AAO MEMBRANES AND SAPPHIRE TEMPLATES	87
4.1 Introduction.....	87
4.2 Experimental.....	89
4.2.1 Materials and Methods	89
4.2.2 The Preparation of Anodic Aluminum Oxide (AAO) Membranes.....	90
4.2.3 The Surface Modification of the Anodic Aluminum Oxide (AAO) Membranes.....	90
4.2.4 Contact Angle Measurements	90
4.2.5 Fabrication of P3HT Nanoarrays	91
4.2.6 Organic Solar Cell Devices Fabrication and Testing.....	92
4.2.7 Scanning Electron Microscopy (SEM)	93
4.2.8 Transmission Electron Microscopy (TEM)	93
4.2.9 Grazing Incidence X-ray Diffraction (GIXD).....	93
4.3 Results and Discussion	94
4.3.1 Preparation and Chracterization of the Anodic Aluminum Oxide (AAO) Membranes	94
4.3.2 Surface Modification of the AAO Templates	96
4.3.3 Preparation and Characterization of P3HT Nanostructures	98
4.3.4 Device Preparation and Testing	103
4.4 Conclusion	105
4.5 References.....	106
5. FUTURE DIRECTIONS	109
5.1 Future Directions	109
5.1.1 Textured Organic Photovoltaic Devices Based on P3HT/PCBM.....	109
5.1.2 Three Component Organic Photovoltaic Devices.....	114
5.1.3 Hybrid Photovoltaic Devices	119
5.2 References.....	121
BIBLIOGRAPHY	122

LIST OF TABLES

Table	Page
2.1 Performance of the P3HT/PCBM BHJ photovoltaic devices	28
2.2 Values of the scattering invariant (Q), the correlation length (a) and the average chords length for the P3HT-rich and PCBM-rich phases obtained under different thermal annealing conditions	34
2.3 P3HT crystal size obtained under different thermal annealing conditions	37
2.4 The near surface composition of PCBM.....	42
2.5 P3HT melting point depression with adding different amount of PCBM	48
3.1 FWHM and crystal sizes of the P3HT annealed at 150 °C for different time	69
3.2 Summary of Device Performance	78
4.1 Contact angle of the AAO membrane surface before and after surface modification	97
4.2 Device performance based on different textures.....	105
5.1 The wrinkle wavelength of P3HT: PCBM Vs the thickness of Al layer	112

LIST OF FIGURES

Figure	Page
1.1 Model of conjugated polymers and the photophysics: a , polythiophene; b , a charged polaron in polythiophene; c , hopping process between status 1 and 2; d , intra-(filled arrows) and intermolecular (unfilled arrows) charge-transport. Reprint from citation 4.....	2
1.2 a , schematic layout of a BHJ solar cell based on P3HT: PCBM; b , chemical structure of P3HT (Donor) and PCBM (Acceptor); c , the photovoltaic process.	4
1.3 Working mechanism of BHJ organic photovoltaics: a , exciton yielding; b , coulombically bound electron-hole pair yielding; c , dissociation of the electron-hole pair; d , free charge carriers transporting; e , exciton decay; f , recombination of the bound electron-hole pair and bimolecular recombination of free charge carriers (courtesy of Lambert Jan Anton Koster, University of Groningen)..	5
1.4 Typical I-V characteristics of and OPV cell in the dark (blue line) and illumination (red line) conditions. The short-circuit current density (I_{sc}) and open-circuit voltage (V_{oc}) are shown. The maximum output power (P_{max}) is given by the rectangle $I_{max} \times V_{max}$, and the power conversion efficiency η is calculated.	7
1.5 Four device architectures of conjugated polymer-based photovoltaic cells: a , single-layer OPV cell; b , bilayer OPV cell; c , disordered bulk heterojunction OPV cell; d , ordered bulk heterojunction OPV cell.	8
1.6 Defocused TEM cross-sectional images of polymer samples prepared by ultramicrotomy shows little difference for a variety of materials: a , a 1:1 by weight P3HT:PCBM blend; b , pure polystyrene. Reprint from citation 49.	13
2.1 Ultraviolet-visible absorption and EQE. a , Absorption spectra of P3HT/PCBM blend films: “As Spun”, (black line); “Pre-Annealed” 30 min, (red line); “Post-Annealed” 5 sec (blue line); “Post-Annealed” 30 min’ (green line). b , EQE spectra of P3HT/PCBM bulk heterojunction solar cells: “As Spun”, (black line); “Pre-Annealed”, (red line); “Post-Annealed” 5 sec (blue line); “Post-Annealed” 30 min (green line).	27
2.2 HRTEM of cross-sections of P3HT/PCBM based multilayered samples. a , “As Spun”; b , “Post-Annealed” 30 min heating at 150 °C. The insets represent high magnification.	30

2.3 HRTEM of cross-sections of P3HT/PCBM based multilayered samples. a , “As Spun”, inset shows the EELS of the diffusion layer; b , “Post-Annealed” heating at 150 °C	30
2.4 SANS profiles of P3HT/PCBM blend films: “As Spun”, (▲); “Pre-Annealed” 30 min (▲); “Post-Annealed” 5 sec (▲); “Post-Annealed” 30 sec (▲); “Post-Annealed” 1 min (▲); “Post-Annealed” 5 min (▲); “Post-Annealed” 30 min (▲); “Post-Annealed” 1 hr (▲). The inset represents the correlation length (a) and the scattering invariant (Q) versus the “Post-Annealing” time.....	33
2.5 GIXD curves of P3HT/PCBM blend films at different incident angles. “As Spun”; “Pre-Annealed” 30 min; “Post-Annealed” 30 min. The insets represent the schemes of edge-on and face-on of P3HT chains	36
2.6 XPS of “Post-Annealed” 30 min heating at 150 °C after removing Al with an aqueous CuCl ₂ solution	37
2.7 NEXAFS spectra of P3HT/PCBM blend films. a , AEY of “Pre-Annealed” 30 min sample; b , AEY of “Post-Annealed” 30 min sample; c , TEY of “Pre-Annealed” 30 min sample; d , TEY of “Post-Annealed” 30 min sample. The inset represents the experimental geometry: the X-rays are incident in the x - z plane with the incident angle, θ , which is measured from the sample surface. The electric field vector of the circularly polarized X-rays has two components, \vec{E}_{\parallel} (major) and \vec{E}_{\perp} . The polar angle θ of the dominant component \vec{E}_{\parallel} from the surface normal is the same as the X-ray incidence angle. Here, we use \vec{E}_{\parallel} instead of \vec{E}_{\perp} for the dominant electric field vector	40
2.8 NEXAFS spectra of P3HT/PCBM blend films and the linear fitting with the spectra of the pure PCBM and P3HT. a , TEY spectra of pure P3HT and PCBM at different incident angles; b-c , TEY spectra of the “As Spun” sample and the fitting curves at different incident angles; d-e , TEY spectra of the “Pre-Annealed” 30 min at 150 °C sample and the fitting curves at different incident angles; f-g , TEY spectra of the “Post-Annealed” 30 min at 150 °C sample and the fitting curves at different incident angles.....	41
2.9 DSIMS of the P3HT/deuterated PCBM blend films. a , “As Spun”; b , “Pre-Annealed” 30 min; c , “Post-Annealed” 5 sec; d , “Post-Annealed” 30 min; ‘S signal’ (red line); ‘D signal’ (black line). e , P3HT/PCBM bilayer diffusion at 150 °C at different time: 0 sec (black), 5 sec (red), 5 min (blue), ‘S signal’ (open circle); ‘D signal’ (solid line).....	46
2.10 DSIMS of the P3HT/deuterated PCBM blend film on a silicon substrate annealed at 150 °C for 30 min. ‘S signal’ (red line); ‘D signal’ (black line).....	47

2.11 Plot of $\frac{1}{V_L} \left[\frac{1}{T_m} - \frac{1}{T_m^0} \right]$ as a function of $\frac{V_L}{T_m}$ for the P3HT/PCBM, where T_m is the melting point of the mixtures and T_m^0 is the equilibrium melting point of pure P3HT.....	49
3.1 DSIMS of P3HT/dPCBM bilayer diffusion at 150 °C at different time a , “As Spun” P3HT/PCBM bilayer (after Figure 6e of ref 28); b , “Pre-Annealed” P3HT /PCBM bilayer; Annealed at 150 °C: 0 sec (black), 5 sec (red), 5 min (blue), ‘S signal’ (solid star); ‘D signal’ (solid line).....	65
3.2 TEM of cross-sections of “As Spun” P3HT/PCBM bilayer diffusion at 150 °C for different time. a , Bright field STEM, annealed for “0 s”; b , Bright field STEM, annealed for “5 s”; c , S core loss image, annealed for “5 s”; d , C core loss image, annealed for “5 s”; e , Overlap image of image “c” and “d”.....	66
3.3 GIXD curves of P3HT/PCBM bilayers annealed at 150 °C for different time. “Pure P3HT layer”; “As Spun” P3HT/PCBM bilayer; “Pre-Annealed” P3HT/PCBM bilayer. a , Incident angle = 0.18°; b , Incident angle = 0.12°	69
3.4 GISAXS, R-SoXS, RSoXR of P3HT/PCBM bilayer and P3HT/PCBM blend annealed at 150 °C at different time. a , GISAXS of “As Spun” P3HT/PCBM bilayer; b , GISAXS of “Pre-Annealed” P3HT/PCBM bilayer; c , GISAXS of P3HT:PCBM blend; d , R-SoXS of “As Spun” P3HT/PCBM bilayer; e , R-SoXS of “Pre-Annealed” P3HT/PCBM bilayer; f , R-SoXS of P3HT:PCBM blend; g , RSoXR of “As Spun” P3HT/PCBM bilayer; h , RSoXR of “Pre-Annealed” P3HT/PCBM bilayer; i , RSoXR of P3HT:PCBM blend; Annealed at 150 °C: 0 sec (black), 5 sec (red), 5 min (blue).....	73
3.5 SANS profiles of “As Spun” P3HT/PCBM bilayer diffusion at 150 °C at different time. “0 s”, (black triangle); 5 sec (red triangle); 5 min (blue triangle).....	75
3.6 Surface roughness of PCBM film (AFM).....	75
3.7 Devices based on P3HT/PCBM bilayer: a , Forward devices; b , Inverted devices.....	77
3.8 Dark currents based on P3HT/PCBM bilayer after different thermal annealing time at 150 °C.....	78
4.1 Al sheet and AAO membrane: a , Al surface before grinding; b , Al surface after grinding; c , SFM image of the prepared AAO membrane (2nd anodization time 1 min); d , SEM image of the prepared AAO membrane. The inset represent the side view of the AAO membrane.....	95
4.2 Nanopore length growth rate in the AAO template	96

4.3 Telescopic graphs of H ₂ O on AAO membrane surface before and after surface modification: a , original AAO membrane (static); b , original AAO membrane (advancing); c , silicone modified AAO membrane (static); d , silicone modified AAO membrane (advancing); e , silicone modified AAO membrane (receding)	97
4.4 Optical microscope images of the surface of the arrays of P3HT nanopillars: a , the surface by AAO dissolving method; b , the surface by NIL	99
4.5 Micrographs of free-standing P3HT nanostructures: a , SFM of the free-standing P3HT pillars (D =50 nm); b , SEM of the free-standing P3HT pillars; c , TEM of the free-standing P3HT pillars; d , SFM of the P3HT film with the saw tooth pattern	100
4.6 Micrographs of free-standing P3HT nanopillars: a , SFM of the free-standing P3HT pillars (D =30 nm); b , TEM of the free-standing P3HT pillars; c , SEM of the free-standing P3HT pillars	101
4.7 Micrographs of free-standing P3HT:PCBM nanopillars: a , SFM of the free-standing P3HT:PCBM pillars (D =50 nm); b , SEM of the free-standing P3HT:PCBM pillars.....	102
4.8 GIXD of the free-standing nanopillars: a , GIXD 2D image for the pure P3HT arrays (D= ~50 nm); b , GIXD 2D image for the P3HT:PCBM (1:1) arrays (D= ~50 nm); c , The out-of-plane 1-D profile of a and b	103
4.9 J-V curve of the devices based on different textures	104
5.1 P3HT saw-tooth pattern preparation: a , scheme of the sawtooth pattern preparation procedure; b , SFM height image of P3HT sawtooth pattern; c , the light reflection in the active layer based on the different surface (flat surface and textured surface).....	110
5.2 OM images (after dissolving Al): a , (P3HT/PCBM)/80 nm Al annealed at 150 °C for 30 min; b , (P3HT/PCBM)/60 nm Al annealed at 150 °C for 30 min; c , (P3HT/PCBM)/40 nm Al annealed at 150 °C for 30 min; (P3HT/PCBM)/30 nm Al annealed at 150 °C for 30 min.....	112
5.3 SFM height images: a , (P3HT/PCBM)/60 nm Al annealed at 150 °C for 30 min (after dissolving Al); b , (P3HT/PCBM)/60 nm Al annealed at 150 °C for 30 min (with Al); c , In-situ 3-D SFM image of (P3HT/PCBM)/60 nm Al annealed at 150 °C for 6 min (with Al)	114

LIST OF SCHEMES

Scheme	Page
3.1 Schematic diagram of preparation of P3HT/PCBM bilayer	63
3.2 Schematic diagram of the mechanism of P3HT/PCBM bilayer diffusion: a , “As Spun” P3HT/PCBM bilayer; b , P3HT crystallizes after short time thermal annealing; c , PCBM diffuses into P3HT film through the P3HT amorphous domains	81
4.1 The procedure for the nanostructured organic photovoltaic device	94
5.1 Chemical structure of PCPDTBT, P3HT and PCBM	116
5.2 Preparation of the random structure from the PCBM/P3HT/PCPDTBT mixture	117
5.3 Preparation of the gradient structure from the PCBM/P3HT/PCPDTBT trilayer	117
5.4 Preparation of the bilayer structure from the crosslinked P3HT/PCPDTBT/PCBM trilayer	118
5.5 Schematic of TiO ₂ nanotube array assembled with modified C ₆₀ , and used for photovoltaic application	120

CHAPTER 1

BACKGROUND

1.1 Overview

As the need for renewable, “green” energy sources becomes more urgent, more and more attention was paid on photovoltaic energy conversion, especially organic photovoltaics (OPVs) made from conjugated polymers. Organic solar cells based on thin polymer films are attractive due to their mechanical flexibility, ease of processing, and low cost fabrication of large area devices.¹ Additionally, their physical properties can be chemically tuned to adjust separately the band gap, the valence and conduction energies, charge transport, as well as the solubility and morphological characteristics.^{2,3} Although significant progress has been made during the last decade, the efficiency of converting solar energy into electrical power with polymer based solar cells is still not high enough, the most efficient devices have the efficiencies of 8.3% by Konarka Technologies, Inc.. To improve the efficiency of plastic solar cells, it is, therefore, crucial to understand the physics of the organic semiconductors and devices; to understand the morphology and the manner in which it develops; and identify what limits the device performance.

1.2 Polymer Semiconductors for Organic Photovoltaic Applications

Conjugated polymers are considered the most popular candidates for the organic photovoltaic applications, why? Except for their mechanical properties and good solubility and, the conjugated polymers share a common electronic structure, which is based on conjugated π electrons. Here, polythiophene is selected as the model of the conjugated polymers.⁴ In the backbone of polythiophene (Fig 1.1 a), each carbon atom

binds to only three adjacent atoms, leaving one electron per carbon atom in a p_z orbital. As a result, the mutual overlap between these p_z forms π bonds along the conjugated backbone, thereby the π electrons along the entire conjugation path were delocalized. These delocalized π electrons in semiconductors can fill a π band, which is called the highest occupied molecular orbital (HOMO) and the empty π^* band is called the lowest unoccupied molecular orbital (LUMO). The energy difference between the HOMO and LUMO, called “band gap” of a conjugated system depends on the conjugation length.⁵ When the conjugation length is reduced, the maximum absorption will be shifted to the “blue” region, and at the same time the local HOMO and LUMO positions of the system will be affected.

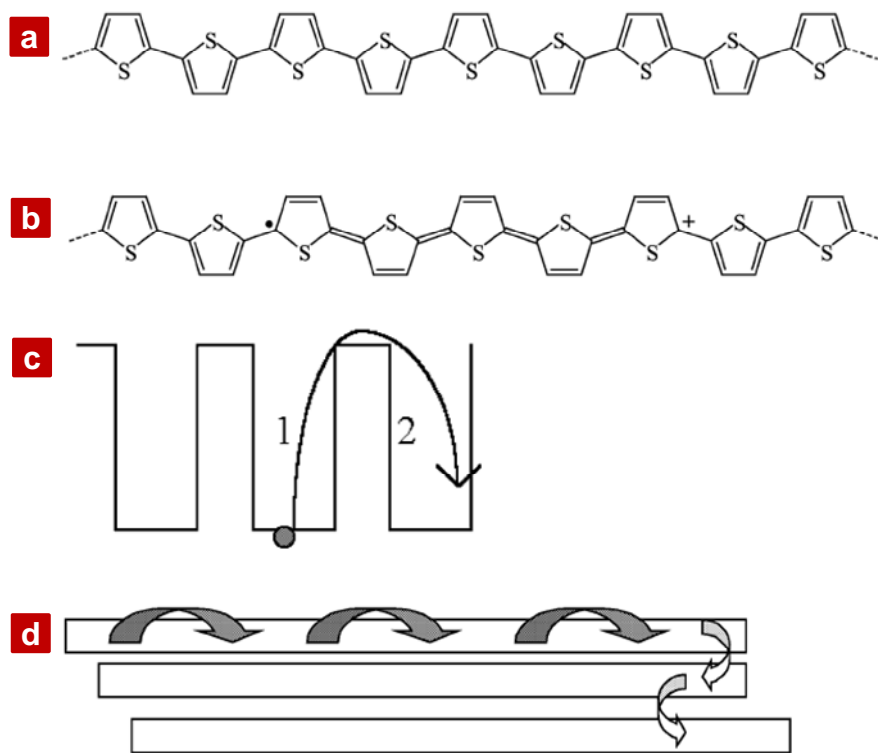


Figure 1.1 Model of conjugated polymers and the photophysics: **a**, polythiophene; **b**, a charged polaron in polythiophene; **c**, hopping process between status 1 and 2; **d**, intra- (filled arrows) and intermolecular (unfilled arrows) charge-transport. Reprint from citation 4.

In conjugated polymers, the electron-phonon coupling leads to the so-called polarons which may be regarded as defects in the conjugated polymer chains (Fig 1.1 b). Such defects could stabilize the charge which is self-trapped as a consequence of lattice deformations. Charge carriers proceed from one such state to another (hopping), thereby absorbing or emitting phonons to overcome the energy difference between these states. So in the majority of organic semiconductors, transport bears all characteristics of a hopping process in which the charge propagates via a side-to-side oxidation–reduction reaction (Fig 1.1 c). In addition to these, intramolecular charge transport along a conjugated polymer chain and intermolecular charge transport between adjacent molecules or polymer chains are necessary to differentiate (Fig 1.1 d). The former which is specific to conjugated polymers is more efficient than the latter.⁶

1.3 Physics of Organic Photovoltaic Solar Cells

A typical organic solar cell is shown in Fig 1.2a, the active layer (P3HT:PCBM) (Fig 1.2b) is sandwiched between two electrodes (cathode and anode), one is transparent and the other one is reflecting, and sun light is introduced through the transparent electrode. In traditional solar cells, indium-tin-oxide (ITO) coated glass or PET is used as the anode, due to its high work function and transparency. A layer of poly(3,4-ethylene dioxythiophene): poly(styrene sulfonate) (PEDOT:PSS) (~ 40 nm) is coated onto the ITO surface to reduce the surface roughness of ITO and further increase the work function of the anode. Then a ~100 nm blend layer of light-harvesting conjugated polymers (e-donor) and electron-accepting materials (e-acceptor) works as an active

layer. A cathode with a low work function (Al, Ca et al.) is deposited onto the active layer by thermal evaporation. Sometimes a thin layer of lithium fluoride (LiF) or other hole blocking layer is deposited between the active layer and Al. When the light shines onto the ITO side, photons are absorbed by the conjugated polymer (*eg.* P3HT) in the active layer, producing excitons (bound electron-hole pairs) that are transported to the interface between the donor and acceptor, where the excitons are dissociated into electrons and holes. Electrons are transported through the acceptor domain and collected by the cathode, and the holes are transported through the donor domain and collected by the anode, which results in an external circuit current. The electrons transporting process in the active layer described schematically in Fig 1.2c.

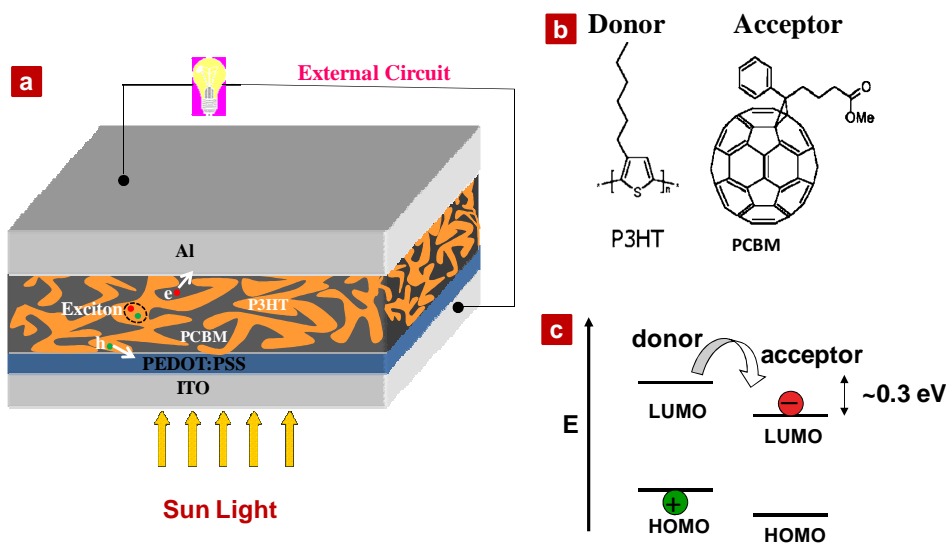


Figure 1.2 **a**, schematic layout of a BHJ solar cell based on P3HT: PCBM; **b**, chemical structure of P3HT (Donor) and PCBM (Acceptor); **c**, the photovoltaic process.

To better understand the physics of the organic photovoltaics, it is the key to know the main conversion steps and loss mechanisms of light power into electric power, which are simply depicted in Fig 1.3. The primary process of photocurrent generation is light absorption, either by the donor or by the acceptor, yielding excitons which have to

diffuse to the interface between the donor and acceptor (Fig 1.3a). When the excitons reach the donor-acceptor interface, electron transfer to the acceptor phase is energetically favored, driven by the energy difference between LUMO levels of the donor and acceptor (> 0.3 eV), which produces an electron-hole pair bound by Coulombic interactions (Fig 1.3b)^{1, 7-9}. The electron-hole pair on this stage is metastable and must be converted into free charge carriers before transport, which mainly depends on temperature and electric field (Fig 1.3c).⁷ The free carriers then must be transported through their respective phases to the electrodes for extraction, which will be affected by the charge carrier mobility of the materials (Fig 1.3d). Possible loss mechanisms are exciton decay (Fig 1.3e), geminate recombination of bound electron-hole pairs, and bimolecular recombination of free charge carriers (Fig 1.3f).

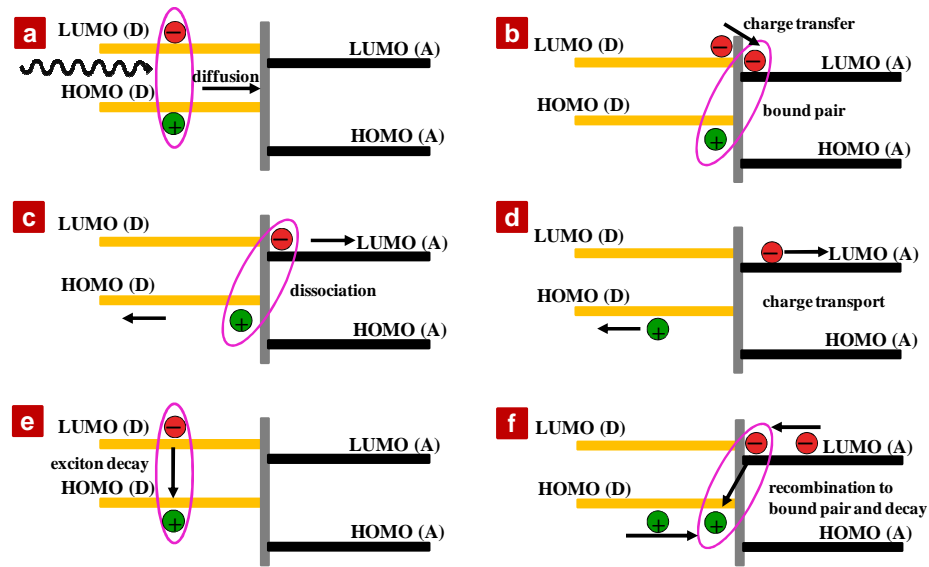


Figure 1. 3 Working mechanism of BHJ organic photovoltaics: **a**, exciton yielding; **b**, coulombically bound electron-hole pair yielding; **c**, dissociation of the electron-hole pair; **d**, free charge carriers transporting; **e**, exciton decay; **f**, recombination of the bound electron-hole pair and bimolecular recombination of free charge carriers. (courtesy of Lambert Jan Anton Koster, University of Groningen)

1.4 Characterization Organic Photovoltaic Solar Cells

The current density-voltage (I-V) characteristics for a solar cell in the dark (blue line) and under illumination (red line), are shown in Fig 1.4. When the cell is in the dark, there is almost no current flowing, until the contacts start to inject electrons at a forward bias larger than a certain value (open-circuit voltage). When the cell is under illumination, the I-V curve is shifted down by the amount of photocurrent (I_{ph}) generated. The open-circuit voltage, V_{oc} , is the maximum photovoltage that can be generated by the cell and corresponds to the voltage when the current under illumination is zero. The maximum current that can run through the cell at zero applied voltage is called the short-circuit current, I_{sc} . In the fourth quadrant, the device generates the maximum power P_{max} ($P_{max} = I_{max} \times V_{max}$). The ratio between P_{max} and the product J_{sc} and V_{oc} is defined as the fill factor (FF) (inserted equation in Fig 1.4), thus $P_{max} = J_{sc} \cdot V_{oc} \cdot FF$. To determine the power conversion efficiency η of a solar cell, the maximum output power P_{max} is compared to the incident light intensity P_{sun} (inserted equation in Fig 1.4). Which physical parameters are going to affect the performance of the plastic solar cell, such as J_{sc} , V_{oc} and FF? Some literatures⁴ indicated that J_{sc} will be affected by the light absorption, quantum efficiency, recombination, electrodes charge collection and *etc*; V_{oc} will be determined by the energy levels of the materials, current leaking, recombination and *etc*; while the FF will be decided by recombination, internal resistance of the cell, electrodes charge collection and *etc*. Optimizing these parameters will be critical to improve the final performance of the OPVs.

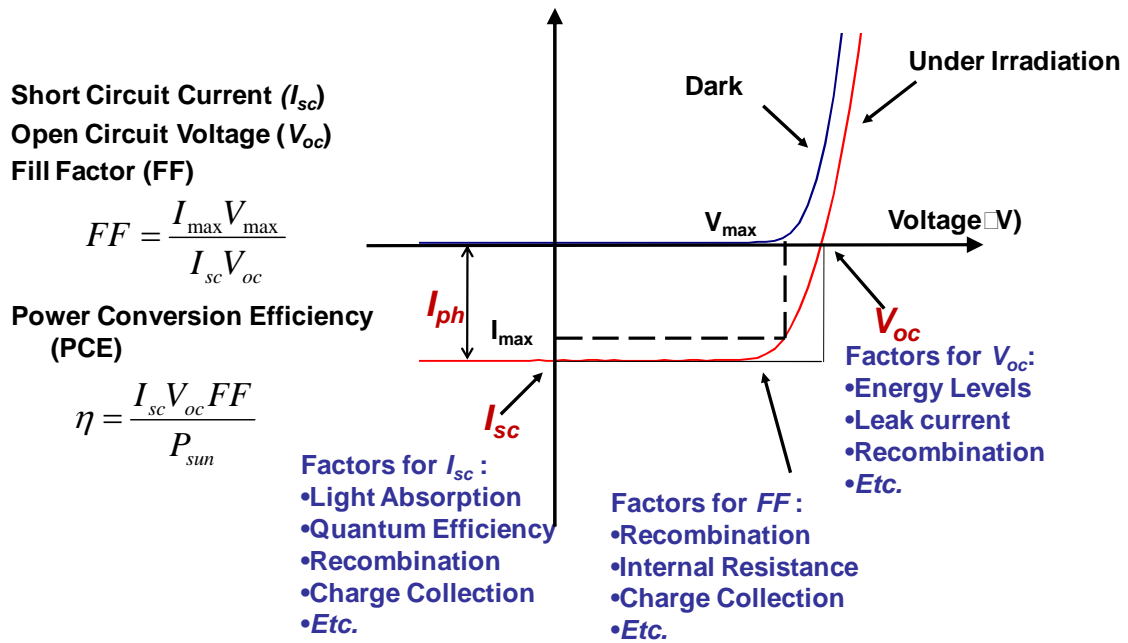


Figure 1. 4 Typical I-V characteristics of an OPV cell in the dark (blue line) and illumination (red line) conditions. The short-circuit current density (I_{sc}) and open-circuit voltage (V_{oc}) are shown. The maximum output power (P_{max}) is given by the rectangle $I_{max} \times V_{max}$, and the power conversion efficiency η is calculated.

1.5 Organic Solar Cell Device Structures

Four different organic photovoltaic devices are depicted in some literatures¹⁰. Fig 1.5 shows the four device structures: (1) single-layer PV cell; (2) bilayer PV cell; (3) disordered bulk heterojunction (the most popular one); (4) ordered bulk heterojunction.

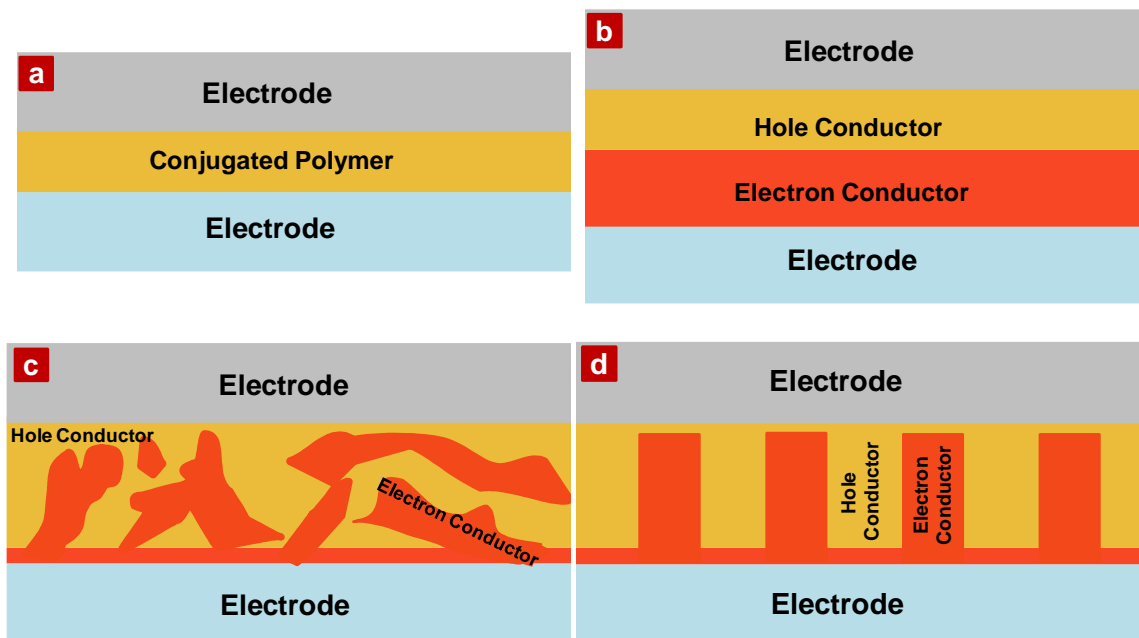


Figure 1.5 Four device architectures of conjugated polymer-based photovoltaic cells: **a**, single-layer OPV cell; **b**, bilayer OPV cell; **c**, disordered bulk heterojunction OPV cell; **d**, ordered bulk heterojunction OPV cell.

(1) Single Layer Devices

The single layer organic solar cell devices are based on a single organic layer sandwiched between two metal electrodes with different work functions, which generate built-in electric fields within the film.¹¹ When the light shines on the cell from the transparent electrode side, photons are absorbed, electrons are excited from the highest occupied molecular orbital (HOMO) to the lowest unoccupied molecular orbital (LUMO) and form excitons, that are then dissociated into free charges (electrons and holes) and collected at the respective electrodes. Since the excitons are strongly bound by Coulombic interactions, the electric field arising from the difference in the work functions of the two electrodes is too weak to dissociate the excitons into the free charges. As a result, a reasonable V_{oc} can be produced by a single-layer conjugated

polymer solar cell, but the photocurrent is very low¹². This can be explained by the following: (1) the predominant tendency of the conjugated polymers to form bound excitons that decay rather than dissociate at room temperature¹³ and (2) the low mobility of the free carriers which were created in conjugated polymers.

(2) Bilayer Devices

The first bilayer solar cell was developed by Tang.¹⁴ And the first polymer/C₆₀ based bilayer solar cell were fabricated by Saricifici et al.¹⁵ Two materials with different HOMO and LUMO were layered to dissociate the excitons into free charge carriers.^{14, 15} In this so-called heterojunction, excitons dissociation is benefited where the electron will be accepted and transported in electron acceptor materials (A) and the hole in the electron donor materials (D), the separated charge carriers are more difficult to recombine with its counterpart. By carefully matching these materials, electrons transfer from the donor to the acceptor, or holes transfer from the acceptor to the donor, is energetically favored. The major difference between single layer device and a bilayer heterojunction device is that in the latter the electrons and holes are confined to e-acceptor phase and e-donor phase respectively. The recombination of free electrons and holes now mainly occurs at the interface of the phases and the free charges are transported within one phase, where the electrons travel within the n-type acceptor phase and the holes travel within the p-type donor phase. Hence, holes and electrons are effectively separated from each other and, thus, charge recombination is greatly reduced and depends more on trap densities. Since the exciton diffusion length is ~ 10 nm¹⁶⁻¹⁸,

only the excitons created in a thin layer at the heterojunction can contribute to the photocurrent of the cell, most excitons generated in the remainder of the device are lost.

(3) Bulk Heterojunction Devices

It is critical to overcome the exciton recombination, which results from a failure to reach the donor/acceptor interface. Since exciton dissociation is most effective at the interface between e-donor phase and e-acceptor phase, the excitons should be formed within domains that are comparable to the exciton diffusion length, typically $\sim 10 \text{ nm}^{21}$. In 1995 Yu, Halls *et al.*^{19, 20} built a cell by mixing donors and acceptors, which increases the D/A interfacial area dramatically and decreases the distance excitons have to travel to reach the interface. This gave rise to the concept of “Bulk Heterojunction (BHJ)”, where the junctions between the electron- and hole-conducting materials occur within the bulk of the materials.

Mixtures of light-harvesting conjugated polymers (donor) and electron-accepting fullerene derivatives (acceptor) offer a promising route toward the development of light-weight, cost-effective, large-area, flexible OPV solar cells.^{1, 19} Within these “bulk heterojunction” (BHJ) OPVs, the donor and acceptor phases should be bicontinuous, with a characteristic length scale comparable to the exciton diffusion length of $\sim 10 \text{ nm}^{21}$. The small size scale of the morphology minimizes the recombination of the bound electron-hole pair and generates a large interfacial area to effectively dissociate the excitons.^{19, 22, 23} The dissociated carriers (electrons and holes) are transported to the cathode and anode, respectively, resulting in an external photocurrent. Clearly, the performance of such BHJ devices depends critically on the morphology of the

photoactive layer²⁴. The only difference between BHJ and the bilayer device is the larger D/A interfacial area, where charge separation occurs, photo-generated excitons can be dissociated into free charges at any place. Like in bilayer devices, the charges are also separated within the different phases and, hence, recombination is reduced to a large extent.

Chapter 2, 3 of this thesis will focus on detailed descriptions of the BHJ morphologies and the manner it develops in the P3HT/PCBM system.

(4) Ordered Bulk Heterojunction Devices

The “ordered bulk heterojunction”, consisting of vertically aligned conjugated polymer nanorods, surrounded by the e-acceptor materials to form the ordered bicontinuous heterojunction morphology, and at the same time maximize the interfacial area and shorten the free charges transporting distance, has been proposed as the ideal morphology for the active layer.^{10, 25} Several research groups have used nanoimprint lithography to produce the polymer nanostructures by using Si mold²⁶. While making the Si mold with nanometer pore size is of high cost. The anodic aluminum oxide (AAO) membranes were also selected to fabricate the conjugated polymer nanopillars²⁵⁻²⁸, but the template removal process will dissolve the PEDOT:PSS layer, leave impurities on the active layer, and in addition to these, the base or acidic solution used to remove the template will deleteriously affect the device performance.

Chapter 4 of this thesis will focus on a cost-effective and simple method to fabricate the P3HT nanostructures by using silicone modified AAO membranes as the

templates, as well as testing the performance of the “ordered bulk heterojunction” devices.

1.6 Morphology

It is well established that the polymer active layer morphology in such BHJs plays a crucial role in the final device properties. In order to fabricate high performance BHJ photovoltaic devices, it is critical to control the nanoscale morphology, molecular ordering, and interfacial properties of all components comprising the device. This also translates into controlling the materials properties, like charge carrier mobility and optical absorption.^{6, 24} While all the above morphologies are strongly affected by the preparation conditions, including the vapor pressure of the solvent²⁹⁻³¹, the rate of solvent removal^{32, 33}, the volume fractions of the components^{30, 34, 35}, the use of chemical additives³⁶⁻⁴², thermal annealing treatments⁴³⁻⁴⁵ and solvent annealing⁴⁶⁻⁴⁸. There has been a tremendous amount of research performed on the P3HT/PCBM blends system using a broad range of techniques to determine the morphology^{5, 15, 17, 19-25}, yet the results from these studies are less than definitive and, in some cases, contradictory.

For example, the defocused transmission electron microscopy (TEM) is the most common way to measure the morphology of the blend system. But recently Mackay et al.⁴⁹ argued that the defocused TEM micrographs for a 1:1 blend of P3HT and PCBM and that of a pure polystyrene film were very similar, as shown in Fig 1.6. Consequently, arguments of spinodal phase separation of P3HT/PCBM using TEM can and should be questioned, since contrast can also arise from film thickness fluctuation. In order to provide new insights and guidance in the generation of active layers in

organic photovoltaics that are crucial in enhancing the device performance, developing methods to quantitatively characterize the morphology of P3HT: PCBM, the interfacial behavior between the active layer and electrodes, are essential.

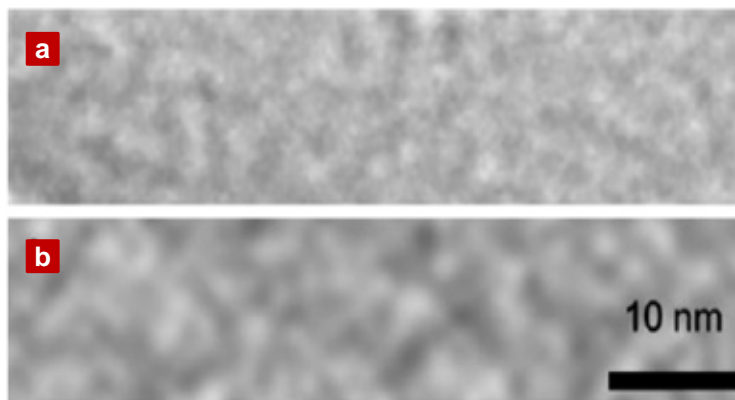


Figure 1.6 Defocused TEM cross-sectional images of polymer samples prepared by ultramicrotomy shows little difference for a variety of materials: **a**, a 1:1 by weight P3HT: PCBM blend; **b**, pure polystyrene. Reprint from citation 49.

Chapter 2 of this thesis will focus on detailed descriptions of the morphologies and interfacial behavior in thin film blends of regio-regular poly(3-hexylthiophene) (P3HT) and [6,6]-phenyl C₆₁-butyric acid methyl ester (PCBM), by multiple techniques.

To better understand the physics of the photoactive layer in the OPV devices, it is also necessary to gain a quantitative understanding of the morphology and the manner in which it develops. Despite a decade of intensive research, a detailed understanding of the mechanism of the phase separation in the photo-active layer is still elusive. Some of the researchers claimed the active layer phase separation was driven by the spinodal decomposition^{50, 51}; some of them thought that it was induced by surface-directed spinodal decomposition⁵²; and others argued that the bicontinuous morphology of the

active layer was affected by the crystallization of the components of the active layer^{24, 53,}
⁵⁴. A key element in the kinetics associated with the morphology development is the interdiffusion of the components.

Chapter 4 of this thesis will focus on understanding the phase separation mechanism of the active layer, by using P3HT/PCBM bilayer as a model to investigate the interdiffusion of the components and its role in the development of the morphology. A detailed description of the diffusion behavior and the morphology developed from a layer of P3HT in contact with a layer of PCBM during thermal annealing is given.

1.7 Reference

- (1) Brabec, C. J.; Sariciftci, N. S.; Hummelen, J. C. *Adv. Funct. Mater.* **2001**, 11, 15-26.
- (2) Liang, Y. Y.; Xu, Z.; Xia, J. B.; Tsai, S. T.; Wu, Y.; Li, G.; Ray, C.; Yu, L. P. *Adv. Mater.* **2010**, 22, E135-E138.
- (3) Chen, H. Y.; Hou, J. H.; Zhang, S. Q.; Liang, Y. Y.; Yang, G. W.; Yang, Y.; Yu, L. P.; Wu, Y.; Li, G. *Nature Photon.* **2009**, 3, 649-653.
- (4) Nunzi, J. M. *Comptes Rendus Physique* **2002**, 3, 523-542.
- (5) Hoffmann, R.; Janiak, C.; Kollmar, C. *Macromolecules* **1991**, 24, 3725-3746.
- (6) Sirringhaus, H.; Brown, P. J.; Friend, R. H.; Nielsen, M. M.; Bechgaard, K.; Langeveld-Voss, B. M. W.; Spiering, A. J. H.; Janssen, R. A. J.; Meijer, E. W.; Herwig, P.; de Leeuw, D. M. *Nature* **1999**, 401, 685-688.
- (7) Mihailetchi, V. D.; Koster, L. J. A.; Hummelen, J. C.; Blom, P. W. M. *Phys. Rev. Lett.* **2004**, 93, 216601.
- (8) Brabec, C. J.; Zerza, G.; Cerullo, G.; De Silvestri, S.; Luzzati, S.; Hummelen, J. C.; Sariciftci, S. *Chem. Phys. Lett.* **2001**, 340, 232-236.
- (9) Sariciftci, N. S.; Smilowitz, L.; Heeger, A. J.; Wudl, F. *Science* **1992**, 258, 1474-1476.
- (10) Coakley, K. M.; McGehee, M. D. *Chem. Mater.* **2004**, 16, 4533-4542.
- (11) Sze, S. M.; Ng, K. K., *Physics of semiconductor device*. John. Wiley & Sons: New York, **1981**.
- (12) Marks, R. N.; Halls, J. J. M.; Bradley, D. D. C.; Friend, R. H.; Holmes, A. B. J. *Phys.: Condens. Matter.* **1994**, 6, 1379-1394.
- (13) Gregg, B. A. *J. Phys. Chem. B* **2003**, 107, 4688-4698.
- (14) Tang, C. W. *Appl. Phys. Lett.* **1986**, 48, 183-185.
- (15) Sariciftci, N. S.; Braun, D.; Zhang, C.; Srdanov, V. I.; Heeger, A. J.; Stucky, G.; Wudl, F. *Appl. Phys. Lett.* **1993**, 62, 585-587.
- (16) Halls, J. J. M.; Pichler, K.; Friend, R. H.; Moratti, S. C.; Holmes, A. B. *Appl. Phys. Lett.* **1996**, 68, 3120-3122.

- (17) Markov, D. E.; Tanase, C.; Blom, P. W. M.; Wildeman, J. *Phys. Rev. B* **2005**, 72, 045217.
- (18) Markov, D. E.; Amsterdam, E.; Blom, P. W. M.; Sieval, A. B.; Hummelen, J. C. *J. Phys. Chem. A* **2005**, 109, 5266-5274.
- (19) Yu, G.; Gao, J.; Hummelen, J. C.; Wudl, F.; Heeger, A. J. *Science* **1995**, 270, 1789-1791.
- (20) Halls, J. J. M.; Walsh, C. A.; Greenham, N. C.; Marseglia, E. A.; Friend, R. H.; Moratti, S. C.; Holmes, A. B. *Nature* **1995**, 376, 498-500.
- (21) Spanggaard, H.; Krebs, F. C. *Sol. Energy Mater. Sol. Cells.* **2004**, 83, 125-146.
- (22) Thompson, B. C.; Frechet, J. M. J. *Angew. Chem. Int. Ed.* **2008**, 47, 58-77.
- (23) Dennler, G.; Sariciftci, N. S. *Proceedings of the Ieee* **2005**, 93, 1429-1439.
- (24) Campoy-Quiles, M.; Ferenczi, T.; Agostinelli, T.; Etchegoin, P. G.; Kim, Y.; Anthopoulos, T. D.; Stavrinou, P. N.; Bradley, D. D. C.; Nelson, J. *Nature Mater.* **2008**, 7, 158-164.
- (25) Aryal, M.; Trivedi, K.; Hu, W. C. *ACS Nano* **2009**, 3, 3085-3090.
- (26) Aryal, M.; Buyukserin, F.; Mielczarek, K.; Zhao, X. M.; Gao, J. M.; Zakhidov, A.; Hu, W. C. *J. Vac. Sci. Technol., B.* **2008**, 26, 2562-2566.
- (27) Haberkorn, N.; Gutmann, J. S.; Theato, P. *ACS Nano* **2009**, 3, 1415-1422.
- (28) Wang, H. S.; Lin, L. H.; Chen, S. Y.; Wang, Y. L.; Wei, K. H. *Nanotechnology* **2009**, 20, 075201.
- (29) Shaheen, S. E.; Brabec, C. J.; Sariciftci, N. S.; Padinger, F.; Fromherz, T.; Hummelen, J. C. *Appl. Phys. Lett.* **2001**, 78, 841-843.
- (30) Park, S. H.; Roy, A.; Beaupre, S.; Cho, S.; Coates, N.; Moon, J. S.; Moses, D.; Leclerc, M.; Lee, K.; Heeger, A. J. *Nature Photon.* **2009**, 3, 297-303.
- (31) Kim, Y.; Choulis, S. A.; Nelson, J.; Bradley, D. D. C.; Cook, S.; Durrant, J. R. *Appl. Phys. Lett.* **2005**, 86, 063502.
- (32) Li, G.; Shrotriya, V.; Huang, J. S.; Yao, Y.; Moriarty, T.; Emery, K.; Yang, Y. *Nature Mater.* **2005**, 4, 864-868.

- (33) Mihaiilechi, V. D.; Xie, H. X.; de Boer, B.; Popescu, L. M.; Hummelen, J. C.; Blom, P. W. M.; Koster, L. J. A. *Appl. Phys. Lett.* **2006**, 89, 012107.
- (34) Mayer, A. C.; Toney, M. F.; Scully, S. R.; Rivnay, J.; Brabec, C. J.; Scharber, M.; Koppe, M.; Heeney, M.; McCulloch, I.; McGehee, M. D. *Adv. Funct. Mater.* **2009**, 19, 1173-1179.
- (35) van Bavel, S. S.; Barenklau, M.; de With, G.; Hoppe, H.; Loos, J. *Adv. Funct. Mater.* **2010**, 20, 1458-1463.
- (36) Pivrikas, A.; Stadler, P.; Neugebauer, H.; Sariciftci, N. S. *Org. Electron.* **2008**, 9, 775-782.
- (37) Peet, J.; Kim, J. Y.; Coates, N. E.; Ma, W. L.; Moses, D.; Heeger, A. J.; Bazan, G. C. *Nature Mater.* **2007**, 6, 497-500.
- (38) Chen, H. Y.; Yang, H. C.; Yang, G. W.; Sista, S.; Zadoyan, R. B.; Li, G.; Yang, Y. *J. Phys. Chem. C.* **2009**, 113, 7946-7953.
- (39) Moule, A. J.; Meerholz, K. *Adv. Mater.* **2008**, 20, 240-245.
- (40) Lee, J. K.; Ma, W. L.; Brabec, C. J.; Yuen, J.; Moon, J. S.; Kim, J. Y.; Lee, K.; Bazan, G. C.; Heeger, A. J. *J. AM. CHEM. SOC.* **2008**, 130, 3619-3623.
- (41) Yao, Y.; Hou, J. H.; Xu, Z.; Li, G.; Yang, Y. *Adv. Funct. Mater.* **2008**, 18, 1783-1789.
- (42) Wang, W. L.; Wu, H. B.; Yang, C. Y.; Luo, C.; Zhang, Y.; Chen, J. W.; Cao, Y. *Appl. Phys. Lett.* **2007**, 90, 183512.
- (43) Ma, W. L.; Yang, C. Y.; Gong, X.; Lee, K.; Heeger, A. J. *Adv. Funct. Mater.* **2005**, 15, 1617-1622.
- (44) Hoppe, H.; Sariciftci, N. S. *J. Mater. Chem.* **2006**, 16, 45-61.
- (45) Yang, X. N.; Loos, J.; Veenstra, S. C.; Verhees, W. J. H.; Wienk, M. M.; Kroon, J. M.; Michels, M. A. J.; Janssen, R. A. J. *Nano Lett.* **2005**, 5, 579-583.
- (46) Zhao, Y.; Xie, Z. Y.; Qu, Y.; Geng, Y. H.; Wang, L. X. *Appl. Phys. Lett.* **2007**, 90, 043504.
- (47) Jo, J.; Na, S. I.; Kim, S. S.; Lee, T. W.; Chung, Y.; Kang, S. J.; Vak, D.; Kim, D. Y. *Adv. Funct. Mater.* **2009**, 19, 2398-2406.
- (48) van Bavel, S. S.; Sourty, E.; de With, G.; Loos, J. *Nano Lett.* **2009**, 9, 507-513.

- (49) Kiel, J. W.; Kirby, B. J.; Majkrzak, C. F.; Maranville, B. B.; Mackay, M. E. *Soft Matter* **2010**, 6, 641-646.
- (50) Audinot, J. N.; Leveque, P.; Bechara, R.; Leclerc, N.; Guillot, J.; Migeon, H. N.; Hadziioannou, G.; Heiser, T. *Surf. Interface Anal.* **2010**, 42, 1010-1013.
- (51) Watts, B.; Belcher, W. J.; Thomsen, L.; Ade, H.; Dastoor, P. C. *Macromolecules* **2009**, 42, 8392-8397.
- (52) Vaynzof, Y.; Kabra, D.; Zhao, L. H.; Chua, L. L.; Steiner, U.; Friend, R. H. *ACS Nano* **2011**, 5, 329-336.
- (53) Chen, D.; Liu, F.; Wang, C.; Nakahara, A.; Russell, T. P. *Nano Lett.* **2011**, 11, 2071-2078.
- (54) Chen, D. A.; Nakahara, A.; Wei, D. G.; Nordlund, D.; Russell, T. P. *Nano Lett.* **2011**, 11, 561.

CHAPTER 2

P3HT/PCBM BULK HETEROJUNCTION ORGANIC PHOTOVOLTAICS: CORRELATING EFFICIENCY AND MORPHOLOGY

2.1 Introduction

Mixtures of light-harvesting conjugated polymers (donor) and electron-accepting fullerene derivatives (acceptor) offer a promising route toward the development of light-weight, cost-effective, large-area, flexible organic photovoltaic, OPV, solar cells.^{1, 2} Within these “bulk heterojunction” (BHJ) OPVs, the donor and acceptor phases should be bicontinuous with a characteristic length scale comparable to the exciton diffusion length of ~10 nm. The small size scale of the morphology minimizes the excitation decay and generates a large interfacial area to effectively dissociate photon excitons.^{1, 3, 4} The dissociated carriers (electrons and holes), are transported to the cathode and anode, respectively, resulting in an external photocurrent. Clearly, the performance of such BHJ devices depends critically on the morphology of the photoactive layer⁵ and it remains a challenge to maximize photon absorption, charge separation and charge transport while maintaining the necessary size scale and continuity constraints of the morphology of these blends. Added to this are the segregation of components at the interfaces between the active layer and cathode/anode to facilitate electron/hole collection and minimize charge carrier recombination. In addition, the thickness of the active layer, usually ~100-200 nm, confined between the two electrodes interfaces place constraints on the morphology developed.

The morphology of OPVs, within the BHJ layer and at the cathode and anode interfaces, are strongly affected by the preparation conditions, including the vapor pressure of the solvent⁶⁻⁸, the rate of solvent removal^{9, 10}, the volume fractions of the components^{7, 11, 12}, the use of chemical additives¹³⁻¹⁹, thermal annealing treatments²⁰⁻²² and solvent annealing²³⁻²⁵. There has been a tremendous amount of research performed on the P3HT/PCBM blends system using a broad range of techniques to determine the morphology^{5, 15, 17, 19-25}, yet the results from these studies are less than definitive and, in some cases, contradictory.

Here we have used multiple techniques to develop a complete, quantitative description of the bulk morphology and interfacial behavior in P3HT/PCBM thin films (~80 nm), confined and unconfined between two electrodes, where variations in the preparation conditions have been minimized to develop a coherent description of the active layer and a quantitative understanding of the relationship between the morphology and device performance. Small angle neutron scattering (SANS) and high resolution transmission electron microscopy (HRTEM) demonstrate the existence of bicontinuous morphology with a characteristic length scale of ~10 nm that was formed within seconds of annealing at 150 °C and remained relatively unchanged with continued annealing. Dynamic secondary ion mass spectroscopy (DSIMS) shows that the presence of the cathode strongly influences the interfacial segregation of the PCBM, and that PCBM penetrates into the PEDOT: PSS layer during annealing. Grazing incidence x-ray diffraction (GIXD) shows the formation of oriented crystalline domains of the P3HT with grain sizes commensurate with that found by electron microscopy. Near edge x-ray absorption fine structure (NEXAFS) reveals a re-orientation of the

morphology immediately at the Al/active layer interface during thermal annealing. By combining these findings, a relationship between the device efficiency and the morphology of the active layer was developed.

2.2 Experimental

2.2.1 Materials and Methods

Regioregular poly(3-hexylthiophene) ($M_w = 42.4$ k, $M_n = 21.2$ k, RR = 96.8%) and [6,6]-phenyl-C61-butyric acid methyl ester were obtained from Konarka Technologies. The Deuterated PCBM, ([6,6]-Pentadeuterophenyl C61 butyric acid methyl ester), was purchased from Sigma-Aldrich. The indium tin oxide (ITO)-coated glass substrates (20 ± 5 ohms/sq) were bought from Thin Film Devices Inc..

2.2.2 Organic Solar Cell Devices Making and Testing

ITO coated glass substrates were cleaned through ultrasonic treatment in detergent, DI water, acetone, and isopropyl alcohol and then dried in an oven overnight. PEDOT: PSS (CLEVIOSTM P VP Al 4083) (~35 nm) was spin-coated onto ultraviolet ozone-treated ITO substrates. After annealing at 150 °C for 30 min in air, the substrates were transferred to a glove box. The P3HT (10 mg): PCBM (10 mg)/1 mL chlorobenzene solution was spin-coated on top of the PEDOT: PSS layer at 1000 rpm. The thickness of P3HT/PCBM film was ~ 80 nm (KLA-TENCOR Alpha-Step IQ Surface Profiler). Finally, ~100-nm-thick Al cathode was deposited (area 6 mm²) on the P3HT/PCBM layer under high vacuum (2×10^{-4} Pa) using a thermal evaporator. For thermal annealing, the completed devices were placed directly onto a digitally

controlled hot plate and heated to 150 °C for the desired time. All current-voltage (I-V) characteristics of the devices were measured under simulated AM1.5G irradiation (100 mW cm⁻²) using a Xe lamp-based Newport 91160 300-W Solar Simulator. A Xe lamp equipped with an AM1.5G filter was used as the white light source. The light intensity was adjusted with an NREL-calibrated Si solar cell with a KG-5 filter. Quantum efficiency measurements were made using a 300-W Xe lamp, Acton 2150i monochromatic, optical chopper, and lock-in amplifier. The monochromatic beam was focused into an area smaller than the device area and the photon flux was determined using a Newport calibrated silicon photodiode.

2.2.3 Focus Ion Beam (FIB) and TEM

TEM cross sections were prepared using an FIB/SEM system (Zeiss Auriga Cross Beam FIB) where a Ga⁺² ion column is equipped onto a high resolution field emission SEM. To protect the surface layer from ion beam damage, a Pt layer of about 150 nm was first deposited on the top surface of the device/chip through electron beam induced in-situ deposition. Then a second Pt layer of about 1.5 μm was deposited on top of the e-beam induced Pt layer via ion beam induced deposition. After Pt deposition, a lamella of a size around 20 μm (width) x 12 μm (depth) x 1 μm (thickness) was normally cut out from the bulk device/chip (perpendicular to the chip surface) and lifted up and welded to a TEM grid. Once the thick cross-section was mounted on a TEM grid, a thinning and polishing process by Ga⁺² ion beam of various energies and beam currents were applied from both sides of the lamella. The final thickness of the specimen was ~ 30-40 nm. To minimize ion beam induced damage to the specimen, 2

keV ion beam was employed for final polishing/cleanup. The prepared TEM specimen was then transferred into a spherical aberration (C_s) corrected transmission electron microscope equipped with corrected Omega energy filter (Zeiss Libra 200 CsTEM) for imaging and analysis. The TEM imaging was done at beam energy of 200 keV. To differentiate the phase between PCBM and the surrounding polymer matrix (e.g. P3HT), zero-loss filtered imaging with an energy window about 5 eV was applied throughout the investigation.

2.2.4 Electron Energy Loss Spectroscopy (EELS)

EELS was used for elemental analysis. In the case of the diffusion layer of aluminum, a spot of 1 nm in size was focused at the middle of the diffusion layer and the spectrum was acquired with an exposure time of 20 seconds. To ensure minimal sample drift, the EELS analysis was performed one hour after the specimen was inserted into the microscope sample chamber.

2.2.5 Small-angle Neutron Scattering (SANS)

SANS experiments were performed at the High Flux Isotope Reactor neutron scattering facility at Oak Ridge National Laboratories (ORNL) (CG-2 SANS). 10 multi-layers, each with a ~80 nm thick layer of the P3HT/PCBM blends, were stacked together, where the neutron beam was delivered at normal incidence to the film surface, placing the scattering vector in the plane of the film.

2.2.6 Grazing Incidence X-ray Ddiffraction (GIXD)

GIXD measurements were performed on Beamline 7.3.3 at the Advanced Light Source at the Lawrence Berkeley National Laboratory. The experimental set-up and sample cell were designed for the surface studies on thin films. An X-ray beam impinged onto the sample at a grazing angle above and below the critical angle of the polymer film ($\alpha_c = 0.16$) but below the critical angle of the silicon substrate ($\alpha_c = 0.22$). The wavelength of X-rays used was 1.240 Å, and the scattered intensity was detected by using two-dimensional charge-coupled device (CCD) camera with image sizes of 2304 x 2304 pixels.

2.2.7 Near Edge X-ray Absorption Fine Structure (NEXAFS)

NEXAFS measurements were performed on the wiggler beam line 10-1 at Stanford Synchrotron Radiation Laboratory, using ~80% linearly polarized light and an energy resolution of ~60 meV at the carbon K-edge. A cylindrical mirror analyzer was used to monitor the Carbon KLL Auger electrons and a picoampmeter was used to detect the sample current. A highly transmissive gold grid (~85%) was used to normalize to the incoming flux. The resulting Auger Electron Yield (AEY) and Total Electron Yield (TEY) was furthermore normalized by subtracting a linear pre-edge background and scaling such that the edge jump far above the K-edge was constant, i.e. normalized to the number of C atoms. Monochromator drifts were calibrated by the structure in the monitored incoming photon flux around 284.7 eV.^{26, 27}

2.2.8 Dynamic Secondary Ion Mass Spectrometry (DSIMS)

DSIMS measurement was done by using the SIMS system: 6650 Quadrupole SIMS (Physical Electronics USA, Chanhassen, MN). Beam energy was 2 kV using Ar⁺ ions as the primary ions, and the beam diameter was 20 microns, raster was 350 microns, accepting negatively-charged secondary ions from the center 20 percent of the crater area. Samples were thin enough that no charge compensation was needed. Base pressure was always below 1×10^{-9} torr.

2.2.9 Differential Scanning Calorimetry (DSC)

DSC measurements were performed using a TA Instrument Q200 instrument under Ar purge (25mL/min). P3HT was sealed in DSC pans with different amount of PCBM. Samples were initially heated at a rate of 40°C/min from room temperature to 270 °C, then held there for 10 min. Subsequently, the samples were cooled at a rate of 2 °C/min to 50 °C and held at 50 °C there for 10 min. The samples were heated at a rate of 10 °C/min to 270 °C, and the melting point (T_m) was obtained from the on the high temperature side intersection of the base line with the tangent to the endotherm. T_m^0 is the melting point of the pure P3HT obtained using the same procedure.²⁸

2.3 Results and Discussion

2.3.1 UV-Vis Absorption and Device Performance at Different Preparation Conditions

The ultraviolet-visible (UV-Vis) absorption spectra and external quantum efficiencies (EQE) of devices using mixtures of P3HT: PCBM (10 mg: 10 mg)/mL chlorobenzene are shown in Fig. 2.1 for four different preparations. The first (black line) is where the active layer was simply spin coated onto the PEDOT: PSS layer with no further thermal treatment henceforth, referred to as the “As Spun” preparation. The second (red line) is where the active layer on the PEDOT:PSS was annealed under a nitrogen atmosphere at 150 °C for 30 minutes before a 100 nm thick Al (cathode) layer was evaporated on top of the active layer and, is referred to as the “Pre-Annealed” treatment. The third is where the Al was evaporated onto the active layer and, subsequently, the entire device was annealed at 150 °C for 5 seconds (blue line) and 30 minutes (green line), referred to as “Post-Annealed”. The difference between these preparations is that, with the “Post-Annealed”, the active layer is confined between the cathode and the PEDOT: PSS layer and an interfacial energy, as opposed to a surface energy for the “Pre-Annealed” case, dictates the segregation of components to the cathode interface. The anode interface is the same in both cases. In comparison to the “As spun” case, the “Pre-Annealed” and “Post annealed” cause the absorption spectra of the active layer to red-shift, increasing the overlap with the solar spectrum. The shoulder centered at 605 nm, seen for all thermally annealed active layers, even after a 5 second annealing, arises from the crystallization of the P3HT^{5, 29} which further enhances the absorption in the visible range. The EQE spectra reflect the changes observed in the absorption spectra with a significant increase being seen with thermal annealing. As seen, the “Post Annealed” shows a dramatic enhancement in the EQE, even with only a

5 second annealing. The energy conversion efficiency and the short-circuit current density behavior parallels the EQE behavior (Table 2.1).

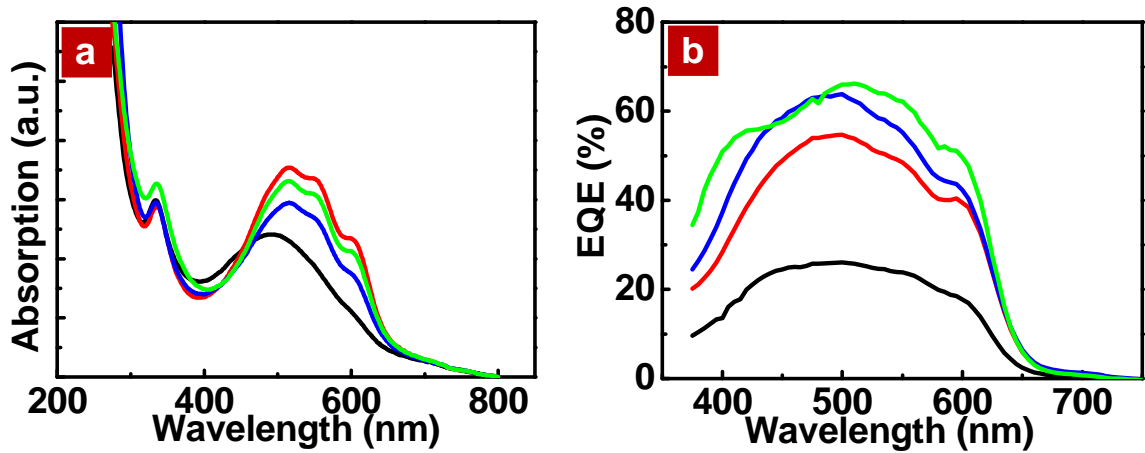


Figure 2.1 Ultraviolet-visible absorption and EQE. **a**, Absorption spectra of P3HT/PCBM blend films: “As Spun”, (black line); “Pre-Annealed” 30 min, (red line); “Post-Annealed” 5 sec (blue line); “Post-Annealed” 30 min’ (green line). **b**, EQE spectra of P3HT/PCBM bulk heterojunction solar cells: “As Spun”, (black line); “Pre-Annealed”, (red line); “Post-Annealed” 5 sec (blue line); “Post-Annealed” 30 min (green line).

Table 2.1 Performance of the P3HT/PCBM BHJ photovoltaic devices.

	Voc (V)	Jsc (mA/cm²)	Fill factor (%)	Efficiency (%)
As Spun	0.50	3.53	34.56	0.61
Pre-Annealed 150 °C, 30 min	0.372	7.25	40.78	1.10
Post-annealed 150 °C, 5 s	0.556	7.57	50.75	2.14
Post-Annealed 150 °C, 30 s	0.556	8.34	56.49	2.62
Post-Annealed 150 °C, 1 min	0.548	8.12	61.58	2.74
Post-Annealed 150 °C, 5 min	0.543	8.80	60.50	2.89
Post-Annealed 150 °C, 30 min	0.573	9.11	64.51	3.37
Post-Annealed 150 °C, 60 min	0.567	9.02	64.53	3.30

2.3.2 Bulk Morphology of the Active Layer Thin Film and the Interfacial Behavior between the Active Layer and the Electrodes

Shown in Fig 2.2 are high resolution transmission electron microscopy (HRTEM) images of ~35 nm cross-sections of the P3HT/PCBM active layer. Fig 2.2a shows the “As Spun” case where adhesive failure between the active layer and the PEDOT: PSS layer occurred during the preparation of the thin section. Secondly, PCBM and P3HT are uniformly mixed with no evidence of phase separation even at high magnification (inset). It should be noted that spin coating the active layer is not the same as blade coating where, in the latter, the slower removal of the solvent from the blend film can result in a phase separation of the PCBM and P3HT. In all our experiments,

spin coating was used. Finally, during the evaporation of the Al onto the active layer, there is a penetration of Al into the active layer where a ~4 nm diffusion or boundary layer is evident immediately adjacent to the crystalline Al layer (as evidenced by the lattice planes and electron energy loss spectroscopy (EELS) (Fig 2.3 a). Upon annealing the multilayered sample to 150 °C for 30 minutes, notable changes are observed in the TEM image (Fig 2.2b). First, no delamination was observed and the interface between the PEDOT: PSS and the active layer appears diffuse, suggesting an interdiffusion between these two layers. Secondly, the extent of penetration of the Al into the active layer remained unchanged, indicating that in the device there are isolated Al atoms or clusters of Al atoms near the cathode interface that can influence the device performance. In addition, as indicated by the arrow, the PCBM-rich phase (darker domain) is in contact with the cathode interface (a highly magnified image is shown in Fig. 2.3b). Most notably, the active layer is no longer uniform and a phase separation of the P3HT and PCBM into bicontinuous morphology is evident. Identical bulk morphology was obtained for the “Pre-Annealed” sample. Based on the electron densities, the darker areas are PCBM-rich, while the lighter areas are P3HT-rich. The average size of the domains in the active layer is ~10-15 nm which is commensurate with the exciton diffusion length and the bicontinuous nature of the morphology is necessary for the device to function. While it is tempting to argue that the morphology arises from a spinodal phase separation of the two components, the length scales observed are not commensurate with numerous past studies on the phase separation of polymer mixtures.^{30, 31} The observed morphology can also arise from a competition between crystallization of the P3HT, where the crystals grow at a rate G_{P3HT} , and a

diffusion of the PCBM away from the growth front, characterized by the diffusion coefficient of the PCBM in the P3HT of D_{PCBM} . D_{PCBM}/G defines δ , a length scale of the size of the crystals. δ will not be isotropic but dependent on G of the different crystal planes of the P3HT.^{32, 28, 33}

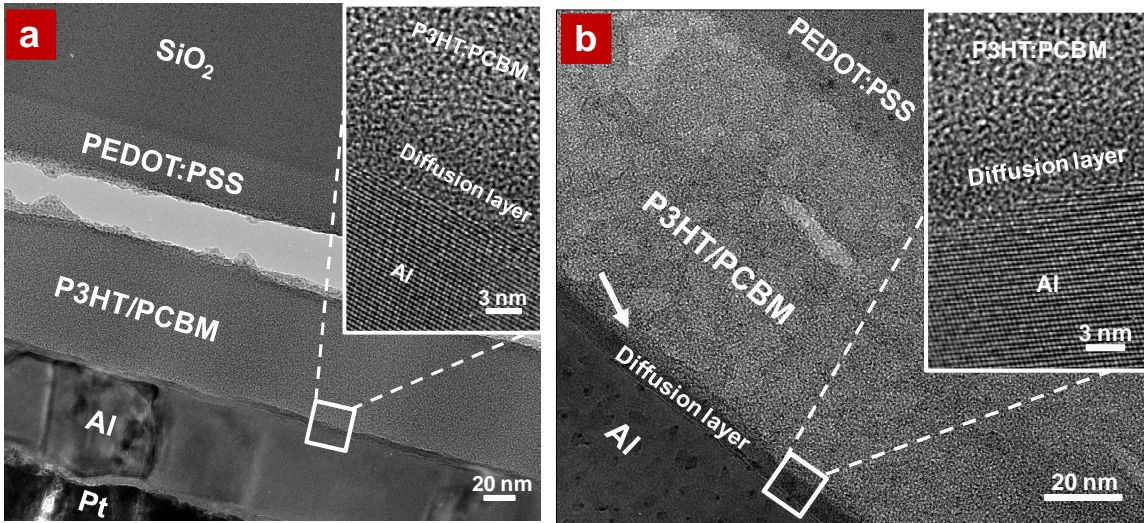


Figure 2.2 HRTEM of cross-sections of P3HT/PCBM based multilayered samples. **a**, “As Spun”; **b**, “Post-Annealed” 30 min heating at 150 °C. The insets represent high magnification.

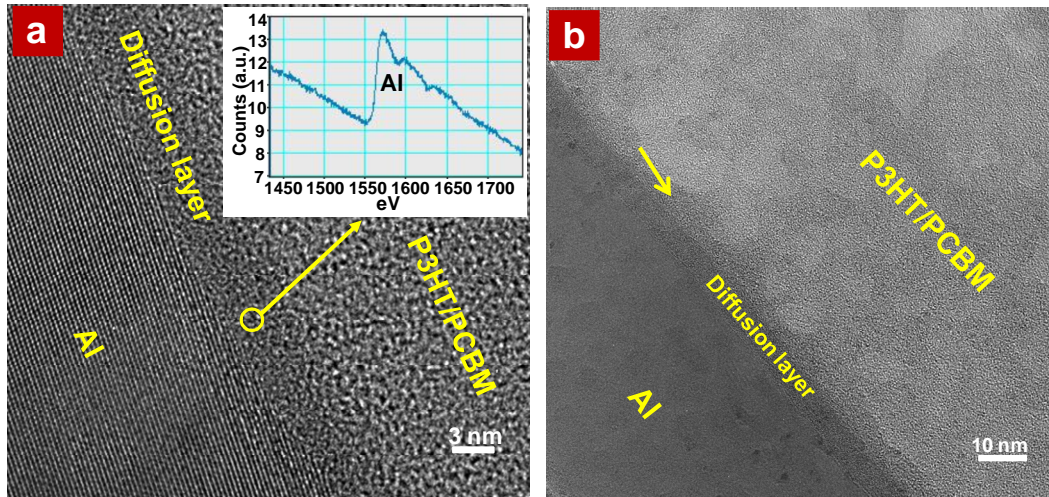


Figure 2.3 HRTEM of cross-sections of P3HT/PCBM based multilayered samples. **a**, “As Spun”, inset shows the EELS of the diffusion layer; **b**, “Post-Annealed” heating at 150 °C.

Small angle neutron scattering (SANS) offers a second means to characterize the bulk morphology of the active layer. Since the lengths of deuterium and carbon are comparable, the scattering length density of PCBM is significantly different from P3HT, affording a large neutron contrast.^{34, 35} SANS experiments were performed on a stack of 10 multi-layers (Si/PEDOT:PSS/P3HT+PCBM/Al), each with a ~ 80 nm thick active layer of the P3HT/PCBM blends, where the neutron beam impinged on the stack at normal incidence, placing the scattering vector in the plane of the film. The silicon substrate and Al layer are transparent to neutrons while the PEDOT: PSS produces only a constant incoherent scattering background that can easily be subtracted. The SANS from the “As Spun” film is shown in Fig 2.4 where only a very low, weakly angularly dependent scattering is seen. Using Guinier’s Law, which states that $I(q) = I(0)\exp(-R_g^2 q^2/3)$ where $I(q)$ is the observed scattering at $q=(4/\lambda)\sin(\varepsilon/2)$, where λ is the neutron wavelength and $\varepsilon=2\theta$ is the scattering angle, and R_g is the radius of gyration of the scattering particle, a value of $R_g < 1$ nm is obtained which arises from uniformly dispersed PCBM, which, as would be expected, leads to a low efficiency. However, after only 5 seconds of heating at 150 °C, the “Post-Annealed” sample showed a significant increase in the SANS with a marked angular dependence. Heating this sample for an additional 25 seconds caused the SANS to increase further and then, with continued heating, the SANS increased only slightly, which indicate that the bulk morphology of the active layer was developed within a few seconds of annealing. Experiments on the “Pre-Annealed” case was done only for a sample heated to 150 °C for 30 minutes and showed SANS identical to that of the “Post-Annealed-30 min” sample, indicating that the bulk morphology of the active layer is not influenced by the

presence of the Al cathode and the differences in the efficiencies of the two has another origin. For a two-phase system the SANS can be treated using the Debye-Bueche equation, $(I(q))^{-1/2} = K(a^3 Q)^{-1}(1 + a^2 q^2)$ where K is a constant, a is the correlation length and $Q = \phi_1 \phi_2 (b_1 - b_2)^2$ is the scattering invariant where ϕ_i is the volume fraction of phase i with a neutron scattering length density of b_i . The time dependence of “ a ” and “ Q ” are shown in the inset of Fig 2.4 for the “Post Annealed” samples. As can be seen, “ a ” increases from ~0.5 nm initially, to ~4.6 nm after 5 seconds of heating to ~5.3 nm after 30 minutes of annealing at 150 °C or longer. From “ a ”, the chord length, i.e. the average size of each domain, can be calculated if the volume fractions of the phases are known. If we assume the volume fractions of the phases are equal to the volume fractions of the components (admittedly a coarse estimate), then, after 30 minutes of annealing, the average chords lengths for the P3HT-rich and PCBM-rich phases are ~11 nm (Table 2.2) which are fully consistent with the HRTEM results. In addition, if the time dependence of Q is examined, a slight increase in Q is observed with time, indicating that $(b_1 - b_2)$ is increasing or that the purity of the phases increases with further annealing. This result is significant, since it means that PCBM, trapped within the P3HT domains, is gradually removed with time. The trapped PCBM can act as traps that will reduce the device efficiency and their removal from the P3HT domain will enhance device efficiency.

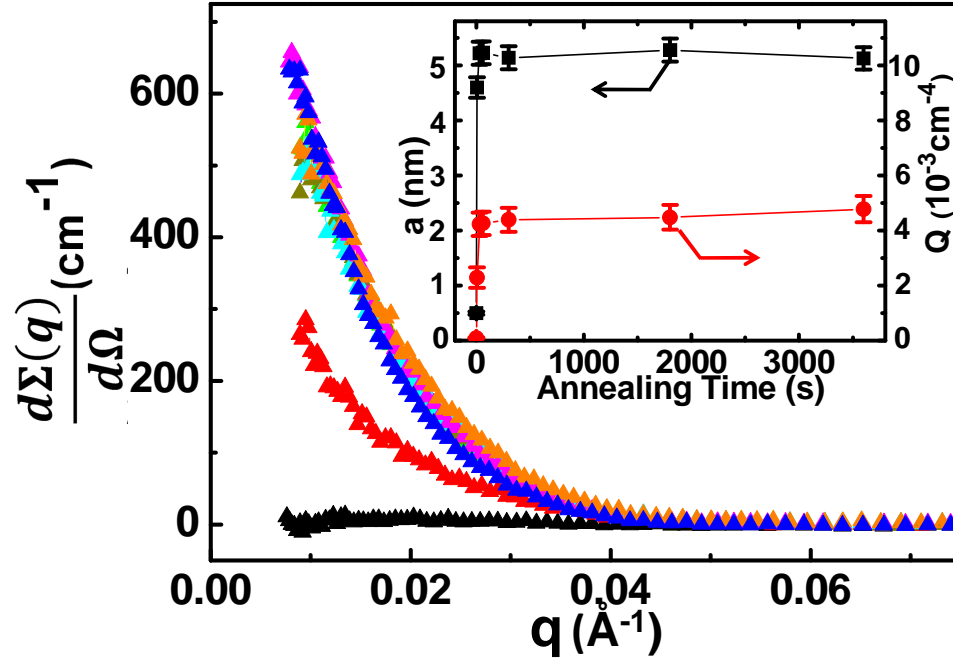


Figure 2.4 SANS profiles of P3HT/PCBM blend films: “As Spun”, (▲); “Pre-Annealed” 30 min (▲); “Post-Annealed” 5 sec (▲); “Post-Annealed” 30 sec (▲); “Post-Annealed” 1 min (▲); “Post-Annealed” 5 min (▲); “Post-Annealed” 30 min (▲); “Post-Annealed” 1 hr (▲). The inset represents the correlation length (a) and the scattering invariant (Q) versus the “Post-Annealing” time.

Table 2.2 Values of the scattering invariant (Q), the correlation length (a) and the average chords length for the P3HT-rich and PCBM-rich phases obtained under different thermal annealing conditions.

	As-Spun	Pre-Anneal 30 min	Post-Anneal 5 s	Post-Anneal 30 s	Post-Anneal 1 min	Post-Anneal 5 min	Post-Anneal 30 min	Post-Anneal 1 h
Q (10^{-3}cm^{-4})	0.1	4.32	2.29	4.23	4.26	4.39	4.48	4.78
a (nm)	0.5	5.32	4.60	5.22	5.23	5.14	5.28	5.13
*L _{P3HT} (nm)	/	12.58	10.87	12.34	12.36	12.15	12.48	12.13
*L _{PCBM} (nm)	/	9.22	7.97	9.05	9.06	8.91	9.15	8.89

Volume Fraction: $\Phi_{\text{P3HT}} = 0.577$; $\Phi_{\text{PCBM}} = 0.423$

*To obtain the chord length, we assumed that the volume fractions of the phases were equal to the volume fractions of the components. This is only an estimate but should only introduce minimal error.

2.3.3 Crystal Orientation and Size of P3HT in the Photoactive Layer

Grazing incidence x-ray diffraction (GIXD), shown in Fig. 2.5, was used to examine the ordering of the P3HT in the thin films. Experiments were performed at incidence angles of 0.12° , below the critical angle, to probe the near surface ordering of the P3HT, and at 0.18° , above the critical angle, to obtain information on the bulk ordering. The diffraction vector is oriented normal to the film surface so that ordering in that direction is studied. Experiments on the “Pre-Annealed” samples were performed without the Al cathode layer, while for the “Post- Annealed” samples, an aqueous CuCl_2 solution was used to remove the Al cathode. X-ray photoelectron spectroscopy (XPS) confirmed the absence of Cu or Al left on the surface (Fig. 2.6). The GIXD from the “As Spun” sample, at 0.12° and 0.18° , showed the (100) reflection, along with a weak

second order reflection, centered at $q = 3.79 \text{ nm}^{-1}$ ($d=1.66 \text{ nm}$) and 3.71 nm^{-1} ($d=1.69 \text{ nm}$), while there was no observable (010) reflection. The (100) reflection is characteristic of the edge-on structure shown schematically in the figure. The absence of the (010) reflection, characteristic of the π - π interchain stacking, for the “As Spun” sample is to be expected, since the P3HT chains will be less ordered, which is consistent with the UV-Vis absorption (Fig.2.1). The “Pre-Annealed” sample showed a significant sharpening and intensification of the (100) reflection, along with the appearance of the (010). The (010) reflection is characteristic of the face-on structure shown schematically in the figure. Consequently, the ordering of the P3HT has markedly improved with thermal annealing, both at the surface and in the interior of the film, and there is evidence of both edge-on and face-on orientations of the P3HT crystals at the surface (cathode interface). These results are consistent with the GIXD results published by others.³⁶⁻³⁹ From the Scherrer’s equation^{38, 40} the dimensions of crystals along the (100) and (010) planes, determined from the full width at half-maximum of the reflections, are $\sim 23 \text{ nm}$ and $\sim 12 \text{ nm}$, respectively, which are consistent with the TEM and SANS results and suggest that one of the phases observed in those experiments can be assigned to the P3HT crystals.(Table 2.3) The GIXD of the “Post-Annealed” sample shows a similar enhancement in the ordering with comparable crystal sizes. However, from the ratio of the integrated intensities of the (010) to (100), it is apparent that there are more crystals with a face-on orientation for the “Post-Annealed” sample, compared with the “Pre-Annealed” sample. With thin-film transistors (TFTs), this orientation gives higher hole mobility^{36, 41} and probably is of consequence for better photovoltaic device

performance. This enhancement in the face-on orientation is clearly a result of the presence of the Al cathode during thermal annealing.

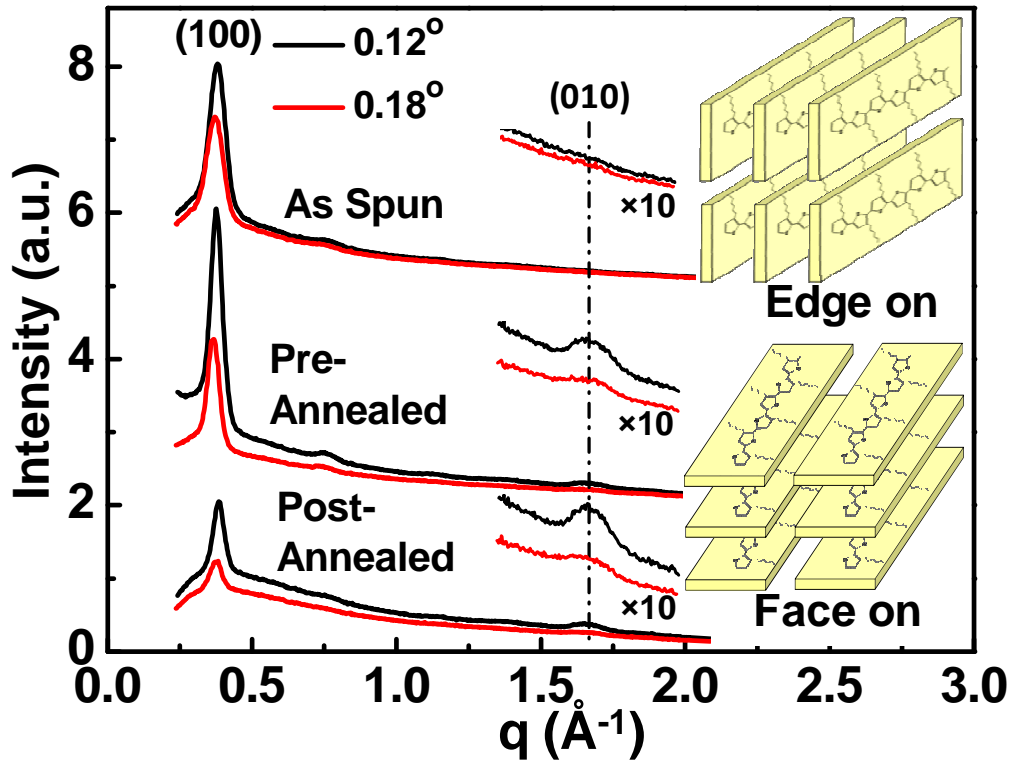


Figure 2.5 GIXD curves of P3HT/PCBM blend films at different incident angles. “As Spun”; “Pre-Annealed” 30 min; “Post-Annealed” 30 min. The insets represent the schemes of edge-on and face-on of P3HT chains.

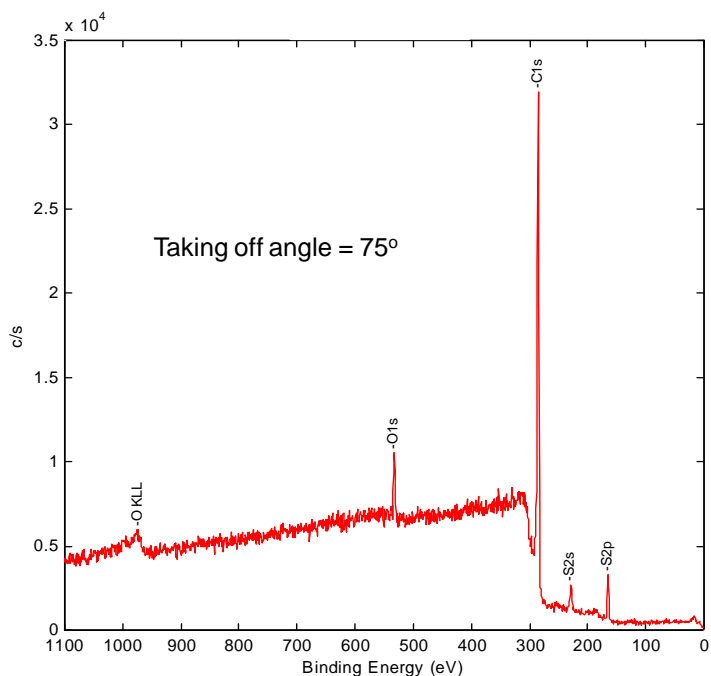


Figure 2.6 XPS of “Post-Annealed” 30 min heating at 150 °C after removing Al with an aqueous CuCl₂ solution.

Table 2.3 P3HT crystal size obtained under different thermal annealing conditions.

	Incident angle	d(100) (nm)	d(010) (nm)	FWHM (Å ⁻¹) (100)	Crystal size (nm) (100)	FWHM (Å ⁻¹) (010)	Crystal size (nm) (010)
As-spun	0.12°	1.66	/	0.0557	20.30	/	/
	0.18°	1.69	/	0.0578	19.56	/	/
Pre-annealed -30 min	0.12°	1.67	0.38	0.0475	23.80	0.0941	12.02
	0.18°	1.72	0.38	0.0484	23.36	0.089	12.70
Post-annealed -30min	0.12°	1.64	0.38	0.0493	22.93	0.0905	12.49
	0.18°	1.67	0.38	0.0485	23.31	0.108	10.48

2.3.4 P3HT Crystal Orientation and PCBM Segregation at the Interface

Near-edge X-ray absorption fine structure (NEXAFS) was used to determine the average near-surface orientation of P3HT chains in the P3HT/PCBM films and the surface composition. Fig. 2.7 shows the Carbon K-edge NEXAFS spectra, measured in Auger (AEY) and total (TEY) electron yields, from the P3HT/PCBM active layer for “Pre-Annealed” and “Post-Annealed”. As with the GIXD measurements, the Al cathode was removed with an aqueous CuCl_2 solution. The NEXAFS intensity is dominated by resonances arising from transitions from the 1s core level to unfilled molecular orbitals of π^* and σ^* character, which are specific to the bonding within different functional groups. In Fig. 2.7, the peaks at 285.0 and 286.46 eV are C=C π^* resonances from PCBM, and the peak at 285.85 eV is the C=C π^* resonance from P3HT. The broad features at higher energies are transitions to σ^* orbitals. The spectra of the pristine PCBM and P3HT were used to fit the spectra of the P3HT/PCBM active layer thin-film mixtures weighted by the volume fraction of the components.^{42, 43} (Figure 2.8). Synchrotron radiation is strongly polarized in the horizontal plane, as shown schematically in Fig. 2.7, so that by rotating the sample, electric field vector of the x-ray beam can be changed from being nearly normal to the film surface ($\vec{E} \perp$ substrate, shallow incidence angle) to being nearly parallel to the film surface ($\vec{E} \parallel$ substrate, high incidence angles). The angular dependence of the highly symmetric π^* and σ^* orbitals can be used to determine the orientations of the functional groups,^{26, 44} distinguishing between the edge-on and face-on orientation of the P3HT chain packing.

Moreover, the difference in probing depths between AEY (1 nm) and TEY (10 nm) spectra provides the orientation of chains within the first nanometer and 10 nm

from the surface.²⁷ In the pristine samples (Fig 2.8a), the intensity of the P3HT 1s- π^* is strongly depending on the incident angles, indicating that pure P3HT film surface has more edge-on, as opposed to face-on, orientation of the P3HT chain packing. PCBM show no dependence on the incidence angle, due to the spherically symmetric fullerene cage.⁴²

NEXAFS spectra from the “Pre-Annealed” sample are shown in Fig. 2.7a and 2.7c. Both the AEY and TEY show that the π^* intensity from PCBM is much weaker than that from P3HT, indicating that the PCBM composition, relative to P3HT, is lower at the film surface. This result is consistent with the neutron reflectivity results of Mackay et al.³⁵ and Parnell et al.³⁴. The spectra also show that the amount of “edge on” P3HT packing is much higher than the “face on” structure in the first nanometer and 10 nm from the surface. Consequently, annealing the active layer without the Al cathode present, resulted in a re-orientation of the P3HT at the surface and a reduction in the PCBM concentration at the surface. This can be understood in terms of the surface energies PCBM (38.2 mN/m)⁴⁵ and P3HT (26.9 mN/m)⁴⁶.

NEXAFS spectra from the “Post-Annealed” sample (Fig. 2.7b and 2.7d) showed an increase in the π^* intensity from PCBM that increases with annealing time, indicating that PCBM segregates to the interface between the Al cathode and the active layer, even after only a 5 second annealing (Fig. 2.8b-g, Table. 2.4). In addition, the ratio of “face on” to “edge on” chain packing at the surface increases dramatically in comparison to the “As Spun” and “Pre-Annealed” samples, which is consistent with the GIXD data. This ratio continues to increase with the post-annealing time. It should also be noted that this ratio for AEY is greater than that for TEY which indicate that the

“face on” structure is richer at the surface than in the bulk film. The differences in the orientation of the P3HT and the increase in PCBM concentration at the cathode interface underpin the superior performance of devices prepared in this manner.

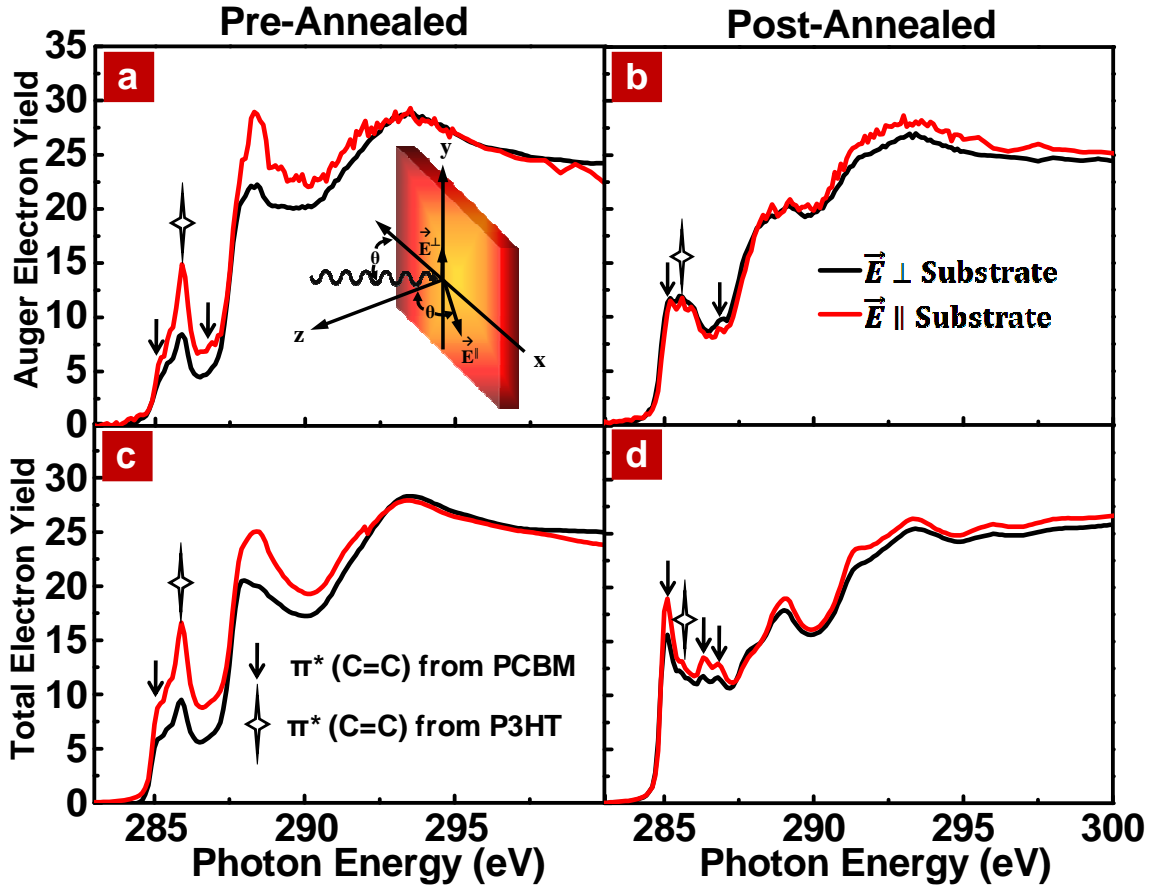
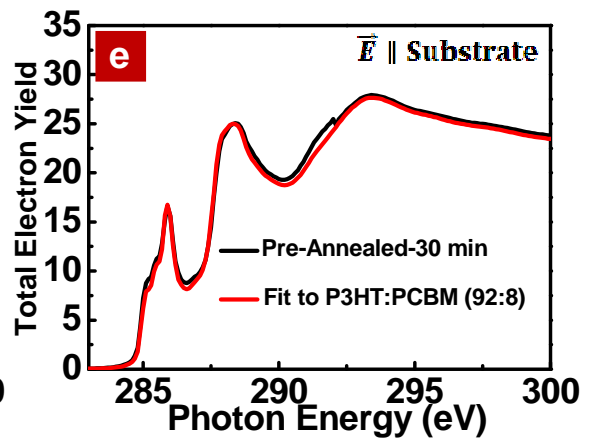
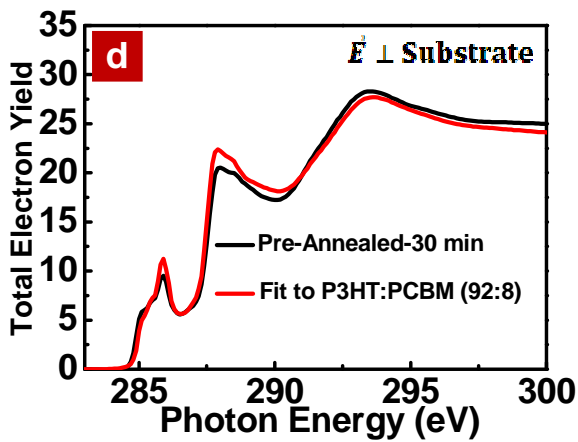
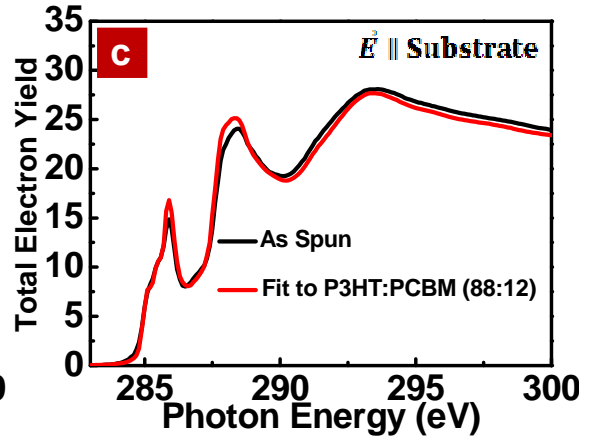
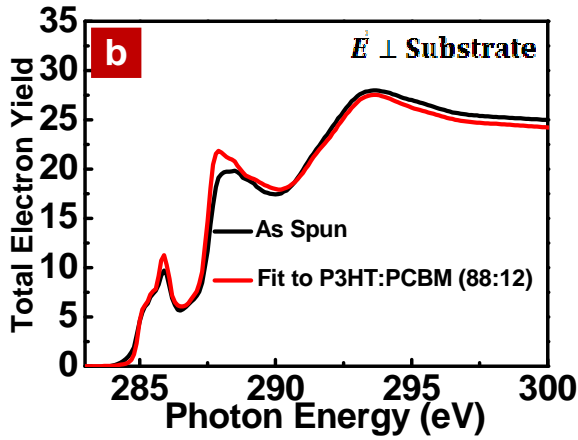
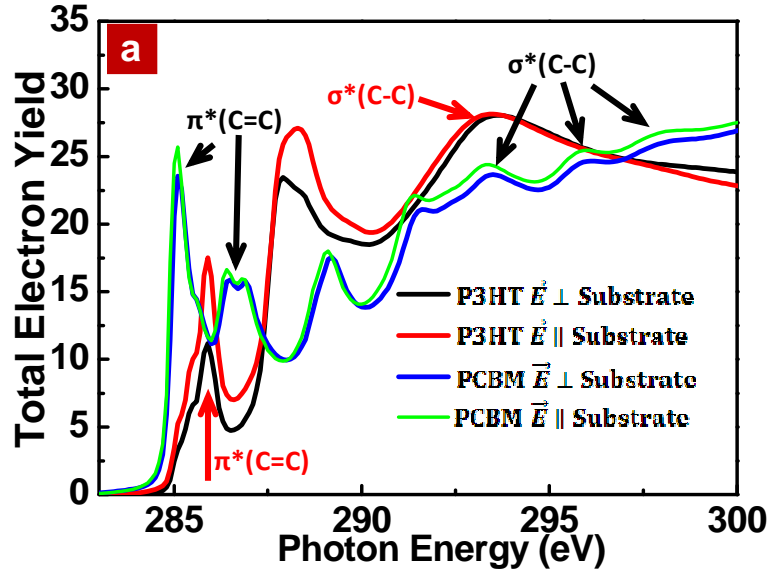


Figure 2.7 NEXAFS spectra of P3HT/PCBM blend films. **a**, AEY of “Pre-Annealed” 30 min sample; **b**, AEY of “Post-Annealed” 30 min sample; **c**, TEY of “Pre-Annealed” 30 min sample; **d**, TEY of “Post-Annealed” 30 min sample. The inset represents the experimental geometry: the X-rays are incident in the x-z plane with the incident angle, θ , which is measured from the sample surface. The electric field vector of the circularly polarized X-rays has two components, \vec{E}_{\parallel} (major) and \vec{E}_{\perp} . The polar angle θ of the dominant component \vec{E}_{\parallel} from the surface normal is the same as the X-ray incidence angle. Here, we use \vec{E} instead of \vec{E}_{\parallel} for the dominant electric field vector.



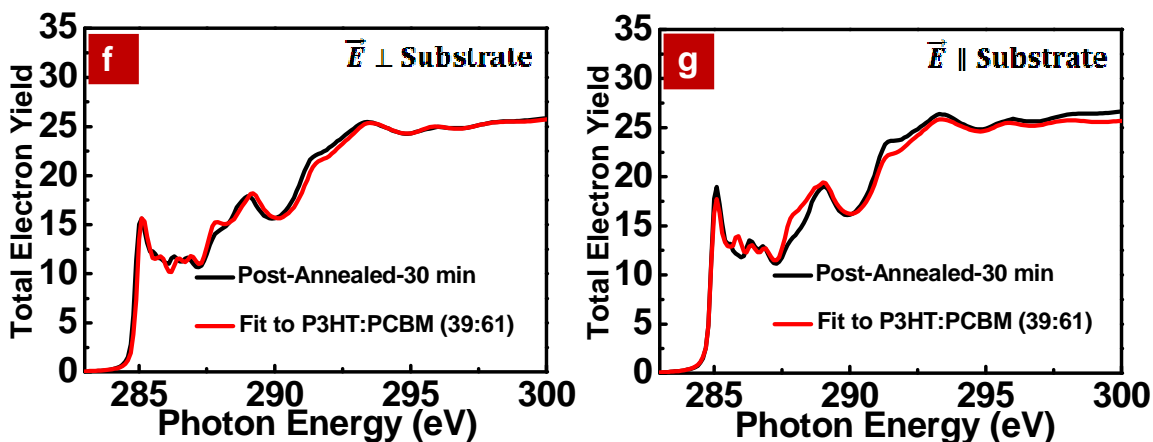


Figure 2.8 NEXAFS spectra of P3HT/PCBM blend films and the linear fitting with the spectra of the pure PCBM and P3HT. **a**, TEY spectra of pure P3HT and PCBM at different incident angles; **b-c**, TEY spectra of the “As Spun” sample and the fitting curves at different incident angles; **d-e**, TEY spectra of the “Pre-Annealed” 30 min at 150°C sample and the fitting curves at different incident angles; **f-g**, TEY spectra of the “Post-Annealed” 30 min at 150 °C sample and the fitting curves at different incident angles.

Table 2.4. The near surface composition of PCBM

	As Spun	Pre-Annealed-30 min	Post-Annealed-5sec	Post-Annealed-1 min	Post-Annealed-30 min
PCBM (Vol %)	12	8	41	44	61

The variation in the composition of the active layer as a function of depth was measured using dynamic secondary ion mass spectroscopy (DSIMS) using an Ar⁺ ion beam which has a depth resolution of ~5 nm. Deuterated PCBM was used to provide a distinct marker for the location of the PCBM, while the S signal was used to locate the P3HT and PEDOT: PSS. As with the GIXD and NEXAFS measurements, the Al cathode was removed with an aqueous CuCl₂ solution. In all cases, a sacrificial layer of

polystyrene was floated onto the surface of the active layer to allow a constant etching rate to be achieved before encountering the active layer. The difference in the etching rate of PCBM and P3HT (the ion beam etches P3HT twice as PCBM) and the phase separation of the P3HT and PCBM will give rise to a deterioration of the depth resolution, but the information obtained is in real space and provides a direct measure of the relative concentration of components.

Shown in Figure 2.9 are the S and D signals from the different preparations of the active layer. For the “As Spun” film, a depletion of the D signal, corresponding to the PCBM is seen at both the air surface and at the interface between the active layer and the PEDOT: PSS. For the “Pre-Annealed” sample, the S signal from the P3HT is seen to increase at the air surface while the D signal arising from the PCBM decreases, which is consistent with the NEXAFS and HRTEM results. In addition, a broadening of the interface between the PEDOT: PSS and active layer is observed for both the S and D signal, suggesting an interdiffusion between the active layer and the PEDOT: PSS layer. This is consistent with the increase in adhesion noted in the FIB and TEM experiments. For the “Post Annealed” sample, there is a decrease in the concentration of the P3HT at the cathode interface and a corresponding increase in the concentration of the PCBM. At the PEDOT: PSS interface, there is a broadening of the D signal arising from the PCBM and a slight broadening of the S signals arising from the P3HT and PEDOT: PSS, both indicating a diffusion of PCBM into the PEDOT: PSS layer. Shown also in Figure 2.9c are the results for the “Post-Annealed” sample after only 5 seconds of annealing at 150 °C. Here, the concentration of P3HT is seen to decrease at the PEDOT: PSS interface while the movement of the PCBM to the cathode interface causes a depletion of the

P3HT near this interface. With time, these signals are seen to achieve the results in Fig 2.9d. Nonetheless, the surprising result here is the rapidity at which the components can diffuse in the layer which raises the question of the miscibility of the components.

Shown in Figure 2.9e are a series of inter-diffusion experiments where a 100 nm thick layer of P3HT was floated onto the surface of a 60 nm thick layer of PCBM. The solid lines are the D signal from the PCBM and the open circles are the S signals from the P3HT. Initially, the interface between the two layers is sharp. However, after only 5 seconds of annealing at 150 °C, the PCBM is seen to penetrate completely through the P3HT layer with a signal that is constant as a function of depth. The interface between this mixed layer and the P3HT has moved closer to the substrate without a significant broadening of the interface. A diffusion coefficient of PCBM into the P3HT can be estimated to be at least 10^{-11} cm²/sec (calculated simply by using the film thickness and annealing time of 5 seconds) and is, more than likely, much higher. Kramer and coworkers⁴⁷ recently investigated the interdiffusion of the PCBM and P3HT in detail with observations similar to that seen here. The shape of the concentration profiles of the P3HT and PCBM is reminiscent of a Case II diffusion of P3HT into PCBM where there is a sharp diffusion front preceded by a small Fickian precursor. However, annealing the bilayer for 5 minutes at 150 °C dispels this viewpoint. After 5 minutes the profile of P3HT at the interface has moved further into the PCBM and has clearly broadened. However, the concentration of PCBM in the P3HT has only increased slightly and there is no variation with depth. It should also be noted that the integrated signal arising from the PCBM has decreased significantly. However, the morphology of the P3HT more than likely holds the key to this behavior and the unusual diffusion

behavior. P3HT is semi-crystalline with crystalline domains of tens nanometers in size as evidenced by HRTEM and GIXD. P3HT crystallizes very rapidly and the grain boundaries between the crystals establish a pathway or framework in which the PCBM must diffuse. Since PCBM is quite soluble in the amorphous P3HT, it is rapidly drawn into these amorphous regions effectively swelling the P3HT, causing the thickness of the P3HT layer to increase. Some P3HT span these grain boundaries forming a network that limits the diffusion of the PCBM into the P3HT and the extent to which the P3HT can be swollen. It should be noted that the local concentration of PCBM in these amorphous regions will be much higher than that observed in the DSIMS measurements. The constant concentration of PCBM in the P3HT layer also argues that the P3HT crystallizes much more rapidly than that the PCBM can diffuse. While the origin of the reduction in the integrated signal arising from PCBM with time is not known, microscopic crystals of PCBM were observed that were avoided during the DSIMS experiments. Such crystals can give rise to an effective reduction in the total amount of PCBM in DSIMS.

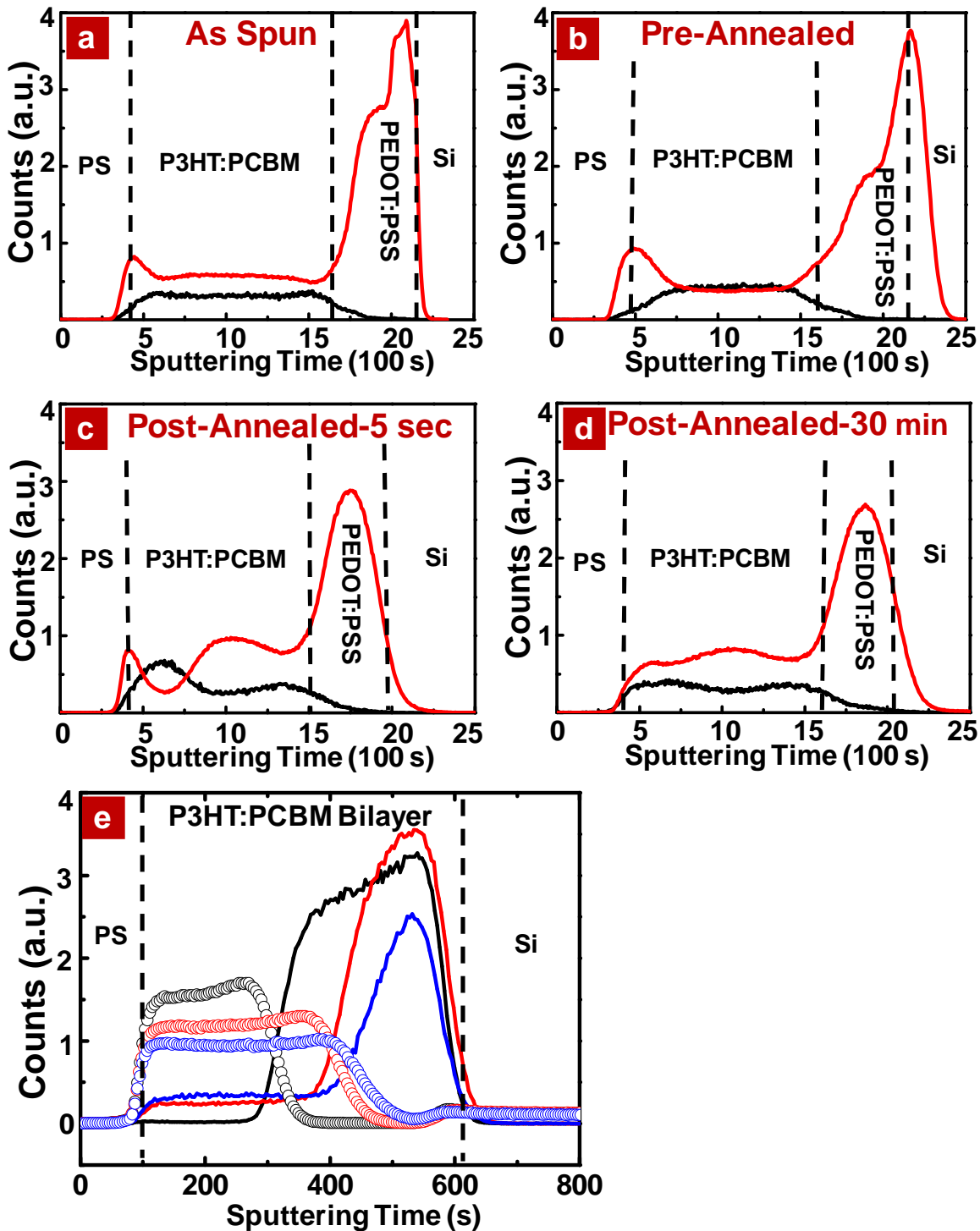


Figure 2.9 DSIMS of the P3HT/deuterated PCBM blend films. **a**, “As Spun”; **b**, “Pre-Annealed” 30 min; **c**, “Post-Annealed” 5 sec; **d**, “Post-Annealed” 30 min; ‘S signal’ (red line); ‘D signal’ (black line). **e**, P3HT/PCBM bilayer diffusion at 150 °C at different time: 0 sec (black), 5 sec (red), 5 min (blue), ‘S signal’ (open circle); ‘D signal’ (solid line).

Dynamic secondary ion mass spectroscopy (DSIMS) was used to obtain the concentration of the different components in the P3HT/PCBM active layer as a function of etching times or depth on a Si substrate for a sample that was thermally annealed at 150 °C for 30 min, which is shown in Fig 2.10. The results indicate that PCBM was enriched at the Si substrate interface. This result demonstrates that the active layer/Si interface is different from the active layer/PEDOT: PSS interface (Fig 2.9b) due to the differences in the interfacial energies and the fact that interdiffusion can occur between the active layer and the PEDOT: PSS while Si is a hard interface.

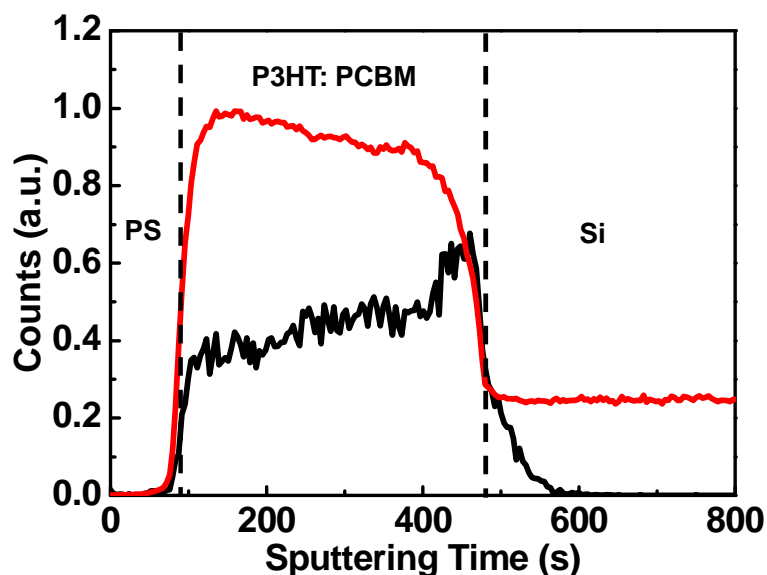


Figure 2.10 DSIMS of the P3HT/deuterated PCBM blend film on a silicon substrate annealed at 150 °C for 30 min. ‘S signal’ (red line); ‘D signal’ (black line).

2.3.5 Miscibility of P3HT and PCBM Measured by DSC

The segmental interaction parameter between P3HT and PCBM, could be determined from the melting point depression of P3HT with added PCBM by DSC.

P3HT melting point depression with adding different amount of PCBM was listed in Table 2.5.

Table 2.5 P3HT melting point depression with adding different amount of PCBM

PCBM Vol (%)	0	4.47	5.99	7.54	11.46	15.49
Melting Point (F)	513.22	510.3	509.83	509.1	506.67	504.69

Equation 1 describes the melting point depression due to mixing of the crystalline polymer and a diluent. The subscript 1 identified with the diluent and 2 with the crystalline polymer, V is the volume fraction, V_u is the molar volume of the repeating unit, χ_{12} is the segmental interaction parameter, and R is the gas constant (8.3144 J/K.mol).⁴⁸

$$\frac{1}{T_m} - \frac{1}{T_m^0} = \frac{R V_{2u}}{\Delta H_{2u} V_{1u}} [(1 - V_2) - \chi_{12} (1 - V_2)^2] \quad (1)$$

$$\chi_{12} = \frac{B V_{1u}}{R T} \quad (2)$$

$$\frac{1}{V_1} \left[\frac{1}{T_m} - \frac{1}{T_m^0} \right] = \frac{R V_{2u}}{\Delta H_{2u} V_{1u}} \left[1 - \frac{B V_{1u}}{R} \frac{V_1}{T_m} \right] \quad (3)$$

By plotting $\frac{1}{V_2} \left[\frac{1}{T_m} - \frac{1}{T_m^0} \right]$ as a function of $\frac{V_1}{T_m}$, $-\frac{B V_{1u}}{R}$ can be determined from the slope/intercept, as shown in Fig 2.11. As a result, $\chi_{12} = \frac{B V_{1u}}{R T} = -0.162$ at 150 °C.

Which indicating that P3HT and PCBM are quite miscible, which would argue that far more PCBM should be solubilized in the P3HT at 150 °C.

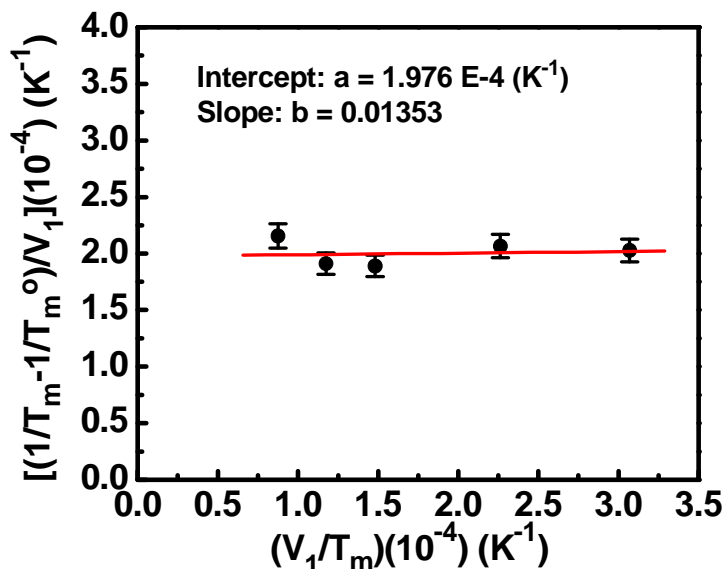


Figure 2.11 Plot of $\frac{1}{V_1} \left[\frac{1}{T_m} - \frac{1}{T_m^0} \right]$ as a function of $\frac{V_2}{T_m}$ for the P3HT/PCBM, where T_m is the melting point of the mixtures and T_m^0 is the equilibrium melting point of pure P3HT.

2.4 Conclusion

In conclusion we have quantitatively demonstrated, by TEM, SANS and GIXD, that the P3HT and PCBM phase separate upon thermal annealing into a bicontinuous morphology with a characteristic length scale of ~ 10 nm domains, where crystalline P3HT comprises one of the domains. For the “Post-Annealed” samples, GIXD and NEXAFS studies revealed a re-orientation in the packing of the P3HT at the cathode/active layer interface that is conducive for holes to flow; NEXAFS, and DSIMS studies showed a segregation of PCBM to the cathode/active layer interface and an interdiffusion at the PEDOT: PSS interface. PCBM and P3HT are shown to be quite miscible and a rather unusual diffusion of the PCBM into the P3HT is observed

indicative of a rapid diffusion of a small molecule into a crystalline network where the tie chains between the crystals limit the extent to which the PCBM can swell the P3HT. Distinct differences, especially the interfacial behavior, were observed between active layers thermally annealed before or after a cathode was evaporated onto the surface, where the latter is more relevant for the usual fabrication of PV devices. The variations in the bulk morphology, interfacial behavior and spatial variation of the components can be directly correlated to the performance of the device.

2.5 References

- (1) Yu, G.; Gao, J.; Hummelen, J. C.; Wudl, F.; Heeger, A. J. *Science* **1995**, *270*, 1789-1791.
- (2) Brabec, C. J.; Sariciftci, N. S.; Hummelen, J. C. *Adv. Funct. Mater.* **2001**, *11*, 15-26.
- (3) Thompson, B. C.; Frechet, J. M. J. *Angew. Chem. Int. Ed.* **2008**, *47*, 58-77.
- (4) Dennler, G.; Sariciftci, N. S. *Proceedings of the Ieee* **2005**, *93*, 1429-1439.
- (5) Campoy-Quiles, M.; Ferenczi, T.; Agostinelli, T.; Etchegoin, P. G.; Kim, Y.; Anthopoulos, T. D.; Stavrinou, P. N.; Bradley, D. D. C.; Nelson, J. *Nature Mater.* **2008**, *7*, 158-164.
- (6) Shaheen, S. E.; Brabec, C. J.; Sariciftci, N. S.; Padinger, F.; Fromherz, T.; Hummelen, J. C. *Appl. Phys. Lett.* **2001**, *78*, 841-843.
- (7) Park, S. H.; Roy, A.; Beaupre, S.; Cho, S.; Coates, N.; Moon, J. S.; Moses, D.; Leclerc, M.; Lee, K.; Heeger, A. J. *Nature Photon.* **2009**, *3*, 297-303.
- (8) Kim, Y.; Choulis, S. A.; Nelson, J.; Bradley, D. D. C.; Cook, S.; Durrant, J. R. *Appl. Phys. Lett.* **2005**, *86*, 063502.
- (9) Li, G.; Shrotriya, V.; Huang, J. S.; Yao, Y.; Moriarty, T.; Emery, K.; Yang, Y. *Nature Mater.* **2005**, *4*, 864-868.
- (10) Mihailetschi, V. D.; Xie, H. X.; de Boer, B.; Popescu, L. M.; Hummelen, J. C.; Blom, P. W. M.; Koster, L. J. A. *Appl. Phys. Lett.* **2006**, *89*, 012107.
- (11) Mayer, A. C.; Toney, M. F.; Scully, S. R.; Rivnay, J.; Brabec, C. J.; Scharber, M.; Koppe, M.; Heeney, M.; McCulloch, I.; McGehee, M. D. *Adv. Funct. Mater.* **2009**, *19*, 1173-1179.
- (12) van Bavel, S. S.; Barenklau, M.; de With, G.; Hoppe, H.; Loos, J. *Adv. Funct. Mater.* **2010**, *20*, 1458-1463.
- (13) Pivrikas, A.; Stadler, P.; Neugebauer, H.; Sariciftci, N. S. *Org. Electron.* **2008**, *9*, 775-782.
- (14) Peet, J.; Kim, J. Y.; Coates, N. E.; Ma, W. L.; Moses, D.; Heeger, A. J.; Bazan, G. C. *Nature Mater.* **2007**, *6*, 497-500.

- (15) Chen, H. Y.; Yang, H. C.; Yang, G. W.; Sista, S.; Zadoyan, R. B.; Li, G.; Yang, Y. *J. Phys. Chem. C* **2009**, *113*, 7946-7953.
- (16) Moule, A. J.; Meerholz, K. *Adv. Mater.* **2008**, *20*, 240-245.
- (17) Lee, J. K.; Ma, W. L.; Brabec, C. J.; Yuen, J.; Moon, J. S.; Kim, J. Y.; Lee, K.; Bazan, G. C.; Heeger, A. J. *J. AM. CHEM. SOC.* **2008**, *130*, 3619-3623.
- (18) Yao, Y.; Hou, J. H.; Xu, Z.; Li, G.; Yang, Y. *Adv. Funct. Mater.* **2008**, *18*, 1783-1789.
- (19) Wang, W. L.; Wu, H. B.; Yang, C. Y.; Luo, C.; Zhang, Y.; Chen, J. W.; Cao, Y. *Appl. Phys. Lett.* **2007**, *90*, 183512.
- (20) Ma, W. L.; Yang, C. Y.; Gong, X.; Lee, K.; Heeger, A. J. *Adv. Funct. Mater.* **2005**, *15*, 1617-1622.
- (21) Hoppe, H.; Sariciftci, N. S. *J. Mater. Chem.* **2006**, *16*, 45-61.
- (22) Yang, X. N.; Loos, J.; Veenstra, S. C.; Verhees, W. J. H.; Wienk, M. M.; Kroon, J. M.; Michels, M. A. J.; Janssen, R. A. J. *Nano Lett.* **2005**, *5*, 579-583.
- (23) Zhao, Y.; Xie, Z. Y.; Qu, Y.; Geng, Y. H.; Wang, L. X. *Appl. Phys. Lett.* **2007**, *90*, 043504.
- (24) Jo, J.; Na, S. I.; Kim, S. S.; Lee, T. W.; Chung, Y.; Kang, S. J.; Vak, D.; Kim, D. Y. *Adv. Funct. Mater.* **2009**, *19*, 2398-2406.
- (25) van Bavel, S. S.; Sourty, E.; de With, G.; Loos, J. *Nano Lett.* **2009**, *9*, 507-513.
- (26) Stohr, J., *NEXAFS spectroscopy*. Berlin ; New York : Springer-Verlag: **1992**.
- (27) Samant, M. G.; Stohr, J.; Brown, H. R.; Russell, T. P.; Sands, J. M.; Kumar, S. K. *Macromolecules* **1996**, *29*, 8334-8342.
- (28) Malik, S.; Nandi, A. K. *J. Polym. Sci. B.* **2002**, *40*, 2073-2085.
- (29) Osterbacka, R.; An, C. P.; Jiang, X. M.; Vardeny, Z. V. *Science* **2000**, *287*, 839-842.
- (30) Hashimoto, T.; Kumaki, J.; Kawai, H. *Macromolecules* **1983**, *16*, 641-648.
- (31) Russell, T. P.; Hadziioannou, G.; Warburton, W. K. *Macromolecules* **1985**, *18*, 78-83.

- (32) Keith, H. D.; Padden, F. J. *J. Appl. Phys.* **1963**, *34*, 2409-2421.
- (33) Verploegen Eric ; Mondal Rajib ; Bettinger J. Christopher; Sok Seihout; Toney F. Michael; Zhenan, B. *Adv. Funct. Mater.* **2010**, *20*, 3519–3529.
- (34) Parnell, A. J.; Dunbar, A. D. F.; Pearson, A. J.; Staniec, P. A.; Dennison, A. J. C.; Hamamatsu, H.; Skoda, M. W. A.; Lidzey, D. G.; Jones, R. A. L. *Adv. Mater.* **2010**, *22*, 2444-2447.
- (35) Kiel, J. W.; Kirby, B. J.; Majkrzak, C. F.; Maranville, B. B.; Mackay, M. E. *Soft Matter* **2010**, *6*, 641-646.
- (36) Sirringhaus, H.; Brown, P. J.; Friend, R. H.; Nielsen, M. M.; Bechgaard, K.; Langeveld-Voss, B. M. W.; Spiering, A. J. H.; Janssen, R. A. J.; Meijer, E. W.; Herwig, P.; de Leeuw, D. M. *Nature* **1999**, *401*, 685-688.
- (37) Kim, Y.; Cook, S.; Tuladhar, S. M.; Choulis, S. A.; Nelson, J.; Durrant, J. R.; Bradley, D. D. C.; Giles, M.; McCulloch, I.; Ha, C. S.; Ree, M. *Nature Mater.* **2006**, *5*, 197-203.
- (38) Chiu, M. Y.; Jeng, U. S.; Su, C. H.; Liang, K. S.; Wei, K. H. *Adv. Mater.* **2008**, *20*, 2573-2578.
- (39) Joshi, S.; Pingel, P.; Grigorian, S.; Panzner, T.; Pietsch, U.; Neher, D.; Forster, M.; Scherf, U. *Macromolecules* **2009**, *42*, 4651-4660.
- (40) Erb, T.; Zhokhavets, U.; Gobsch, G.; Raleva, S.; Stuhn, B.; Schilinsky, P.; Waldauf, C.; Brabec, C. J. *Adv. Funct. Mater.* **2005**, *15*, 1193-1196.
- (41) Kim, D. H.; Park, Y. D.; Jang, Y. S.; Yang, H. C.; Kim, Y. H.; Han, J. I.; Moon, D. G.; Park, S. J.; Chang, T. Y.; Chang, C. W.; Joo, M. K.; Ryu, C. Y.; Cho, K. W. *Adv. Funct. Mater.* **2005**, *15*, 77-82.
- (42) Germack, D. S.; Chan, C. K.; Hamadani, B. H.; Richter, L. J.; Fischer, D. A.; Gundlach, D. J.; DeLongchamp, D. M. *Appl. Phys. Lett.* **2009**, *94*, 233303.
- (43) Watts, B.; Belcher, W. J.; Thomsen, L.; Ade, H.; Dastoor, P. C. *Macromolecules* **2009**, *42*, 8392-8397.
- (44) Stohr, J.; Outka, D. A. *Phys. Rev. B.* **1987**, *36*, 7891-7905.
- (45) Bjorstrom, C. M.; Nilsson, S.; Bernasik, A.; Budkowski, A.; Andersson, M.; Magnusson, K. O.; Moons, E. *Appl. Surf. Sci.* **2007**, *253*, 3906-3912.
- (46) Wang, X. J.; Ederth, T.; Inganas, O. *Langmuir* **2006**, *22*, 9287-9294.

(47) Treat, N. D.; Brady, M. A.; Smith, G.; Toney, M. F.; Kramer, E. J.; Hawker, C. J.; Chabinyc, M. L. *Adv. Energy Mater.* **2010**, *1*, 82–89.

(48) Nishi, T.; Wang, T. T. *Macromolecules* **1975**, *8*, 909-915.

CHAPTER 3

BULK HETEROJUNCTION PHOTOVOLTAIC ACTIVE LAYERS VIA BILAYER INTERDIFFUSION

3.1 Introduction

Bulk heterojunction (BHJ) organic photovoltaic (OPV) devices are attracting significant attention and are regarded as the most promising technology for the plastic PV industry. They provide a general route to achieve large-area, low-cost, flexible and efficient devices due to a bicontinuous morphology that develops with a characteristic length scale comparable to the exciton diffusion length of ~ 10 nm.¹⁻⁶ Significant progress in BHJ solar cells has been made by the synthesis of low band gap conjugated polymers and optimization of the device preparation conditions, including the application of thermal annealing treatments⁷⁻⁹, solvent annealing¹⁰⁻¹², adding chemical additives¹³⁻¹⁹, adjusting the volume fractions of the components²⁰⁻²² and controlling the rate of solvent evaporation^{23, 24}. The efficiency of converting solar energy into electrical power within the plastic solar cells is still not high enough; the most efficient devices have the efficiencies of 7-8%^{25, 26}, recently Konarka Technologies, Inc. reported the organic device with efficiency 8.3%. To improve the efficiency of plastic solar cells, it is crucial to understand and control the morphology and identify routes to optimize the morphology for performance.

As in previous studies²⁷⁻³¹, optimization of the optical absorption, charge mobility and interpenetrating network morphology of the active layer is critical to

improve the device performance. The first two factors are gradually being improved by molecular engineering through the synthesis of new low band gap materials with the balanced transport compared to PCBM. However, understanding and controlling the morphology is still only beginning due, in part, to the difficulty in characterizing the structure and morphology. To further improve the device efficiency, it is essential to gain a fundamental understanding of the physical properties of the conjugated polymers and their interactions with PCBM. It is of particular importance to understand the mechanism by which the morphology of the active layer develops during standard processing conditions and to control the multiple kinetic processes involved to achieve the desired morphology. The non-equilibrium state of the morphology generated by spin coating or other solvent casting processes and the ordering of the conjugated polymer in the active layer, make controlling the morphology much more complex. It is also imperative that we gain a quantitative understanding of the miscibility of the components, the purity of the phases developed, and the interdiffusion of the components so as to fundamentally understand the mechanism of phase separation and ultimately control the active layer morphology to achieve higher device performance.

In our previous work²⁸ and in the work of others³²⁻³⁵ the interdiffusion of P3HT and PCBM under thermal annealing or solvent inducing was reported, yet the morphology developed and how diffusion enters into the development of the morphology by pure thermal annealing procedure has not been discussed. Here we used regio-regular poly(3-hexylthiophene) (P3HT) as a model conjugated polymer and [6,6]-phenyl C61- butyric acid methyl ester (PCBM) to study the interdiffusion and phase separation behavior of a proto-typical OPV active layer system. Multiple techniques

were used to develop an understanding of the diffusion behavior between the P3HT/PCBM bilayer system and the morphology. Transmission electron microscopy (TEM), grazing incidence small angle X-ray scattering (GISAXS), resonant soft X-ray scattering (RSoXS)^{36, 37} and small angle neutron scattering (SANS) were used to elucidate the development of bicontinuous morphology with a characteristic length scale of ~10-15 nm after interdiffusion between P3HT layer and PCBM layer. This morphology formed very rapidly, within seconds of annealing at 150 °C, and remained relatively unchanged with continued annealing. Dynamic secondary ion mass spectroscopy (DSIMS), grazing incidence x-ray diffraction (GIXD) and resonant soft x-ray reflectivity (RSoXR)³⁸⁻⁴², showed that the interdiffusion between P3HT and PCBM layers happens with a few second and the PCBM penetrates completely through the P3HT layer, even if the P3HT is ordered before the diffusion. The resultant morphology was the same in all cases. RSoXS/RSoXR shows the clear trend of the interdiffusion of PCBM into the P3HT with a very short annealing time. By combining these findings, a phase separation mechanism is proposed.

3.2 Experimental

3.2.1 Materials and Methods

Regioregular poly(3-hexylthiophene) (Mw = 42.4 k, Mn = 21.2 k, RR = 96.8%) and [6,6]-phenyl-C61-butyric acid methyl ester were obtained from Konarka Technologies. The Deuterated PCBM, ([6,6]-Pentadeuterophenyl C61 butyric acid methyl ester), was purchased from Sigma-Aldrich. The indium tin oxide (ITO)-coated glass substrates (20 ± 5 ohms/sq) were bought from Thin Film Devices Inc., and were

cleaned through ultrasonic treatment in detergent, DI water, acetone, and isopropyl alcohol and then dried in an oven overnight.

3.2.2 Forward Devices

PEDOT: PSS (CLEVIOS™ P VP Al 4083) (~ 35 nm) was spin-coated onto ultraviolet ozone-treated ITO substrates. After annealing at 150 °C for 30 min in air, the substrates were transferred to a glove box. P3HT solution in chlorobenzene (20 mg/ml) was then spun-coated onto the PEDOT: PSS covered substrates at the speed of 1300 rpm. The average thickness was 80 nm measured by Alpha Step IQ Surface Profilometer. The P3HT thin film was dried in vacuum oven overnight at room temperature to fully remove the residue solvent. Then the PCBM layer was spin-coated directly on top of the P3HT layer from a dichloromethane solution (10 mg/ml). This process was conducted as quickly as possible to minimize interface mixing. When the bilayer heterojunction was fabricated, thermal annealing was conducted at 150 °C with different time. A thin layer of LiF (1 nm) was fabricated on top of bilayer heterojunction by thermal evaporation at a speed of 0.1-0.2 Å/s and in the end, a 100 nm Aluminum was evaporated as the cathode.

3.2.3 Inverted Devices

ITO substrates were cleaned by conventional process and ultraviolet ozone-treated for 10 minutes. A zinc acetate [Zn(ac)] solution (15.7 mg/ml) in 96% 2-methoxy ethanol and 4% ethanolamine was spin-coated at 2000 rpm onto the ITO substrates. These substrates were annealed at 300 °C for 5 min in air to convert Zn(ac) into ZnO.

The resulting film was then rinsed in de-ionized water, acetone, and isopropanol to remove the residue organic materials on the surface and then dried at 120 °C overnight. The ZnO coated substrates were ultraviolet ozone-treated for 5 minutes and a thin layer of PCBM was spin-coated on top from its chlorobenzene solution (20 mg/mL) at the speed of 1300 rpm with an average thickness of 50 nm. Then the P3HT thin film (~80 nm) was floated onto PCBM layer. The bilayer heterojunction was washed with de-ionized water several times and dried in vacuum overnight. Subsequently, these bilayer thin films were annealed at 150 °C with different time. A 10 nm of MoO₃ was fabricated on top of the bilayer by thermal evaporation at the speed of 0.2-0.3 Å /s and a 50 nm of Au was evaporated as the anode.

3.2.4 Organic Solar Cell Devices Testing

All the devices were measured under simulated AM1.5G irradiation (100 mW cm⁻²) using a Xe lamp-based Newport 91160 300-W Solar Simulator. A Xe lamp equipped with an AM1.5G filter was used as the white light source. The light intensity was adjusted with an NREL-calibrated Si solar cell with a KG-5 filter. The current-voltage (I-V) characteristics were recorded using a Keithley 2400 source measure unit.

3.2.5 BF-STEM and TEM-EELS

BF-STEM and TEM-EELS cross sections were prepared using an FIB system (SII NanoTechnology Inc. SMI3200F) delivering a 30 keV beam of Ga⁺² ions. Carbon protective layer was deposited on the top surface before cutting out. The thickness of the specimen was ~ 100 nm. The BF-STEM analyses were carried out with Hitachi High-

Technologies S-5500 operating at 30 kV. The TEM-EELS imaging was performed at beam energy of 200kV using Hitachi High-Technologies HD-2700 with EV-3000.

3.2.6 Dynamic Secondary Ion Mass Spectrometry (DSIMS)

Dynamic Secondary Ion Mass Spectrometry (DSIMS) measurement was done by using the SIMS system: 6650 Quadrupole SIMS (Physical Electronics USA, Chanhassen, MN). Beam energy was 2 kV using O_2^+ ions as the primary ions, and the beam diameter was 20 microns, raster was 250 microns, accepting negatively-charged secondary ions from the center 15 percent of the crater area. Samples were thin enough that no charge compensation was needed. Base pressure was always below 1×10^{-9} torr.

3.2.7 Small-angle Neutron Scattering (SANS)

Small-angle Neutron Scattering (SANS) experiments were performed at the High Flux Isotope Reactor neutron scattering facility at Oak Ridge National Laboratories (ORNL) (CG-2 SANS). 10 multi-layers, were stacked together, where the neutron beam was delivered at normal incidence to the film surface, placing the scattering vector in the plane of the film.

3.2.8 Grazing Incidence Small Angle X-ray Scattering (GI-SAXS) and Grazing Incidence X-ray Diffraction (GIXD)

GI-SAXS and GIXD measurements were performed on Beamline 7.3.3 at the Advanced Light Source at the Lawrence Berkeley National Laboratory. The experimental set-up and sample cell were designed for the surface studies on thin films.

An X-ray beam impinged onto the sample at a grazing angle above and below the critical angle of the polymer film ($\alpha_c = 0.16$), but below the critical angle of the silicon substrate ($\alpha_c = 0.22$). The wavelength of X-rays used was 1.240 Å, and the scattered intensity was detected by using two-dimensional charge-coupled device (CCD) camera with image sizes of 2304 x 2304 pixels.

3.2.9 Resonant Soft X-ray Scattering (RSoXS)

RSoXS experiments were conducted at beamline 11.0.1.2. at Advanced Light Source (ALS), LBNL. Beamline 11.0.1.2 is a dedicated resonant soft x-ray scattering setup with Energy range of 100 eV – 1500 eV. The undulator source provides high flux and full polarization control. The energy resolution at carbon edge (~ 290 eV) is ~ 0.1 eV. For the P3HT/PCBM bilayer samples, RSoXS experiment was performed using a reflection geometry (analog to GISAXS). For the P3HT:PCBM blend samples, transmission geometry was used for the study. The scattering intensity was at different x-ray energies with a high-resolution in-vacuum CCD camera (PI-MTE form Princeton Instrument). The resulting two-dimensional scattering data were averaged azimuthally to obtain intensity at each q.

3.2.10 Resonant Soft X-ray Reflectivity (RSoXR)

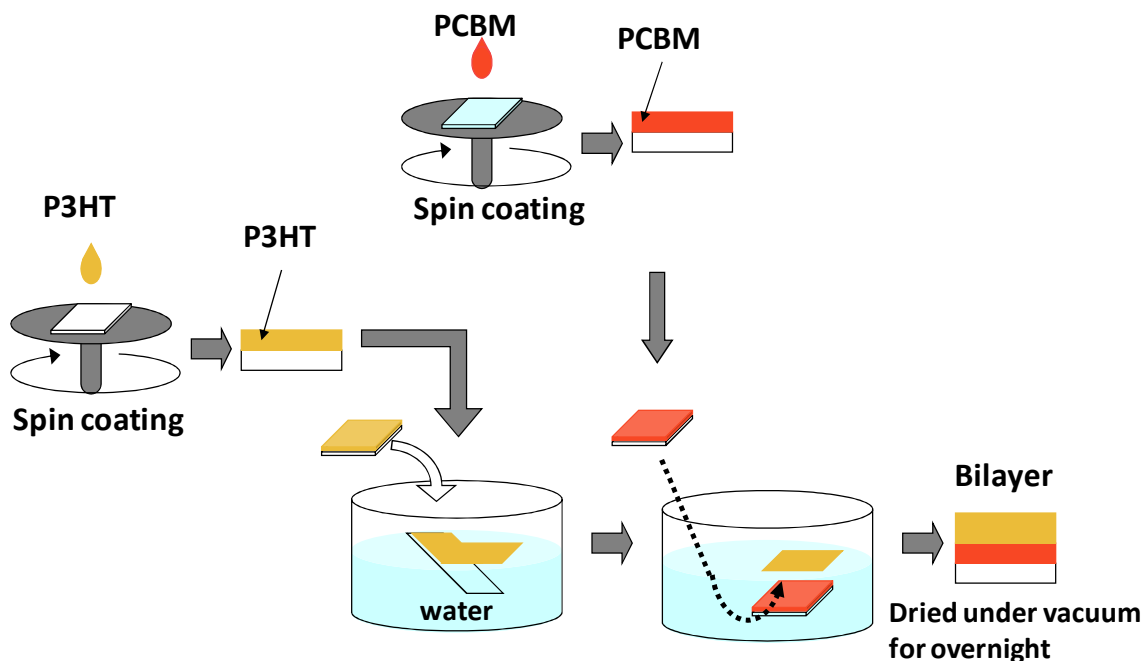
RSoXR measurements were performed at beamline 6.3.2 of the ALS. A channel electron multiplier detector was used for high S/N data collection using θ - 2θ scan geometry. For both RSoXS/RSoXR experiments, multiple photon energies were chosen for tuning the contrast and specific sensitivity at different interfaces. Fresh sample area

was used after previous scans to avoid radiation damage and multiple scans were performed to improve statistics.

3.3 Results and Discussion

3.3.1 P3HT/PCBM Bilayer Preparation

A schematic of the procedure used to prepare P3HT/PCBM bilayer is shown in Scheme 3.1. Pure P3HT and PCBM films were prepared by spinning coating the P3HT/chlorobenzene and PCBM/chlorobenzene onto silicon wafers. The P3HT film was then floated onto the surface of the deionized water, then retrieved with the PCBM-coated Si wafer, and the P3HT/PCBM bilayer was dried in vacuum oven overnight at room temperature. By using this floatation method, any solvent-induced interdiffusion is completely avoided and only the interdiffusion of the components by thermal annealing is observed^{34, 35}. The bilayer samples were heated to 150 °C for different periods of time and the concentration profiles of the components was measured to assess the interdiffusion and the morphology developed.



Scheme 3.1 Schematic diagram of preparation of P3HT/PCBM bilayer

3.3.2 Interdiffusion Behavior of P3HT/PCBM Bilayer

Shown in Figure 3.1 are a series of interdiffusion results for bilayers of P3HT (100 nm)/dPCBM (60 nm) after different annealing times at 150 °C. The DSIMS profiles monitor the variation in the elemental composition of a sample as a function of sputtering time which corresponds to depth in the film. A quantitative conversion of sputtering time to depth requires a calibration against that measured with the pure components and, while this was done, differences in the sputtering rate in the different components gives rise to a broadening when there are phase separated domains present. This is the case for P3HT and dPCBM and, as such, the profiles were left as a function of the sputtering time. In all the DSIMS experiments, the deuterium (D) signal (the solid lines) from dPCBM was used to locate the dPCBM, while the sulfur (S) signal (the solid star) was used as a marker for P3HT. In all cases, a sacrificial layer of polystyrene was

floated onto the surface of the active layer to allow the ion beam to establish a constant sputtering rate before etching in the active layer occurred. In Fig. 3.1a, the P3HT layer is the “As-Spun” film with no thermal treatment, initially, the interface between P3HT layer and dPCBM layer is sharp. However, after only 5 seconds of annealing at 150 °C, the dPCBM is seen to penetrate completely through the P3HT layer with a signal that is constant as a function of depth. After 5 minutes, it shows that the P3HT layer increased in thickness, due to the incorporation of PCBM, but the interface has not been broadened. However, the concentration of PCBM in the P3HT has only increased slightly and there is no variation with depth. In Fig. 3.1b, the P3HT layer (~100 nm) was preannealed on a mica substrate at 150 °C for 5 min prior to transfer onto the dPCBM coated Si substrate. The diffusion behavior is essentially the same as Fig. 3.1a, the only difference is that the concentration of dPCBM in the P3HT for the 5 sec sample is lower than that for the bilayer using the “As-Spun” P3HT which is understandable, since the volume fraction of the amorphous P3HT is less for the pre-ordered P3HT than for the “As-Spun” P3HT film. These results indicate that the PCBM can diffuse into an ordered P3HT layer very rapidly and the average composition is a constant. In addition, the PCBM is highly miscible with amorphous P3HT and that must be a continuous pathway of amorphous P3HT throughout the P3HT film after the P3HT has ordered.

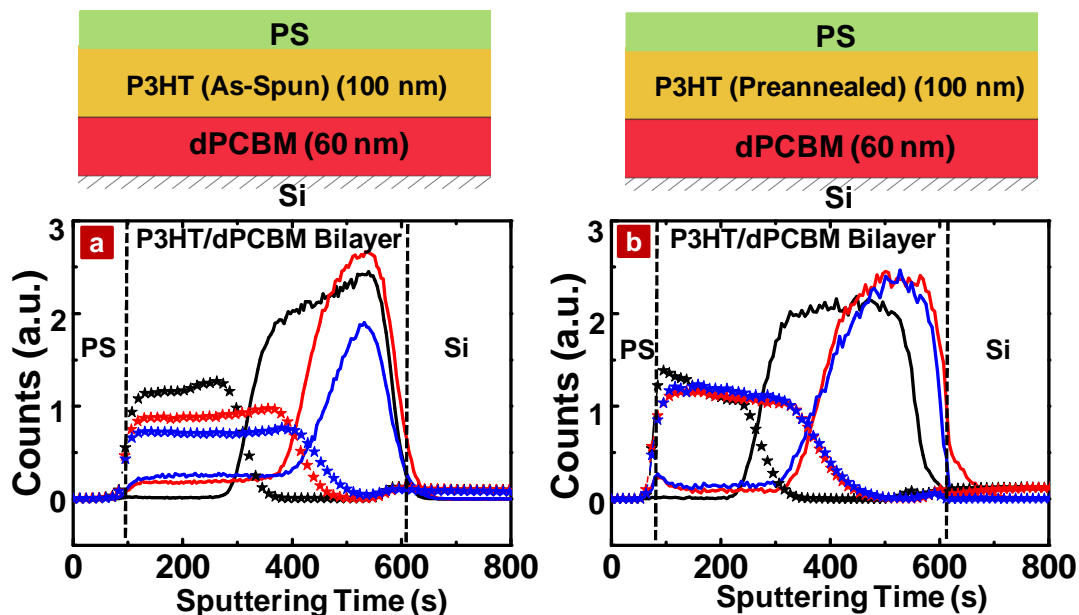


Figure 3.1 DSIMS of P3HT/dPCBM bilayer diffusion at 150 °C at different time **a**, “As Spun” P3HT/PCBM bilayer (after Figure 6e of ref 28); **b**, “Pre-Annealed” P3HT/PCBM bilayer; Annealed at 150 °C: 0 sec (black), 5 sec (red), 5 min (blue), ‘S signal’ (solid star); ‘D signal’ (solid line).

3.3.3 Morphology Development from P3HT/PCBM Bilayer Diffusion

Shown in Fig. 3.2 are TEM images of the cross-sections of the “As Spun” P3HT/PCBM bilayers with and without thermal annealing for 5 sec at 150 °C. The initial “As Spun” P3HT/PCBM bilayer sample shows a sharp interface between the two layers (Figure 3.2a), while, once the bilayer sample was annealed for only 5 sec, diffusion occurred and a bicontinuous morphology spans the entire film with domains ~10-15 nm in size (Figure 3.2b). This is virtually identical to the morphology obtained for a bulk P3HT/PCBM mixture after thermal annealing²⁸. Figure 3.2a and 3.2b were taken in the scanning transmission electron microscopy (STEM) bright field mode. To confirm that the morphology developed in the “5 s” sample consists of P3HT-rich and PCBM-rich domains, electron energy loss spectroscopy (EELS) was used to obtain the TEM image. Figure 3.2c is the S-core loss image, where the brighter regions are the

P3HT-rich domains, while the darker regions are the PCBM-rich region, since S is found only in the P3HT. Figure 3.2d is the C- core loss image. Here, the brighter regions are the PCBM-rich domains, while the darker regions are the P3HT-rich domains, since the density of carbon in PCBM is much higher than in P3HT. Figure 3.2e, an overlap of the images in Figure 3.2c and 3.2d, is uniform in the P3HT/PCBM layer as would be expected due to the complementarity of the domains. Figure 3.2b, 3.2c and 3.2d indicate that the bicontinuous morphology develops in a few seconds of annealing at 150 °C for the “As Spun” P3HT/PCBM bilayer sample. Also, it can be seen that PCBM penetrates completely through the P3HT layer, which is consistent with DSIMS results.

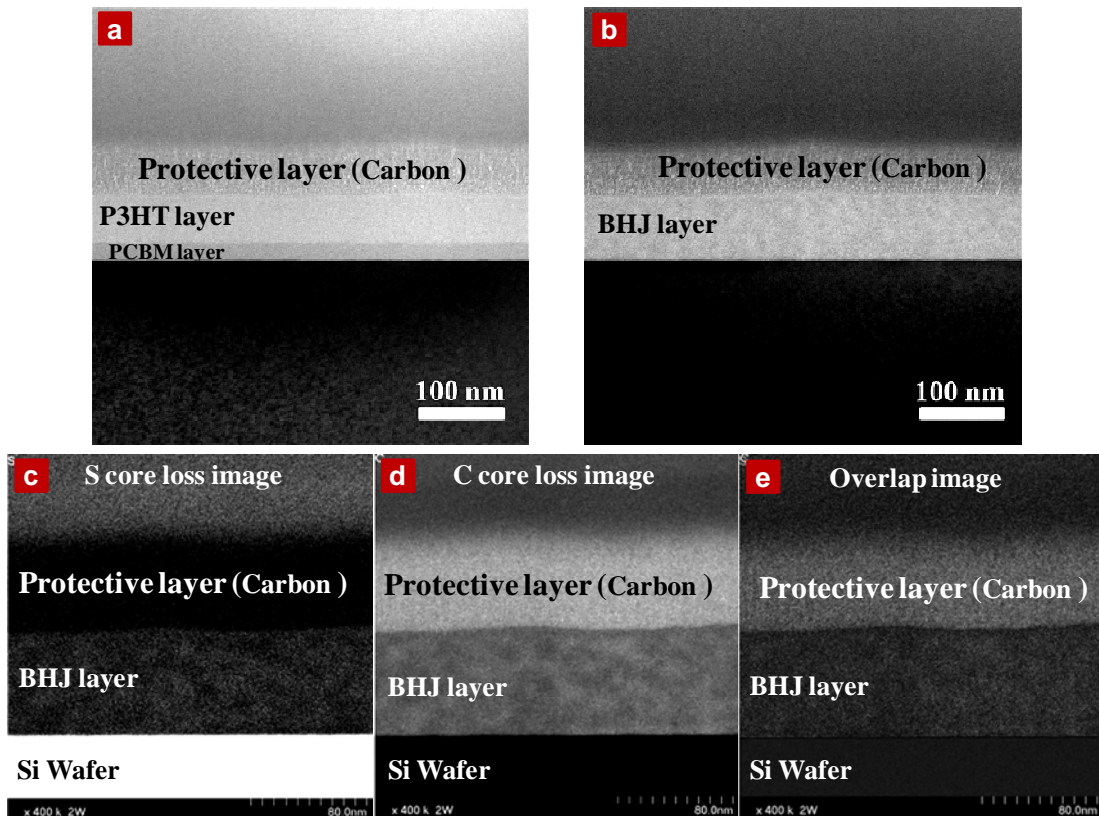


Figure 3.2 TEM of cross-sections of “As Spun” P3HT/PCBM bilayer diffusion at 150 °C for different time. **a**, Bright field STEM, annealed for “0 s”; **b**, Bright field STEM, annealed for “5 s”; **c**, S core loss image, annealed for “5 s”; **d**, C core loss image, annealed for “5 s”; **e**, Overlap image of image “c” and “d”.

GIXD, Shown in Fig. 3.3a, was used to determine the ordering of the P3HT in the thin films. 0.18° was used as the incidence angle, which is above the critical angle (0.16°), to probe the bulk ordering of the P3HT. The data shown in Figure 3.3 is the out-of-plane scattering, i.e. characterizing the ordering normal to the sample surface. The GIXD profiles from both the “Pure P3HT film” and the “As Spun” P3HT/PCBM bilayer sample (Figure 3.3a) show the (100) reflection, along with a second (200) and a third order (300) reflections, which indicate that the edge-on crystal structure is prevalent in these samples²⁸. The reflections get stronger and sharper with increasing annealing time. By using the Scherrer’s equation^{43, 44} the sizes of crystals along the (100) direction, can be determined from the full width at half-maximum of the reflections, and are summarized in Table 3.1. The crystal size increases from ~19 nm to ~25 nm with increasing annealing time. The reflections from the “Pre-Annealed” P3HT /PCBM bilayer sample do not change much with annealing time, which indicates that the P3HT chain packing has already developed fully during the preannealing process and the crystal size remained constant at ~ 25 nm. These results show that the diffusion of the PCBM into the P3HT did not disrupt the morphology established by the P3HT. The crystal size is very close to the domain size measured by TEM, which suggests that one of the phases in the active layer observed in TEM experiments, is a highly ordered P3HT phase. The GIXD results in Figure 3.3b, obtained below the critical angle (0.12°), were used to characterize the ordering of the P3HT at the surface of the film, i.e. within the first ~10 nm from the surface. For the “As Spun” P3HT/PCBM bilayer sample and the “Pre-Annealed” P3HT /PCBM bilayer sample, without thermal annealing, there are

no interference arising from PCBM, since the thickness of the P3HT layer is ~100 nm. After annealing the bilayers at 150 °C for only 5 sec, an interference arising from the PCBM ($q = 1.41 \text{ \AA}^{-1}$) was observed, which indicates that PCBM has penetrated through the entire P3HT layer, even the “Pre-annealed” P3HT layer, within a few seconds, which is consistent with the DISIMS and TEM data. The GIXD data also indicate that the PCBM diffusion within the P3HT film must happen in the amorphous P3HT regions, since the GIXD arising from the P3HT has remained unchanged during the PCBM diffusion. The fact that the morphology of the P3HT/PCBM layer is the same, whether the PCBM is diffused into the P3HT after the P3HT was ordered or if the P3HT was ordered from a homogenous mixture of P3HT and PCBM is noteworthy²⁸, and opens an interesting route to generate the bulk heterojunction (BHJ) morphology by a simple diffusion of the PCBM into the P3HT. This process also imparts control over the distribution of the PCBM in the P3HT and enables the specific placement of a PCBM-rich layer at the cathode interface.

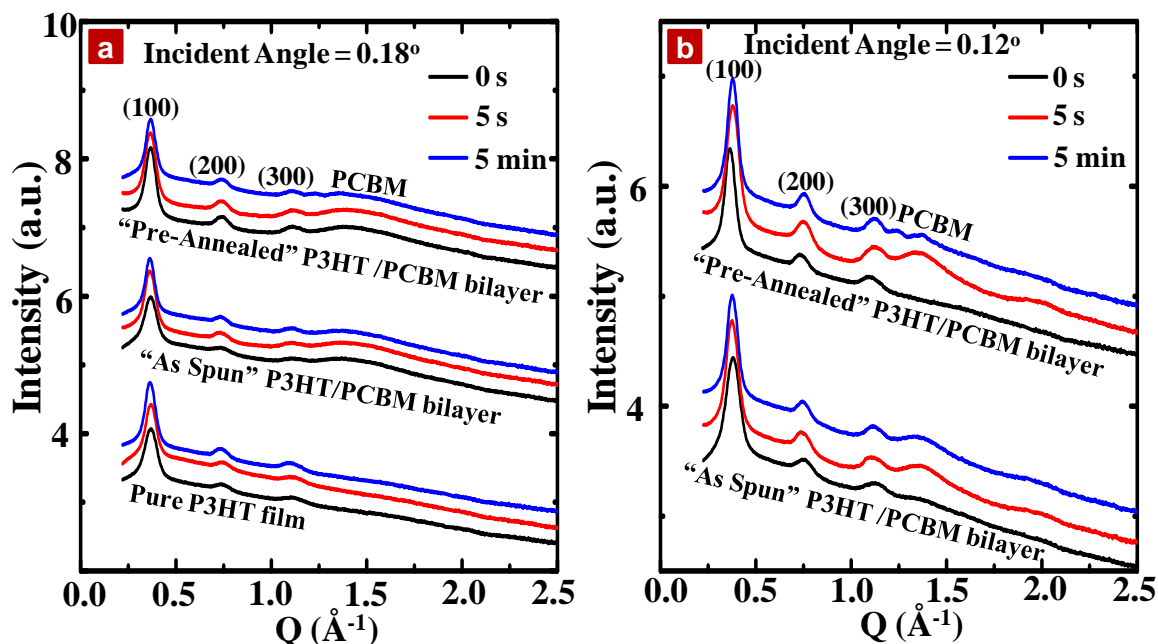


Figure 3.3 GIXD curves of P3HT/PCBM bilayers annealed at 150 °C for different time. “Pure P3HT layer”; “As Spun” P3HT/PCBM bilayer; “Pre-Annealed” P3HT/PCBM bilayer. **a**, Incident angle = 0.18°; **b**, Incident angle = 0.12°

Table 3.1 FWHM and crystal sizes of the P3HT annealed at 150 °C for different time

Annealed time	Pure P3HT Layer			“As Spun” P3HT/PCBM Bilayer			“Pre-Annealed” P3HT/PCBM Bilayer		
	0 s	5 s	5 min	0 s	5 s	5 min	0 s	5 s	5 min
FWHM (100) Å ⁻¹	0.0596	0.0510	0.0461	0.0605	0.0494	0.0437	0.0443	0.0462	0.0447
Crystal size (100) (nm)	19.0	22.1	24.6	18.7	22.9	25.9	25.5	24.5	25.3

Grazing incidence small angle X-ray scattering (GISAXS) and resonant soft X-ray scattering (RSoXS) were used to monitor the morphology development of the P3HT/PCBM bilayer samples with thermal annealing at 150 °C. Figure 3.4 shows the

in-plane scattering, where the scattering vector is oriented in the plane of the film. The electron density difference between the P3HT and PCBM provides sufficient contrast to observe the scattering arising from the phase separated morphology. In Figure 3.4a the GISAXS from, the “As Spun” P3HT /PCBM bilayer sample shows a monotonically decreasing profile in the initial bilayer sample. When the sample was annealed at 150 °C for only 5 sec, a peak in the GISAXS profile is seen at $q=0.028 \text{ \AA}^{-1}$. With continued annealing at 150 °C for 5 minutes, the maximum in the scattering gets more intense and shifts slightly to the lower q , due to the incorporation of the PCBM into P3HT. This trend is much more obvious in the “Pre-Annealed” P3HT/PCBM bilayer sample. These results indicate the bicontinuous morphology was developed within a few seconds and the sizes of the domains did not change much with annealing time. The increase in the intensity suggests that the phases become more pure with time, i.e. the electron density difference between the domains is increasing. These samples were also investigated with R-SoXS (Figure 3.4d). A photon energy of 283 eV was used to provide maximum contrast between the P3HT-rich phase and the PCBM-rich phase. The scattering profiles are consistent with the GISAXS data (Figure 3.4a). From the peak position in the GISAXS and R-SoXS profiles, an average domain size of ~11 nm is found. For the “Pre-Annealed” P3HT/PCBM bilayer sample, both the GISAXS (Figure 3.4b) and R-SOXS (Figure 3.4e) scattering profiles were essentially the same as those from the “As-Spun” P3HT/PCBM bilayer. The scattering from the “Pre-Annealed” P3HT/PCBM bilayer (5 sec) is slightly lower compared with the “As Spun” P3HT/PCBM bilayer (5 sec), due simply to the lower concentration of PCBM in the P3HT, which is consistent with the DSIMS data. These results indicate that PCBM can

even penetrate through the pre-ordered P3HT very rapidly without perturbing the bicontinuous morphology and that the PCBM must diffuse into the P3HT film at the grain boundaries between the ordered P3HT without perturbing the ordering of the P3HT. The GISAXS and R-SoXS profiles for the P3HT/PCBM blend samples are shown in Figure 3.4c and Figure 3.4f, respectively. These data show a broader maximum, centered at $q=0.018 \text{ \AA}^{-1}$ with an average domain size $\sim 17 \text{ nm}$, compared with the bilayer interdiffusion samples.

The RSoXR (Figure 3.4g, h, and i) was used to characterize the diffusion of PCBM into the P3HT. Specular x-ray reflectivity measures the electron density profiles normal to the sample surface, and with RSoXR, the energy can be tuned to enhance the contrast for specific elements in the sample and, as such, can provide information on the concentration profiles normal to the film surface. RSoXR data was taken at 283 eV for to enhance the contrast at the P3HT/PCBM interface. Figure 4g shows the RSoXR form the “As Spun” P3HT/PCBM bilayer sample. Kiessig fringes with two distinct fringe spacing were observed, which arise from interferences from the Vacuum/P3HT and PCBM/Si interfaces. The dominant fringe spacing is $\sim 0.04 \text{ nm}^{-1}$, which correspond to the thickness of the total bilayer of $\sim 163 \text{ nm}$. Smaller fringes are seen at lower q ($< 0.3 \text{ nm}^{-1}$) that damped at higher q goes higher, indicating that the surface of the P3HT in the bilayer is rough. The larger fringes, with a spacing of $\sim 0.09 \text{ nm}^{-1}$ are due to interferences from the P3HT/PCBM, PCBM/Si interfaces, yields a PCBM film thickness of $\sim 70 \text{ nm}$. The fringes amplitude is damped at higher q which is characteristic of the roughness at the P3HT/PCBM interface. After annealing for 5 seconds, the smaller fringes are getting more visible at higher q , this indicating that bilayer surface becomes smoother, which

would be expected. On the other hand, the amplitude of the larger fringes has decreased significantly, indicating a reduction in the electron density differences at the interfaces, which would be expected if the PCBM diffused further through the P3HT layer. The fact that the interferences have sharpened also indicates that the interface between the P3HT and PCBM has remained sharp. After further annealing for 5 minutes, the small fringes corresponding to the bilayer become a bit more evident, in comparison to those measured at 5 seconds, and the large fringes (PCBM) completely disappeared. These results clearly show that the bilayer nature of the sample has vanished, due to the complete interdiffusion of the P3HT and PCBM and that a uniform layer is formed.

Figure 3.4h shows the RSoXR form the “Pre-Annealed” P3HT/PCBM bilayer” sample. The initial bilayer shows Kiessig fringes corresponding to both the bilayer and PCBM bottom layer. The higher frequency fringes, corresponding to the bilayer, are much sharper and more clear at a higher q , in comparison to the “As-Spun” P3HT/PCBM bilayer discussed above, which indicates that the preannealed P3HT has a much smoother surface and sharper interface with PCBM. The latter is also reflected in the persistence of the lower frequency fringes out to higher q . After 5 sec of annealing, the PCBM has diffused into the P3HT, reducing the amplitude of the fringes at higher q . In this case, though, the bilayer surface appears to have roughened. Further annealing for 5 minutes results in a loss of all the fringes, indicating the full penetration of PCBM into the P3HT. Figure 3.4i shows the RSoXR form the “P3HT: PCBM blend” sample. As would be expected for a uniform thin film, Kiessig fringes with one frequency are seen, corresponding to a film thickness of ~ 101 nm. With annealing, the fringes become sharper, indicating that the film has become smoother with annealing.

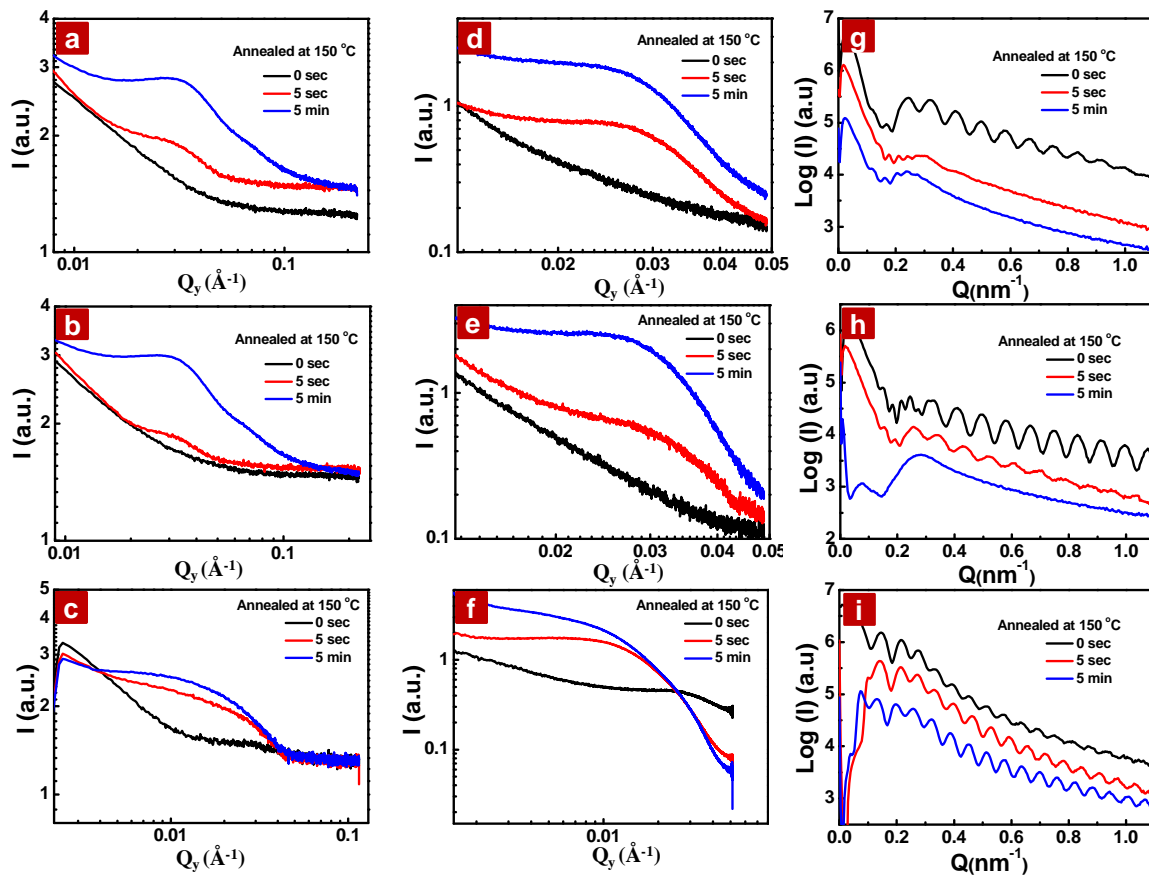


Figure 3.4 GISAXS, R-SoXS, RSoXR of P3HT/PCBM bilayer and P3HT/PCBM blend annealed at 150 °C at different time. **a**, GISAXS of “As Spun” P3HT/PCBM bilayer; **b**, GISAXS of “Pre-Annealed” P3HT/PCBM bilayer; **c**, GISAXS of P3HT:PCBM blend; **d**, R-SoXS of “As Spun” P3HT/PCBM bilayer; **e**, R-SoXS of “Pre-Annealed” P3HT/PCBM bilayer; **f**, R-SoXS of P3HT:PCBM blend; **g**, RSoXR of “As Spun” P3HT/PCBM bilayer; **h**, RSoXR of “Pre-Annealed” P3HT/PCBM bilayer; **i**, RSoXR of P3HT:PCBM blend; Annealed at 150 °C: 0 sec (black), 5 sec (red), 5 min (blue).

Small angle neutron scattering (SANS) offers another means to characterize the bulk morphology of the biayers. The previous studies^{28, 45, 46} have already shown that the scattering length density of PCBM is significantly different from P3HT, which provide a large neutron contrast between the P3HT rich and PCBM rich domain. Since the neutron beam impinges on the sample at normal incidence, the diffraction vector is in

the plane of the film which corresponds to the same direction as that observed in the transmission RSoXS experiments. The SANS from the “0 s” bilayer sample is shown in Fig. 3.5 where monotonically decreasing profile was observed. If the interface between the P3HT and PCBM was infinitely sharp, with the exception of an angularly independent incoherent scattering, there should be no SANS. The scattering observed can have two origins. The first is non-uniformities in the PCBM layer, while the second is roughness at the PCBM/P3HT interface, where height fluctuations at the interface will give rise to in-plane correlation in the neutron scattering length density (Figure 3.6). However, after only 5 seconds of heating at 150 °C, a significant increase in the SANS is seen and a shoulder at $q \sim 2.8 \times 10^{-2} \text{ \AA}^{-1}$ is observed. This corresponds to an average domain size of 11.2 nm was found. These results are in good agreement with the results by other methods. Further heating the bilayer sample (5 min) lead to a slight increase in the SANS intensity, while the peak position only shifts slightly to the lower q . Again, the SANS results show that the morphology develops very rapidly and that the dominant change with further annealing is a purification of the domains.

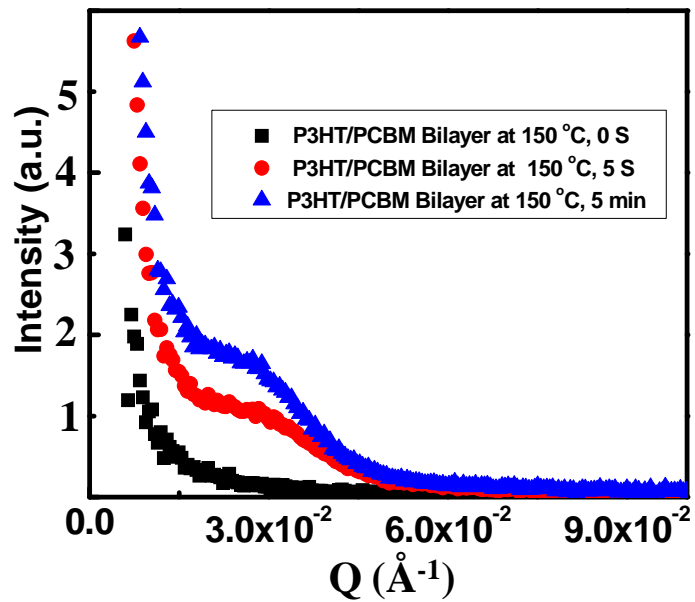


Figure 3.5 SANS profiles of “As Spun” P3HT/PCBM bilayer diffusion at 150 °C at different time. “0 s”, (black triangle); 5 sec (red triangle); 5 min (blue triangle).

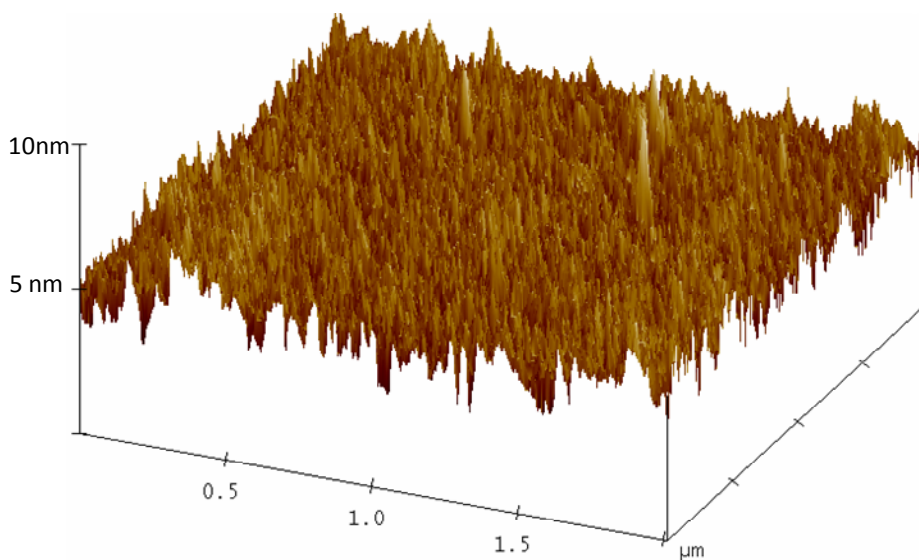


Figure 3.6 Surface roughness of PCBM film (AFM)

3.3.4 Device Performance Based on P3HT/PCBM Bilayer

Photovoltaic devices with both conventional and inverted structures using the bilayer-annealing preparation method were prepared. For the forward device, a PEDOT:PSS layer was cast onto ITO glass. Then, an 80 nm layer of P3HT was cast from chlorobenzene solutions onto the PEDOT:PSS and dried in vacuum at room temperature overnight. After that, the PCBM solution in dichloromethane was spin-coated onto the P3HT layer as rapidly as possible to form a PCBM layer. The bilayer structure was then annealed at 150 °C for different times. A control device (P3HT:PCBM blend) was fabricated by the normal BHJ device fabrication process. A thin layer of LiF and Al was then evaporated onto the surface as the cathode. The device performances are summarized in Figure 3.7a and Table 3.2. It is clear that the originally formed bilayer is not optimal, as would be expected, characterized by a relatively small V_{oc} and J_{sc} . Yet, after only a few seconds of annealing at 150 °C the device performance is dramatically improved (both V_{oc} and J_{sc}), which correlates well with the development of a two-phase morphology with the diffusion of PCBM into the P3HT layer to form the standard bulk heterojunction structure. The device annealed for 30s showed the best performance, close to that of the bulk heterojunction control device, which may be a result of the purification of the phases as indicated by the results from different techniques.

While the device prepared from the “As-Spun” bilayer shows the diffusion induced bulk heterojunction morphology, there may be some mixing at the P3HT/PCBM interface during the spin-coating PCBM layer, since DCM is a marginal

solvent for P3HT and it could dissolve low molecular weight P3HT and swell the P3HT film.³⁴ Therefore, inverted bilayer devices were prepared using the floatation method to avoid this possibility. A ZnO layer was prepared on ITO glass using a previously reported process.⁴⁷ PCBM was directly spin-coated onto the ZnO layer and then annealed at 150 °C for 2 minute to remove residual solvent. Subsequently, a P3HT thin film was floated onto the PCBM layer as described previously. The bilayer was dried in vacuum overnight at room temperature. The bilayer device was annealed at 150 °C for different periods of time and then thin layers of MoO₃ and Au were evaporated onto the surface to form the anode. The device data is summarized in Figure 3.7b and Table 3.2. These devices showed the same trend as the “As-Spun” bilayer devices. While the unannealed device showed a very small J_{sc}, after only a few seconds of annealing, markedly improvements in the J_{sc}, were observed, due to the formation of the BHJ structure. It was also found that the dark current increased for the annealed devices, due to the formation of the interpenetrating morphology and ordering of the P3HT (Figure 3.8).

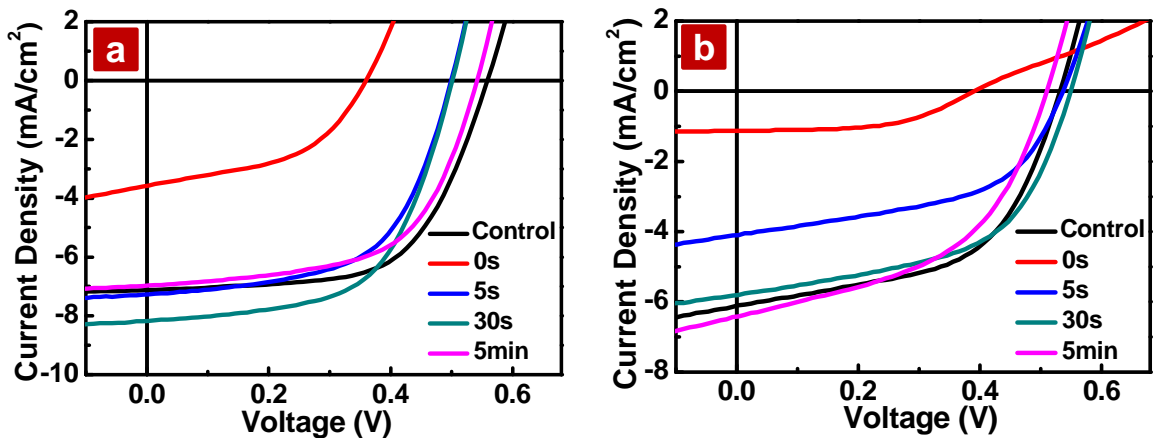


Figure 3.7 Devices based on P3HT/PCBM bilayer: **a**, Forward devices; **b**, Inverted devices.

Table 3.2. Summary of Device Performance

		V_{oc} (V)	J_{sc} (mA/cm ²)	FF (%)	PCE (%)
Foward device	Blend (5min)	0.56	7.11	62.07	2.47
	0s	0.36	3.57	47.79	0.61
	5s	0.50	7.25	58.50	2.12
	30s	0.50	8.16	59.06	2.41
	5min	0.54	6.95	59.45	2.24
Inverted device	Blend (5min)	0.53	6.12	54.46	1.77
	0s	0.39	1.13	53.90	0.24
	5s	0.54	4.10	51.53	1.13
	30s	0.55	5.80	54.13	1.72
	5min	0.51	6.42	48.53	1.59

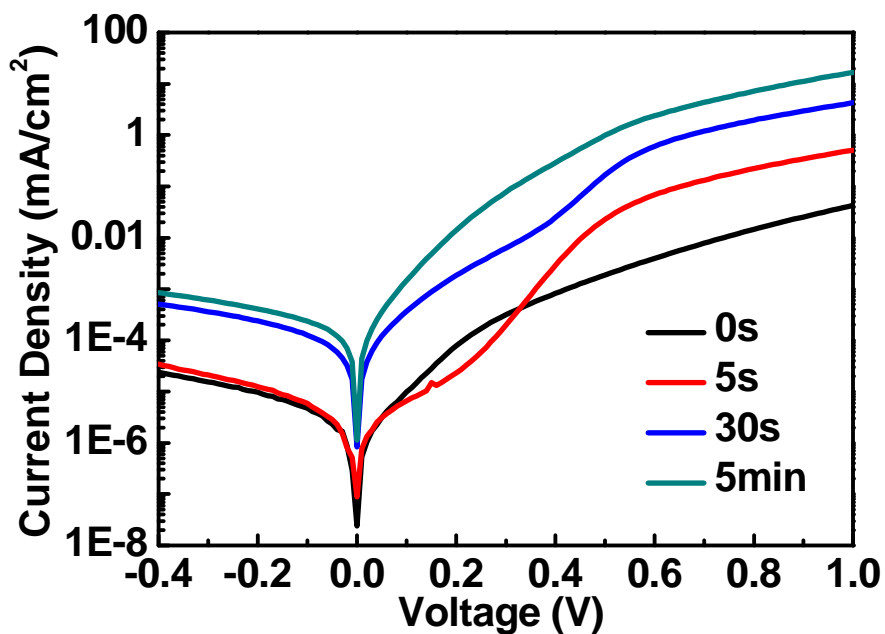


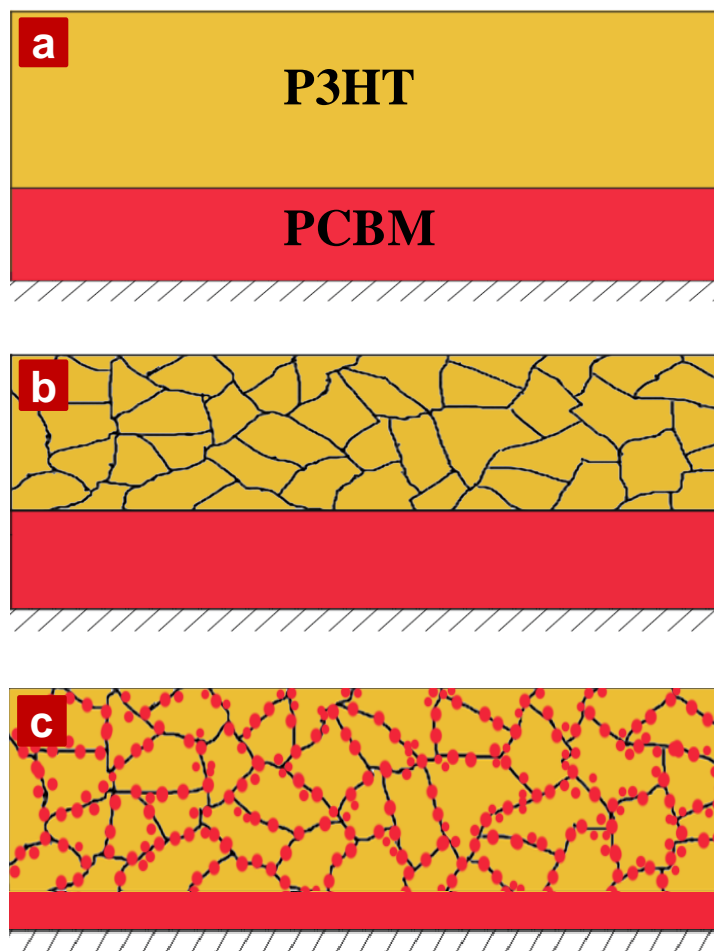
Figure 3.8 Dark currents based on P3HT/PCBM bilayer after different thermal annealing time at 150 °C.

3.3.5 Mechanism of P3HT/PCBM Bilayer Diffusion

Based on the results reported here, we can propose a mechanism for the diffusion of the PCBM into the P3HT. First, whether the P3HT is initially ordered or not, the resultant morphology is the same. Consequently, we can conclude that the ordering of the P3HT occurs on a time scale that is much more rapid than the diffusion of the PCBM into the P3HT. Therefore, the PCBM must diffuse into a framework established by the ordered domains of the P3HT. Secondly, the diffusion of the PCBM into the P3HT does not disrupt the ordered regions of the P3HT, as evidenced by GIXD and the fundamental size scales of the domains remains constant, as evidenced by the GISAXS, R-SoXS and SANS results. Consequently, the PCBM must diffuse into disordered regions along the grain boundaries between the ordered P3HT domains. Thirdly, the PCBM rapidly diffuses into the P3HT layer where the concentration does not vary with depth and the interface between the P3HT and PCBM remains sharp. Fourthly, measurements of the melting point depression clearly indicate that PCBM is very soluble in the amorphous or molten P3HT²⁸. So, shown in Scheme 3.2, grain boundaries are formed when the P3HT nucleates and orders into domains that are tens of nanometers in size, due to the truncation with other ordered P3HT growth fronts. The PCBM then diffuses rapidly into this inter-granular network, driven by the high solubility of PCBM in P3HT and, possibly, capillary force. Since the total volume available for the diffusion is small, the penetration of the P3HT occurs very rapidly without a significant swelling of the P3HT layer. When the PCBM reaches the air surface, the PCBM can crystallize, as was evidenced in studies from our own laboratories and others. In addition, since the concentration of the PCBM would be high

in the inter-granular regions, the PCBM can, with time, crystallize, causing deterioration in the performance of the active layer which has also been observed previous.

One final point that needs to be addressed is the similarity in the morphologies of the mixtures and that obtained by diffusing the PCBM into a pre-ordered P3HT. The only real difference is that, in the case of the mixtures, the size of the domains is somewhat larger. It is apparent that the morphology observed in the P3HT/PCBM system arises from the ordering of the P3HT and the rejection of the PCBM from the growth front of the P3HT crystal. While the ratio of the diffusion coefficient to the growth rate yields a characteristic distance, one must also consider the nucleation density. The fact that the blend films have a larger characteristic size scale can easily be attributed to a reduction in the nucleation density, thereby giving rise to the larger domains. It is apparent, though, that a phase separation mechanism, like spinodal phase separation, cannot account for the observations here.



Scheme 3.2 Schematic diagram of the mechanism of P3HT/PCBM bilayer diffusion: **a**, “As Spun” P3HT/PCBM bilayer; **b**, P3HT crystallizes after short time thermal annealing; **c**, PCBM diffuses into P3HT film through the P3HT amorphous domains.

3.4 Conclusion

In summary, amorphous P3HT and PCBM are shown to be highly miscible at 150 °C. In the P3HT/PCBM bilayer sample, PCBM can completely diffuse into the P3HT layer, even a pre-ordered P3HT layer, without perturbing the ordering of the P3HT. A bulk heterojunction morphology was developed by the diffusion of the PCBM into the P3HT after annealing at 150 °C for only a few seconds, which is similar to conventional BHJ morphology. This finding provides a new method to fabricate BHJ solar cells devices, which can also be applied to layer to layer lamination and roll to roll processes.

3.5 Reference

- (1) Brabec, C. J.; Sariciftci, N. S.; Hummelen, J. C. *Adv. Funct. Mater.* **2001**, *11*, 15-26.
- (2) Yu, G.; Gao, J.; Hummelen, J. C.; Wudl, F.; Heeger, A. J. *Science* **1995**, *270*, 1789-1791.
- (3) Spanggaard, H.; Krebs, F. C. *Sol. Energy Mater. Sol. Cells.* **2004**, *83*, 125-146.
- (4) Halls, J. J. M.; Pichler, K.; Friend, R. H.; Moratti, S. C.; Holmes, A. B. *Appl. Phys. Lett.* **1996**, *68*, 3120-3122.
- (5) Markov, D. E.; Amsterdam, E.; Blom, P. W. M.; Sieval, A. B.; Hummelen, J. C. *J. Phys. Chem. A.* **2005**, *109*, 5266-5274.
- (6) Markov, D. E.; Tanase, C.; Blom, P. W. M.; Wildeman, J. *Phys. Rev. B: Condens. Matter.* **2005**, *72*, 6.
- (7) Ma, W. L.; Yang, C. Y.; Gong, X.; Lee, K.; Heeger, A. J. *Adv. Funct. Mater.* **2005**, *15*, 1617-1622.
- (8) Hoppe, H.; Sariciftci, N. S. *J. Mater. Chem.* **2006**, *16*, 45-61.
- (9) Yang, X. N.; Loos, J.; Veenstra, S. C.; Verhees, W. J. H.; Wienk, M. M.; Kroon, J. M.; Michels, M. A. J.; Janssen, R. A. J. *Nano Lett.* **2005**, *5*, 579-583.
- (10) Zhao, Y.; Xie, Z. Y.; Qu, Y.; Geng, Y. H.; Wang, L. X. *Appl. Phys. Lett.* **2007**, *90*, 043504.
- (11) Jo, J.; Na, S. I.; Kim, S. S.; Lee, T. W.; Chung, Y.; Kang, S. J.; Vak, D.; Kim, D. Y. *Adv. Funct. Mater.* **2009**, *19*, 2398-2406.
- (12) van Bavel, S. S.; Sourty, E.; de With, G.; Loos, J. *Nano Lett.* **2009**, *9*, 507-513.
- (13) Pivrikas, A.; Stadler, P.; Neugebauer, H.; Sariciftci, N. S. *Org. Electron.* **2008**, *9*, 775-782.
- (14) Peet, J.; Kim, J. Y.; Coates, N. E.; Ma, W. L.; Moses, D.; Heeger, A. J.; Bazan, G. C. *Nature Mater.* **2007**, *6*, 497-500.
- (15) Chen, H. Y.; Yang, H. C.; Yang, G. W.; Sista, S.; Zadoyan, R. B.; Li, G.; Yang, Y. *J. Phys. Chem. C.* **2009**, *113*, 7946-7953.
- (16) Moule, A. J.; Meerholz, K. *Adv. Mater.* **2008**, *20*, 240-245.

- (17) Lee, J. K.; Ma, W. L.; Brabec, C. J.; Yuen, J.; Moon, J. S.; Kim, J. Y.; Lee, K.; Bazan, G. C.; Heeger, A. J. *J. AM. CHEM. SOC.* **2008**, *130*, 3619-3623.
- (18) Yao, Y.; Hou, J. H.; Xu, Z.; Li, G.; Yang, Y. *Adv. Funct. Mater.* **2008**, *18*, 1783-1789.
- (19) Wang, W. L.; Wu, H. B.; Yang, C. Y.; Luo, C.; Zhang, Y.; Chen, J. W.; Cao, Y. *Appl. Phys. Lett.* **2007**, *90*, 183512.
- (20) Park, S. H.; Roy, A.; Beaupre, S.; Cho, S.; Coates, N.; Moon, J. S.; Moses, D.; Leclerc, M.; Lee, K.; Heeger, A. J. *Nature Photon.* **2009**, *3*, 297-303.
- (21) Mayer, A. C.; Toney, M. F.; Scully, S. R.; Rivnay, J.; Brabec, C. J.; Scharber, M.; Koppe, M.; Heeney, M.; McCulloch, I.; McGehee, M. D. *Adv. Funct. Mater.* **2009**, *19*, 1173-1179.
- (22) van Bavel, S. S.; Barenklau, M.; de With, G.; Hoppe, H.; Loos, J. *Adv. Funct. Mater.* **2010**, *20*, 1458-1463.
- (23) Li, G.; Shrotriya, V.; Huang, J. S.; Yao, Y.; Moriarty, T.; Emery, K.; Yang, Y. *Nature Mater.* **2005**, *4*, 864-868.
- (24) Mihailetschi, V. D.; Xie, H. X.; de Boer, B.; Popescu, L. M.; Hummelen, J. C.; Blom, P. W. M.; Koster, L. J. A. *Appl. Phys. Lett.* **2006**, *89*, 012107.
- (25) Chen, H. Y.; Hou, J. H.; Zhang, S. Q.; Liang, Y. Y.; Yang, G. W.; Yang, Y.; Yu, L. P.; Wu, Y.; Li, G. *Nature Photon.* **2009**, *3*, 649-653.
- (26) Liang, Y. Y.; Xu, Z.; Xia, J. B.; Tsai, S. T.; Wu, Y.; Li, G.; Ray, C.; Yu, L. P. *Adv. Mater.* **2010**, *22*, E135- E138.
- (27) Campoy-Quiles, M.; Ferenczi, T.; Agostinelli, T.; Etchegoin, P. G.; Kim, Y.; Anthopoulos, T. D.; Stavrinou, P. N.; Bradley, D. D. C.; Nelson, J. *Nat.Mater.* **2008**, *7*, 158-164.
- (28) Chen, D.; Nakahara, A.; Wei, D.; Nordlund, D.; Russell T. P. *Nano Lett.* **2011**, *11*, 561-567.
- (29) Ma, W. L.; Gopinathan, A.; Heeger, A. J. *Adv. Mater.* **2007**, *19*, 3656-3659.
- (30) Thompson, B. C.; Frechet, J. M. J. *Angew. Chem. Int. Ed.* **2008**, *47*, 58-77.

- (31) Kim, Y.; Cook, S.; Tuladhar, S. M.; Choulis, S. A.; Nelson, J.; Durrant, J. R.; Bradley, D. D. C.; Giles, M.; McCulloch, I.; Ha, C. S.; Ree, M. *Nature Mater.* **2006**, *5*, 197-203.
- (32) Treat, N. D.; Brady, M. A.; Smith, G.; Toney, M. F.; Kramer, E. J.; Hawker, C. J.; Chabynyc, M. L. *Adv. Energy Mater.* **2010**, *1*, 82–89.
- (33) Collins, B. A.; Gann, E.; Guignard, L.; He, X.; McNeill, C. R.; Ade, H. *J. Phys. Chem. Lett.* **2010**, *1*, 3160–3166.
- (34) Lee, K. H.; Schwenn, P. E.; Smith, A. R. G.; Cavaye, H.; Shaw, P. E.; James, M.; Krueger, K. B.; Gentle, I. R.; Meredith, P.; Burn, P. L. *Adv. Mater.* **2011**, *23*, 766-770.
- (35) Moon, J. S.; Takacs, C. J.; Sun, Y.; Heeger, A. J., *Nano Lett.* **2011**, *11*, 1036-1039.
- (36) Swaraj, S.; Wang, C.; Yan, H. P.; Watts, B.; Jan, L. N.; McNeill, C. R.; Ade, H. *Nano Lett.* **2010**, *10*, 2863-2869.
- (37) Swaraj, S.; Wang, C.; Araki, T.; Mitchell, G.; Liu, L.; Gaynor, S.; Deshmukh, B.; Yan, H.; McNeill, C. R.; Ade, H. *Eur. Phys. J. Special Topics.* **2009**, *167*, 121-126.
- (38) Yan, H. P.; Swaraj, S.; Wang, C.; Hwang, I.; Greenham, N. C.; Groves, C.; Ade, H.; McNeill, C. R. *Adv. Funct. Mater.* **2010**, *20*, 4329-4337.
- (39) Wang, C.; Garcia, A.; Yan, H. P.; Sohn, K. E.; Hexemer, A.; Nguyen, T. Q.; Bazan, G. C.; Kramer, E. J.; Ade, H. *J. AM. CHEM. SOC.* **2009**, *131*, 12538-12539.
- (40) Ade, H.; Wang, C.; Garcia, A.; Yan, H.; Sohn, K. E.; Hexemer, A.; Bazan, G. C.; Nguyen, T. Q.; Kramer, E. J. *J. Polym. Sci., Part B: Polym. Phys.* **2009**, *47*, 1291-1299.
- (41) Wang, C.; Araki, T.; Watts, B.; Harton, S.; Koga, T.; Basu, S.; Ade, H. *J. Vac. Sci. Technol., A.* **2007**, *25*, 575-586.
- (42) Wang, C.; Araki, T.; Ade, H. *Appl. Phys. Lett.* **2005**, *87*, 214109.
- (43) Erb, T.; Zhokhavets, U.; Gobsch, G.; Raleva, S.; Stuhn, B.; Schilinsky, P.; Waldauf, C.; Brabec, C. J. *Adv. Funct. Mater.* **2005**, *15*, 1193-1196.
- (44) Chiu, M. Y.; Jeng, U. S.; Su, C. H.; Liang, K. S.; Wei, K. H. *Adv. Mater.* **2008**, *20*, 2573-2578.
- (45) Parnell, A. J.; Dunbar, A. D. F.; Pearson, A. J.; Staniec, P. A.; Dennison, A. J. C.; Hamamatsu, H.; Skoda, M. W. A.; Lidzey, D. G.; Jones, R. A. L. *Adv. Mater.* **2010**, *22*, 2444-2447.

(46) Kiel, J. W.; Kirby, B. J.; Majkrzak, C. F.; Maranville, B. B.; Mackay, M. E. *Soft Matter* **2010**, *6*, 641-646.

(47) White, M. S.; Olson, D. C.; Shaheen, S. E.; Kopidakis, N.; Ginley, D. S. *Appl. Phys. Lett.* **2006**, *89*, 143517.

CHAPTER 4

P3HT NANOPILLARS AND SAWTOOTHED SURFACES FOR ORGANIC PHOTOVOLTAIC DEVICES NANOIMPRINTED BY AAO MEMBRANES AND SAPPHIRE TEMPLATES

4.1 Introduction

During the past decade, organic photovoltaics (OPVs), based on conjugated polymers, have become particularly attractive due to their ease of processing, mechanical flexibility, and low cost for fabricating large area devices.^{1, 2} In OPVs the dissociated free charges (electrons and holes) are created at the interface between the donor (e-donor) and acceptor (e-acceptor) phases, then transported to their respective electrodes, and form the external circuit. Therefore, increasing the interfacial area between the e-donor and e-acceptor phases, and limiting the morphology of the heterojunction to the nanoscale are critical for improving the device performance, since the excitation diffusion length in the conjugated polymer is limited to ~ 10 nm.³⁻⁵ In the last decade, significant progress has been made in OPV research with the introduction of bulk heterojunction (BHJ) systems. In the BHJ system the heterojunction area is increased and, if the domain sizes can be maintained on the tens of nanometer size scale, there would be a substantial increase in the interfacial area and the domain sizes would be commensurate with the exciton diffusion length. Although significant progress has been made in the last decade, the efficiency of converting solar energy into

electrical power with plastic solar cells is still not high enough; the most efficient devices have efficiencies of 8.3% by Konarka Technologies, Inc..

Control over the size scale of the morphology in the active layer can be achieved by thermal annealing⁶⁻⁹, solvent annealing¹⁰⁻¹², controlling solution concentration^{13, 14} and composition, adding additives¹⁵⁻¹⁹, electrospinning²⁰, and nanoimprint lithography²¹⁻²⁵.

Four different OPV devices have been proposed previously. These are: (1) single-layer PV cell; (2) bilayer PV cell; (3) disordered bulk heterojunction (the most popular one); (4) ordered bulk heterojunction.²⁶ An “ordered bulk heterojunction”, consisting of vertically aligned conjugated polymer nanorods surrounded by the e-acceptor materials to form the ordered bicontinuous heterojunction morphology, has been proposed as the ideal morphology for the active layer.^{27, 28}

Several groups have used nanoimprint lithography (NIL) to produce the polymer nanostructures by using a Si mold^{22, 24, 25}. While making the Si mold with nanometer pore size is expensive, anodic aluminum oxide (AAO) membranes, widely used as templates for fabrication of polymer-based nanostructures, including nanotubes,^{29, 30} nanorods,³¹⁻³⁴ mesoporous nanostructures,^{35, 36} and vesicles,³⁷ provide an inexpensive and effective platform. AAO membranes characteristically have a well-defined pore sizes (ranging from 8-500 nm diameter, depending on the anodization conditions) with a narrow pore size distribution, arranged in a hexagonal manner.³⁸ The surface properties can also be tuned by chemically modifying the surface, taking advantage of hydroxyl groups on the surface of the walls.³⁹ AAO template have been used to fabricate poly(3-hexylthiophene) (P3HT) nanopillars^{23, 40}, but the template removal process will dissolve the PEDOT:PSS layer, leave impurities on the active layer, and in addition to these, the

base or acidic solution used to remove the template will deleteriously affect the device performance.

To solve these problems, we present a simple, cost-effective method to fabricate P3HT nanostructures by using the template method. Free-standing nanorod arrays and sawtooth patterns of P3HT were fabricated on ITO/glass substrates by using AAO membranes and mis-cut sapphire crystals as templates, respectively. Two methods were applied: (1) P3HT was forced into the nanopores of the AAO template by thermal imprinting, then the template was dissolved by treatment of a 5 wt% NaOH/H₂O solution to release the P3HT nanoarrays, then freeze-drying was applied to sublime the ice under high vacuum conditions in order to obtain the free-standing P3HT nanoarrays without collapse; (2) AAO templates and sapphire patterns were modified by silicone to reduce the surface energy of the templates and, after thermal imprinting, the templates were removed easily and the nanorods/nanosawtooth patterns were successfully replicated on the P3HT thin film, which were then used to fabricate the OPV devices.

4.2 Experimental

4.2.1 Materials and Methods

Regioregular poly(3-hexylthiophene) ($M_w = 42.4$ k, $M_n = 21.2$ k, RR = 96.8%) and [6,6]-phenyl-C61-butyric acid methyl ester were obtained from Konarka Technologies. DMS-T22 was purchased from Gelest, Inc. The indium tin oxide (ITO)-coated glass substrates (20 ± 5 ohms/sq) were bought from Thin Film Devices Inc..

4.2.2 The Preparation of Anodic Aluminum Oxide (AAO) Membranes

The AAO templates were prepared, according to published methods³⁸, by the two-step anodization process developed by Masuda *et al.* At first, a high-purity aluminum sheet (99.999%, 0.25 mm thick) was polished by the grinder “PowerPro 3000”. Then the sample was sonicated in water and rinsed in an acetone solution. Subsequently, the aluminum sheet was anodized at 40 V in 0.3 mol/L oxalic acid at 17 °C for 5 h. After the resultant aluminum oxide film was chemically etched in a mixture of phosphoric and chromic acid, the second anodization was performed for different time intervals ranging from 60 s to 120 s, which can control the pore length in the AAO templates. Pore widening was performed using aqueous phosphoric acid (5 wt %) at 25 °C for a defined time. The nanopore center-to-center distance is ~110 nm and the diameter is around 60 nm after the pore-widening process by using phosphoric acid. Smaller pore sizes (~30 nm) can be made by performing the anodization at 25 V in 0.3 mol/L sulfuric solution at 4 °C.

4.2.3 The Surface Modification of the Anodic Aluminum Oxide (AAO) Membranes

AAO and sapphire templates were immersed in DMS-T22 at 150 °C for 2 days, subsequently rinsed with toluene, acetone, ethanol and DI water. Finally the substrates were dried.

4.2.4 Contact Angle Measurements

Contact angle measurements were performed using a tensiometer (OCA 20, Future Digital Scientific Co., Garden City NY) and a syringe with a 24-gauge flat-tipped

needle. Dynamic advancing (θ_A) and receding angles (θ_R) were recorded while Milli-Q water was added to and withdrawn from the drop, respectively.

4.2.5 Fabrication of P3HT Nanoarrays

A 2 wt% P3HT chlorobenzene solution was spin-coated on silicon wafers or ITO glass substrates which have been treated with O₂-plasma, at 4000 rpm for 1 min. At the same time, a 2 wt% P3HT solution in chlorobenzene was spin coated onto the AAO templates with an underlying aluminum substrate at 1000 rpm for 1 min, and dried under vacuum at room temperature. Then, both substrates coated with P3HT (one from the AAO template and the other from the silicon wafer or ITO glass substrates) were put facing each other in order to allow the P3HTs layers to interdiffuse, forming a single layer. Then, the sample was sandwiched between two glass slides and clamped together. To get better contact between the AAO template and the silicon or ITO substrate, a 5 mm thick PDMS was inserted between the AAO template and the outside glass slide. Under vacuum conditions, the sample was heated up to 230 °C and annealed for 10 min at that temperature. After the sample was cooled to the room temperature, the top alumina layer was carefully removed by sand paper, and then the sample was immersed in 5 wt% CuCl₂/H₂O solution for about 20 min to completely dissolve the Al layer. Subsequently, the alumina template was removed using a 5 wt% NaOH/H₂O solution to release the P3HT nanoarrays. The substrate with P3HT nanoarrays was immersed in water (10 mins), EtOH/H₂O (1:1) (20 mins) and isopropanol (IPA)/H₂O (1:1) (20 mins) to remove the residue of sodium and aluminum hydroxide. Finally, the sample was transferred to a 20 mL vial filled with 1 mL IPA/H₂O (1:1), and frozen by liquid N₂.

The IPA and water was removed by subliming the ice under high vacuum conditions. IPA was used to make the P3HT nanorods stand normal to the surface due to their low surface energy and low volume expansion when it was frozen.

A 2 wt% P3HT solution in chlorobenzene was spin-coated on PEDOT: PSS coated silicon wafers or ITO glass substrates at 1000 rpm for 1 min. Then the silicone modified AAO membrane with the underlying aluminum substrates or sapphire templates were brought together with the P3HT coated substrates, sandwiched facing each other between two glass slides and clamped together. To get better contact between AAO template and the P3HT coated silicon or ITO substrate, a 5 mm thick PDMS was inserted between the AAO template and the outside glass slide. The sample was heated to 230 °C under vacuum and annealed for 5 mins at that temperature. After the sample cooled down to room temperature, the templates were easily demolded, leaving the nanostructure behind on the P3TH thin film.

4.2.6 Organic Solar Cell Devices Fabrication and Testing

ITO coated glass substrates were cleaned through ultrasonication treatment in detergent, DI water, acetone, and isopropyl alcohol and then dried in an oven overnight. PEDOT: PSS (CLEVIOSTM P VP Al 4083) (~ 35 nm) was spin-coated onto ultraviolet ozone-treated ITO substrates. After annealing at 150 °C for 30 min in air, the substrates were transferred to a glove box. P3HT thin films were spin coated onto the substrates where the thickness of the P3HT film was ~ 180 nm (KLA-TENCOR Alpha-Step IQ Surface Profiler). Nanostructured P3HT surfaces were prepared by the NIL method described above. The PCBM layer was spin-coated directly on top of the P3HT

nanostructured layer from a dichloromethane solution (10 mg/ml). This process was conducted as rapidly as possible to minimize interfacial mixing. Afterwards, a thin (~100 nm) layer of aluminum was thermally evaporated under high vacuum (2×10^{-4} Pa) onto the surface (area 6 mm^2) as the cathode. The preparation procedure is shown in the Scheme 4.1. All current-voltage (I-V) characteristics of the devices were measured under simulated AM1.5G irradiation (100 mW cm^{-2}) using a Xe lamp-based Newport 91160 300-W Solar Simulator as the white light source. The light intensity was adjusted with an NREL-calibrated Si solar cell with a KG-5 filter.

4.2.7 Scanning Electron Microscopy (SEM)

The FEI Magellan 400 Field Emission Scanning Electron Microscope was used to investigate the polymer nanostructures. All samples were coated with 3 nm Au before performing SEM measurements.

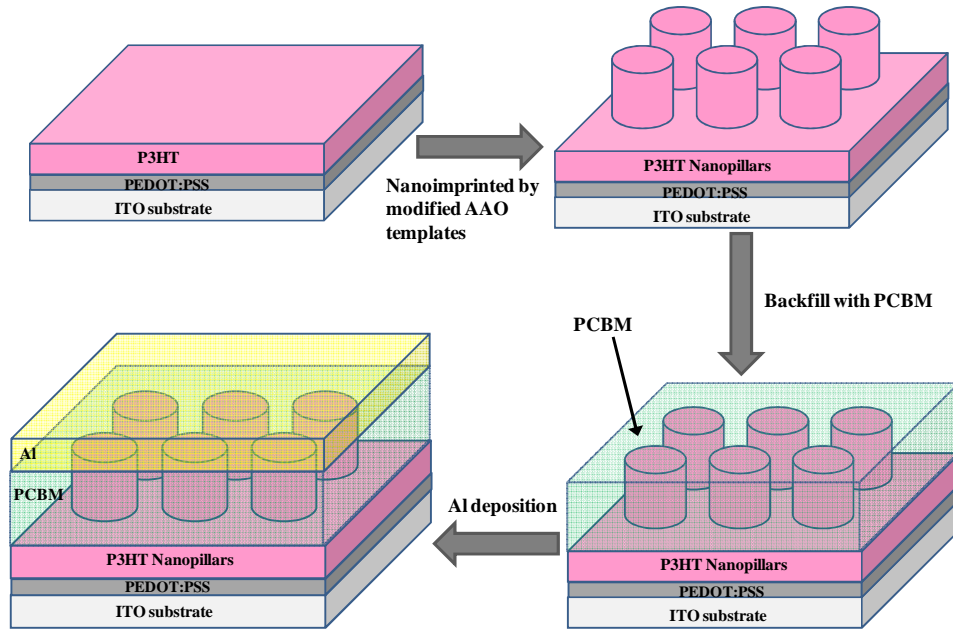
4.2.8 Transmission Electron Microscopy (TEM)

Bright field transmission electron microscopy (TEM) studies were conducted with a JEOL 2000 FX TEM operating at an accelerating voltage of 200 kV.

4.2.9 Grazing Incidence X-ray Diffraction (GIXD)

GIXD measurements were performed on Beamline 7.3.3 at the Advanced Light Source at the Lawrence Berkeley National Laboratory. The experimental set-up and sample cell were designed for surface studies on thin films. An X-ray beam impinged onto the sample at a grazing angle above the critical angle of the polymer film ($\alpha_c =$

0.16) but below the critical angle of the silicon substrate ($\alpha_c = 0.22$). The wavelength of X-rays used was 1.240 \AA , and the scattered intensity was detected using a two-dimensional charge-coupled device (CCD) camera with image sizes of 2304×2304 pixels, pixel size is $0.082 \text{ mm} \times 0.082 \text{ mm}$.



Scheme 4.1 The procedure for the nanostructured organic photovoltaic device.

4.3 Results and Discussion

4.3.1 Preparation and Characterization of the Anodic Aluminum Oxide (AAO) Membranes

Membranes

To be used as NIL templates, a flat, clean surface of the AAO membrane is necessary. To achieve this, the original aluminum sheet was polished to a smooth finish. Here, a mechanical polishing method was used instead of the electropolishing method. The surfaces of the aluminum sheet before and after being polished with the grinder are shown in the Fig 4.1a and Fig 4.1b, respectively. The mirror-like flat surface shown in Fig 4.1b is critical for preparing a flat AAO template. After polishing, the AAO

templates were produced by the traditional two-step anodization process in 0.3 M oxalic acid solution with the second anodization for 1 min, and characterized by SFM and SEM shown Figure 4.1c and Figure 4.1d. Pore sizes ~ 50 nm in diameter are shown which could be easily controlled by the anodization conditions, for example the electrolyte type, concentration, applied voltage and temperature. A side view of the AAO membrane (~ 200 nm in length) is shown in the inset of Figure 4.1d. The pore length could be adjusted by varying the second anodization time, as shown in the Figure 4.2.

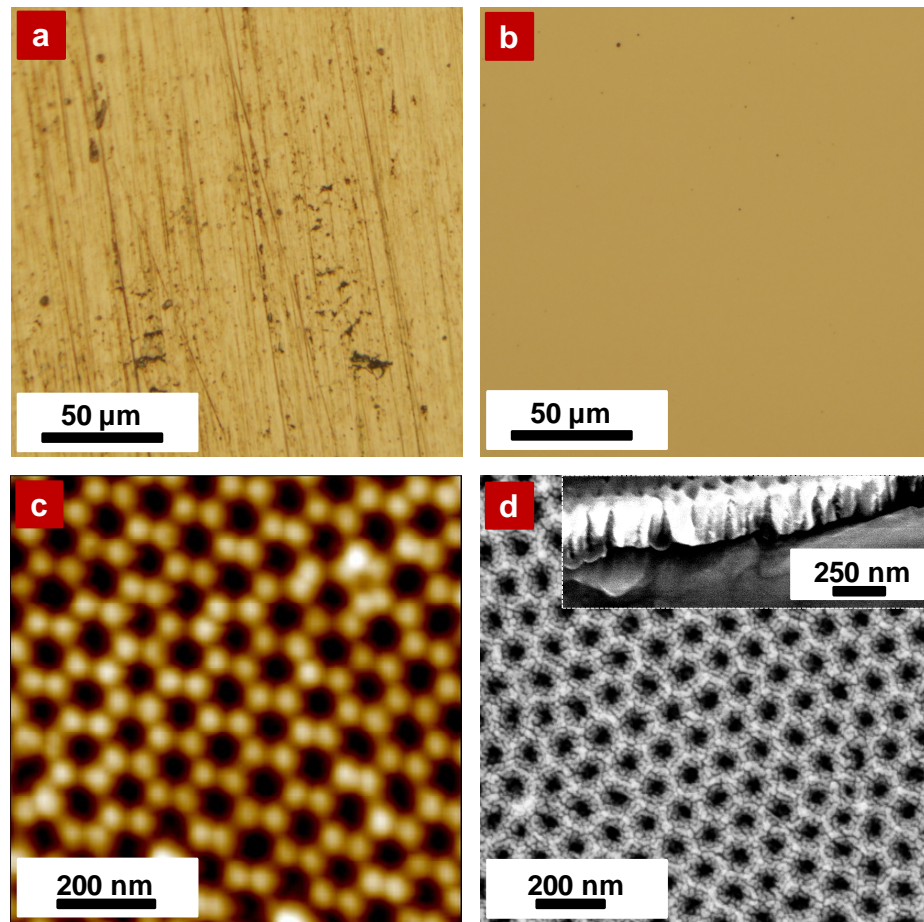


Figure 4.1 Al sheet and AAO membrane: **a**, Al surface before grinding; **b**, Al surface after grinding; **c**, SFM image of the prepared AAO membrane (2nd anodization time 1 min); **d**, SEM image of the prepared AAO membrane. The inset represent the side view of the AAO membrane.

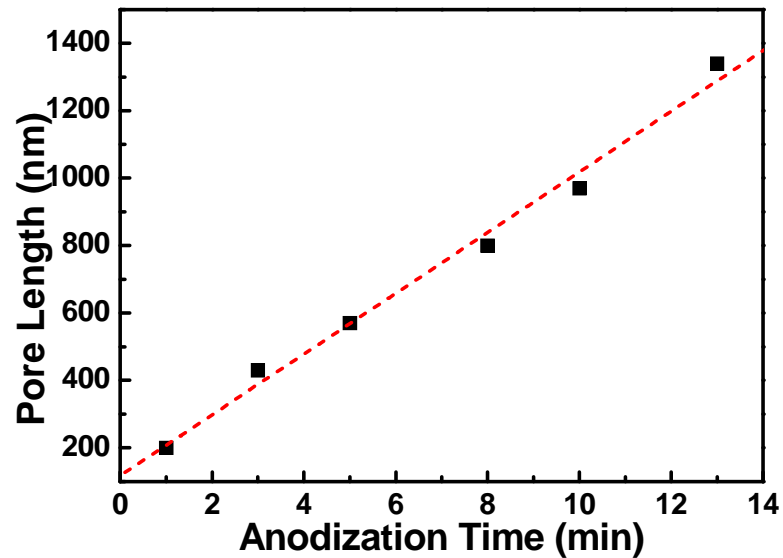


Figure 4.2 Nanopore length growth rate in the AAO template

4.3.2 Surface Modification of the AAO Templates

To understand how the surface properties were changed by the silicone modification, contact angles were measured on the surface before and after the modification was performed (Figure 4.3, Table 4.1). The results show that the surface property of the AAO template is more hydrophobic after being modified by silicone, as discussed by McCarthy and coworkers.⁴¹

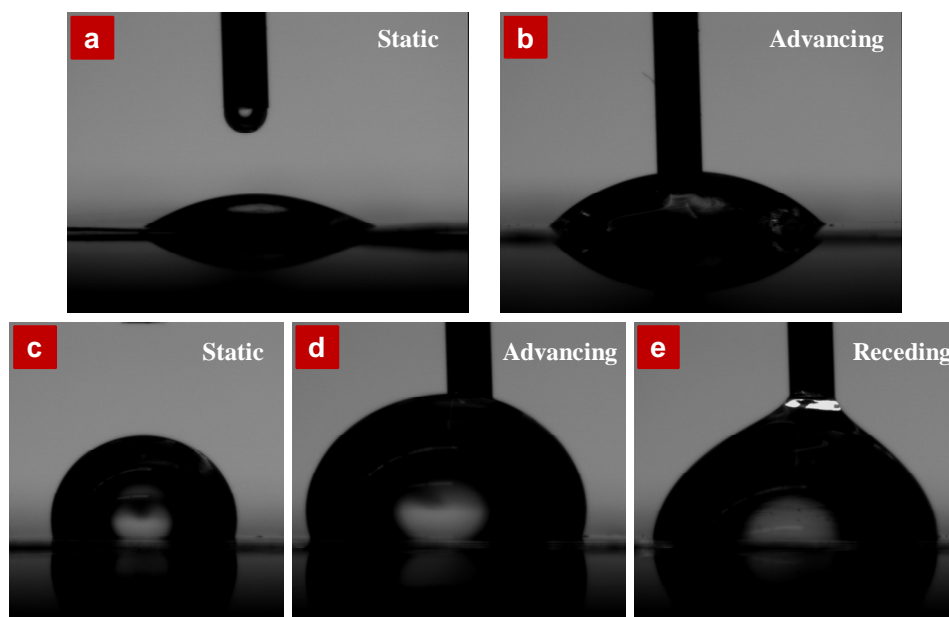


Figure 4.3 Telescopic images of H₂O on AAO membrane surface before and after surface modification: **a**, original AAO membrane (static); **b**, original AAO membrane (advancing); **c**, silicone modified AAO membrane (static); **d**, silicone modified AAO membrane (advancing); **e**, silicone modified AAO membrane (receding).

Table 4.1 Contact angle of the AAO membrane surface before and after surface modification

Contact angle	Original AAO membrane	Silicone modified AAO membrane
Static	33.8°	104.7°
Advancing	43.8°	109.3°
Receding	---	92.9°

4.3.3 Preparation and Characterization of P3HT Nanostructures

To make the nanopillar arrays of P3HT by using the AAO template, we used two different methods. The first method was termed “AAO dissolving method”: P3HT was forced into the nanopores of the AAO template by thermal imprinting and then the template was dissolved with a 5 wt% NaOH/H₂O solution to release the P3HT nanoarrays. Freeze-drying was used to sublime the ice under high vacuum conditions to obtain the free-standing P3HT nanoarrays. This process avoided collapse of the nanopillars by capillary force, if the water was simply evaporated. The second method is NIL: Here, AAO templates were modified with a silicone to reduce the surface energy of the templates. After thermal imprinting, the templates were easily lifted off, leaving P3HT replicas that have potential application in OPV devices. Although the nanostructures obtained by the two methods are similar, their surface properties are markedly different, as shown in Figure 4.4. The AAO dissolving method left a substantial amount of impurity on the surface and the NaOH/H₂O degrades the P3HT, which is not good for the device performance (Figure 4.4a). The NIL method, on the other hand, gave a flat and clean surface (Figure 4.4b), which is good for the device. Therefore, in the following, all the data were obtained using nanopillars produced by the NIL route.

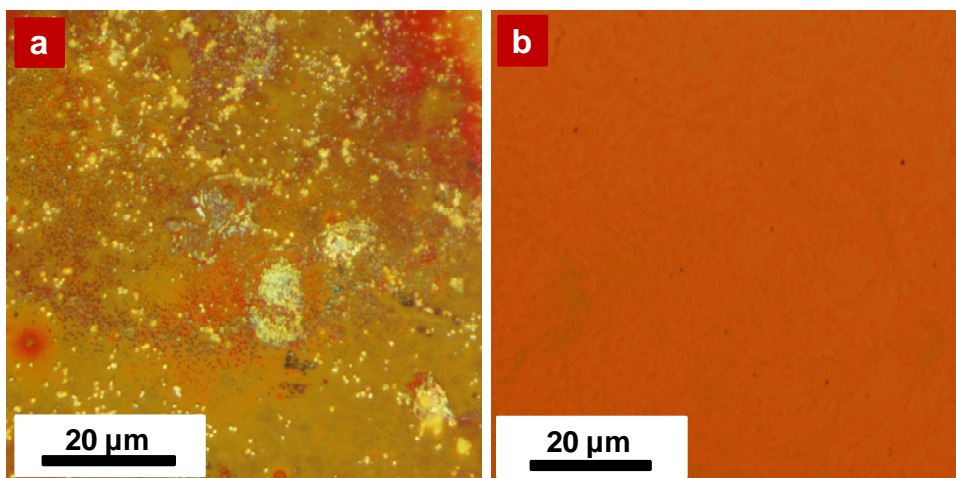


Figure 4.4 Optical microscope images of the surface of the arrays of P3HT nanopillars: **a**, the surface by AAO dissolving method; **b**, the surface by NIL.

Arrays of high areal density, free-standing P3HT nanorods with ~ 50 nm diameter are shown in Figure 4.5a, 5b, 5c. These nanorods afford a high interfacial area between the P3HT and electron acceptor (eg. PCBM) that is back-filled between the nanorods. No collapse of the nanostructures was observed. Using the same surface modification method, the surface energy of sapphire was dramatically reduced, and the advancing contact angle is 110° . In this way the sapphire template with saw-tooth patterned surface could also be used as a mold for P3HT film (Figure 4.5d), which could reduce light reflection, extend the optical length path length and increase the interfacial area between the donor and acceptor phase.

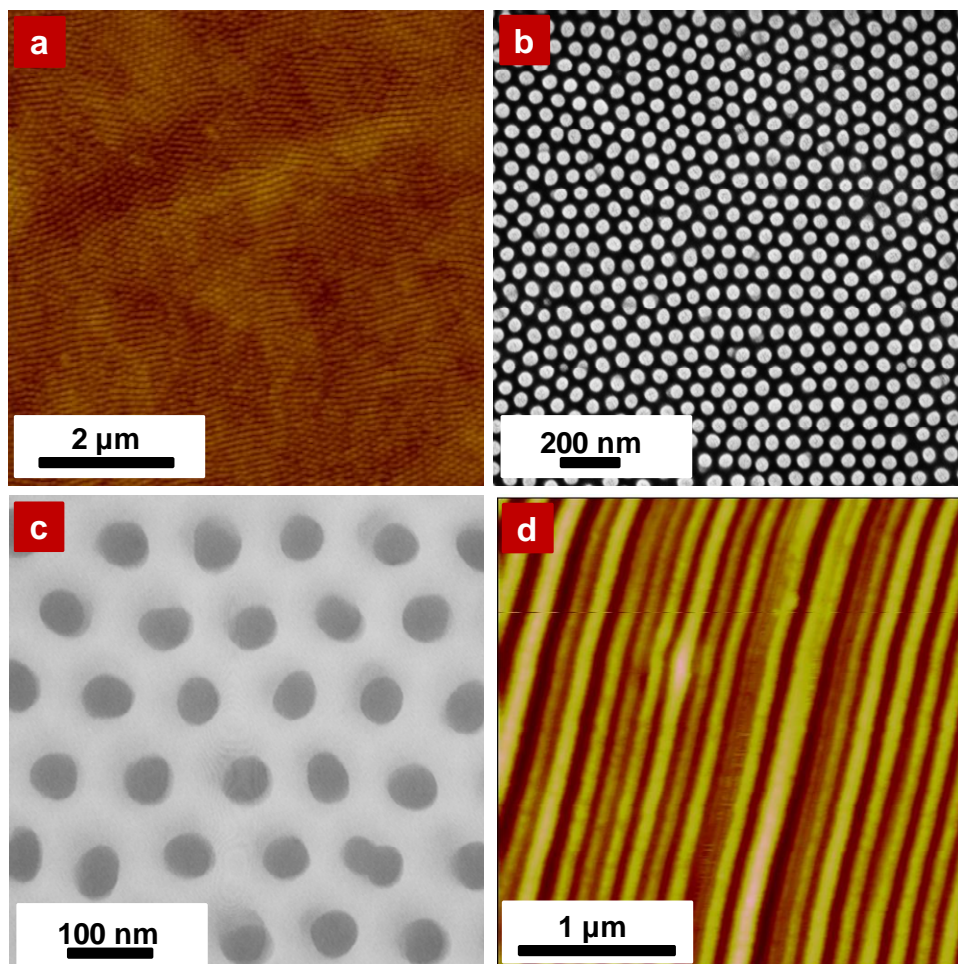


Figure 4.5 Micrographs of free-standing P3HT nanostructures: **a**, SFM of the free-standing P3HT pillars ($D = 50$ nm); **b**, SEM of the free-standing P3HT pillars; **c**, TEM of the free-standing P3HT pillars; **d**, SFM of the P3HT film with the saw tooth pattern.

The diameter of the free standing P3HT nanorods could be easily controlled by the AAO templates, e.g. smaller diameter P3HT nanorods are shown in Figure 4.6.

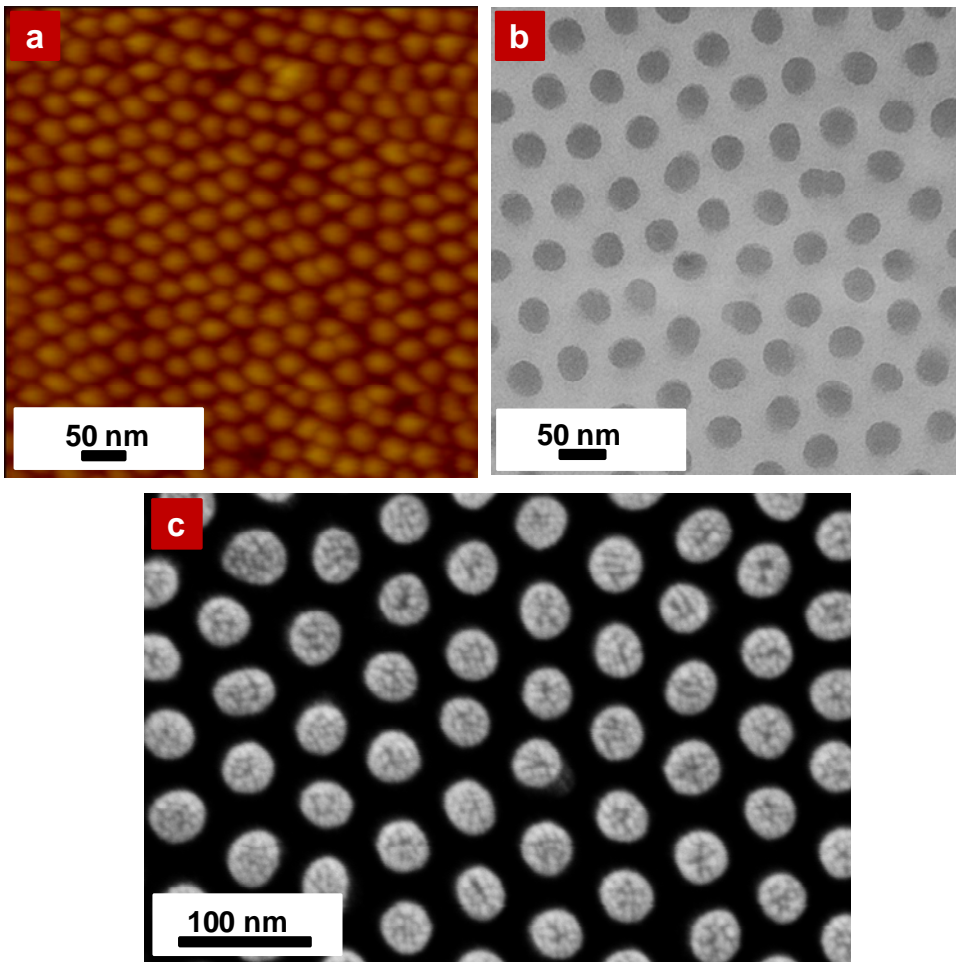


Figure 4.6 Micrographs of free-standing P3HT nanopillars: **a**, SFM of the free-standing P3HT pillars ($D = 30$ nm); **b**, TEM of the free-standing P3HT pillars; **c**, SEM of the free-standing P3HT pillars.

If P3HT:PCBM (1:1 wt ratio) blends were used instead of pure P3HT, free-standing P3HT:PCBM nanopillars could also be fabricated (Figure 4.7). When the Al cathode was thermally evaporated onto the sample, the interface between the active layer and the cathode could be significantly increased.

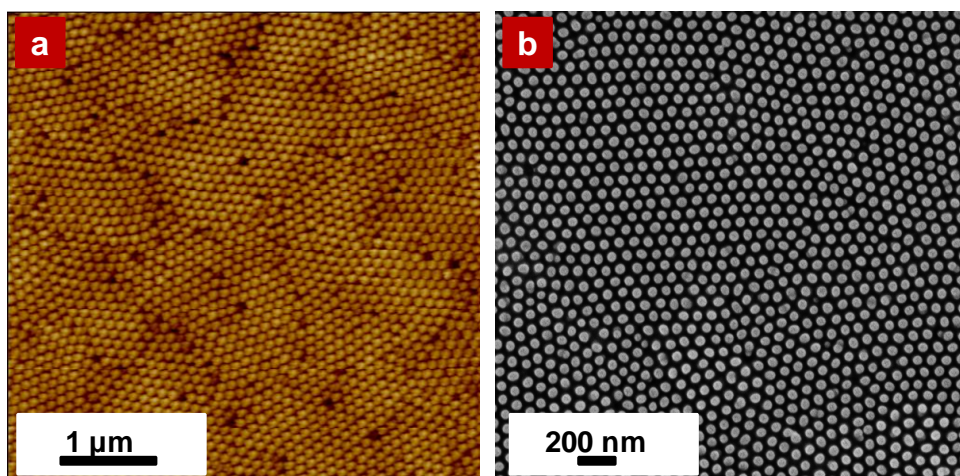


Figure 4.7 Micrographs of free-standing P3HT:PCBM nanopillars: **a**, SFM of the free-standing P3HT:PCBM pillars ($D = 50$ nm); **b**, SEM of the free-standing P3HT:PCBM pillars.

GIXD, shown in Fig. 4.8, was used to determine the ordering of the components in the nanostructures. An incidence angle of 0.18° , which is above the critical angle of the P3HT (0.16°), was used to probe the ordering of the P3HT and/or PCBM throughout sample. The diffraction data are shown in Figure 4.8. Figure 4.8a shows the 2D image for the pure P3HT arrays with nanopillars ~ 50 nm in diameter, while the 2D image in Figure 4.8b is for the P3HT:PCBM blend arrays with nanopillars ~ 50 nm in diameter. Both images show the (100) reflection, along with second (200) and third order (300) reflections, indicating that the edge-on crystal structure is prevalent in these samples. In the P3HT:PCBM blend arrays, an interference arising from the PCBM ($q = 1.41 \text{ \AA}^{-1}$) is observed. The 1-D profile in Figure 4.8c is the signal from out-of-plane scattering, i.e. characterizing the ordering normal to the sample surface.

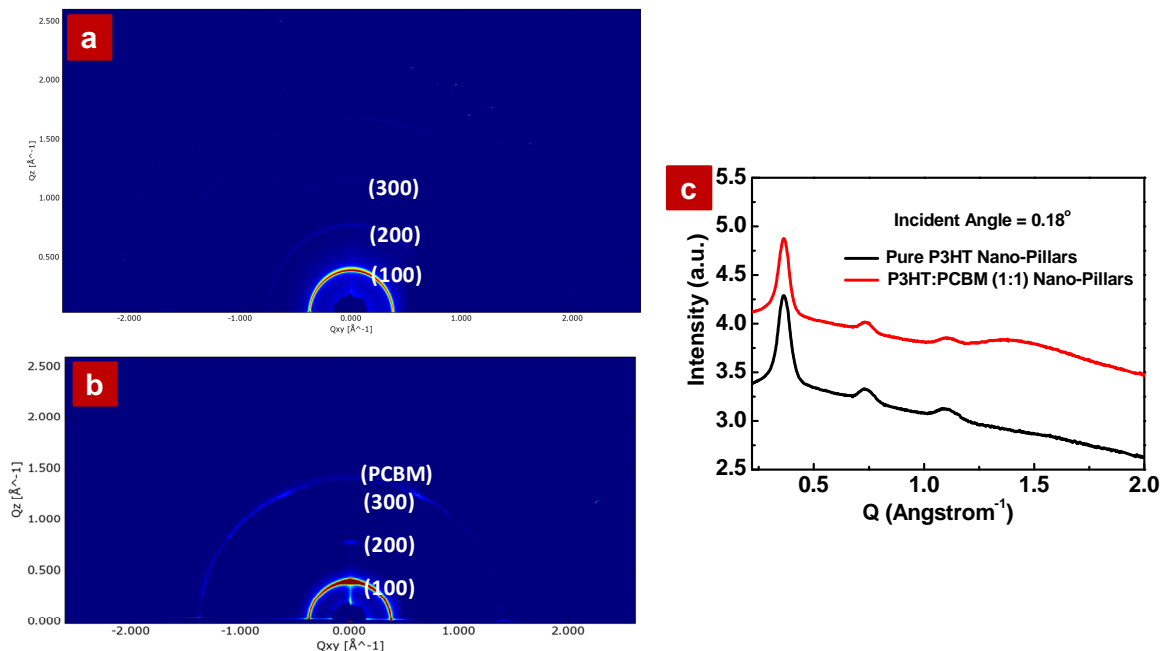


Figure 4.8 GIXD of the free-standing nanopillars: **a**, GIXD 2D image for the pure P3HT arrays ($D = \sim 50$ nm); **b**, GIXD 2D image for the P3HT:PCBM (1:1) arrays ($D = \sim 50$ nm); **c**, The out-of-plane 1-D profile of **a** and **b**.

4.3.4 Device Preparation and Testing

Photovoltaic devices with traditional structures were prepared. Here, a PEDOT:PSS layer was cast onto ITO glass, then a ~ 180 nm P3HT layer was spin-coated from the P3HT chlorobenzene solution on top onto the ITO glass and the NIL process was used to generate a surface topography of the P3HT nanopillars with different diameters. As rapidly as possible, a PCBM solution in dichloromethane was spin-coated onto the P3HT thin film layer or the arrays of P3HT to form a PCBM layer. Al was then evaporated onto the surface as the cathode. The device performances are summarized in Figure 4.9 and Table 4.2. It is clear that the bilayer device shows the lowest performance, as would be expected, characterized by a relatively small V_{oc} and J_{sc} . Once the P3HT layer was converted into nanopillars with ~ 50 nm in diameter and then

covered with PCBM layer, the performance dramatically increased to $\sim 2\%$, with a higher V_{oc} and J_{sc} , due to the larger surface area between the donor and acceptor domains, and the vertically ordered heterojunction morphology in the active layer. When the diameters of the P3HT pillars are reduced to ~ 30 nm, the efficiency is even higher, due, more than likely, to a exciton recombination within the smaller nanopillars, since the excitation diffusion length limitation is ~ 10 nm.

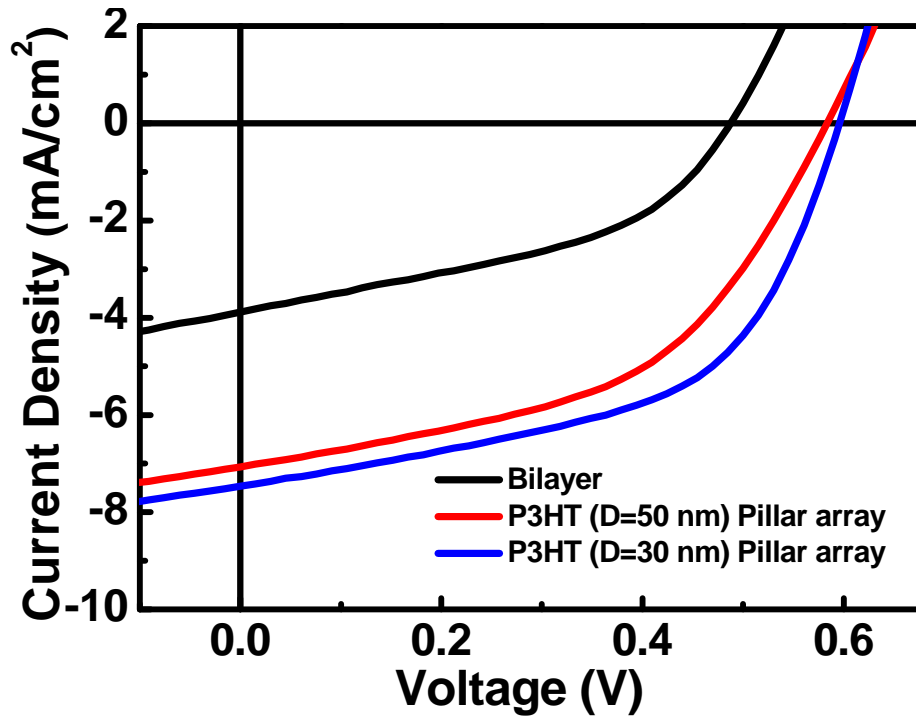


Figure 4.9 J-V curve of the devices based on different textures

Table 4.2 Device performance based on different textures

Device Type	V _{OC} (V)	J _{SC} (mA/cm ²)	FF (%)	PCE (%)
Bilayer	0.49	3.88	43.33	0.82
P3HT Pillars (50 nm)	0.58	7.06	48.83	2.0
P3HT Pillars (50 nm)	0.60	7.46	53.53	2.4

4.4 Conclusion

The surface energy of the AAO template was successfully reduced by silicone modification, making it suitable as an NIL template. Free-standing nanorod arrays and sawtooth patterns of poly(3-hexylthiophene) (P3HT) were fabricated on ITO/glass substrates by using anodic aluminum oxide (AAO) and mis-cut sapphire as the templates. The fabricated P3HT nanostructures dramatically increase the interfacial area between the donor and acceptor, which shorten the transporting pathway of the charge carriers and enhance the device efficiency to around 1.2%. This technique provided new insight and guidance for the development in the photovoltaic area, as it could be easily applied to the NIL and roll-to-roll processing.

4.5 Reference

- (1) Brabec, C. J.; Sariciftci, N. S.; Hummelen, J. C. *Adv. Funct. Mater.* **2001**, 11, 15-26.
- (2) Yu, G.; Gao, J.; Hummelen, J. C.; Wudl, F.; Heeger, A. J. *Science* **1995**, 270, 1789-1791.
- (3) Halls, J. J. M.; Pichler, K.; Friend, R. H.; Moratti, S. C.; Holmes, A. B. *Appl. Phys. Lett.* **1996**, 68, 3120-3122.
- (4) Markov, D. E.; Amsterdam, E.; Blom, P. W. M.; Sieval, A. B.; Hummelen, J. C. *J. Phys. Chem. A* **2005**, 109, 5266-5274.
- (5) Markov, D. E.; Tanase, C.; Blom, P. W. M.; Wildeman, J. *Phys. Rev. B.* **2005**, 72, 045217.
- (6) Hoppe, H.; Sariciftci, N. S. *J. Mater. Chem.* **2006**, 16, 45-61.
- (7) Ma, W. L.; Yang, C. Y.; Gong, X.; Lee, K.; Heeger, A. J. *Adv. Funct. Mater.* **2005**, 15, 1617-1622.
- (8) Chen, D. A.; Nakahara, A.; Wei, D. G.; Nordlund, D.; Russell, T. P. *Nano Lett.* **2011**, 11, 561-567.
- (9) Chen, D.; Liu, F.; Wang, C.; Nakahara, A.; Russell, T. P. *Nano Lett.* **2011**, 11, 2071-2078.
- (10) Zhao, Y.; Xie, Z. Y.; Qu, Y.; Geng, Y. H.; Wang, L. X. *Appl. Phys. Lett.* **2007**, 90, 043504.
- (11) Jo, J.; Na, S. I.; Kim, S. S.; Lee, T. W.; Chung, Y.; Kang, S. J.; Vak, D.; Kim, D. Y. *Adv. Funct. Mater.* **2009**, 19, 2398-2406.
- (12) van Bavel, S. S.; Sourty, E.; de With, G.; Loos, J. *Nano Lett.* **2009**, 9, 507-513.
- (13) Park, S. H.; Roy, A.; Beaupre, S.; Cho, S.; Coates, N.; Moon, J. S.; Moses, D.; Leclerc, M.; Lee, K.; Heeger, A. J. *Nature Photon.* **2009**, 3, 297-302.
- (14) Mayer, A. C.; Toney, M. F.; Scully, S. R.; Rivnay, J.; Brabec, C. J.; Scharber, M.; Koppe, M.; Heeney, M.; McCulloch, I.; McGehee, M. D. *Adv. Funct. Mater.* **2009**, 19, 1173-1179.
- (15) Peet, J.; Kim, J. Y.; Coates, N. E.; Ma, W. L.; Moses, D.; Heeger, A. J.; Bazan, G. C. *Nature Mater.* **2007**, 6, 497-500.

- (16) Chen, H. Y.; Yang, H. C.; Yang, G. W.; Sista, S.; Zadoyan, R. B.; Li, G.; Yang, Y. *J. Phys. Chem. C* **2009**, 113, 7946-7953.
- (17) Moule, A. J.; Meerholz, K. *Adv. Mater.* **2008**, 20, 240-245.
- (18) Lee, J. K.; Ma, W. L.; Brabec, C. J.; Yuen, J.; Moon, J. S.; Kim, J. Y.; Lee, K.; Bazan, G. C.; Heeger, A. J. *J. Am. Chem. Soc.* **2008**, 130, 3619-3623.
- (19) Rogers, J. T.; Schmidt, K.; Toney, M. F.; Kramer, E. J.; Bazan, G. C. *Adv. Mater.* **2011**, 23, 2284-2288.
- (20) Tai, Q. D.; Zhao, X. Z.; Yan, F. *J. Mater. Chem.* **2010**, 20, 7366-7371.
- (21) Haberkorn, N.; Gutmann, J. S.; Theato, P. *ACS Nano* **2009**, 3, 1415-1422.
- (22) Aryal, M.; Buyukserin, F.; Mielczarek, K.; Zhao, X. M.; Gao, J. M.; Zakhidov, A.; Hu, W. C. *J. Vac. Sci. Technol., B* **2008**, 26, 2562-2566.
- (23) Wang, H. S.; Lin, L. H.; Chen, S. Y.; Wang, Y. L.; Wei, K. H. *Nanotechnology* **2009**, 20, 075201.
- (24) He, X. M.; Gao, F.; Tu, G. L.; Hasko, D.; Huttner, S.; Steiner, U.; Greenham, N. C.; Friend, R. H.; Huck, W. T. S. *Nano Lett.* **2010**, 10, 1302-1307.
- (25) He, X. M.; Gao, F.; Tu, G. L.; Hasko, D. G.; Huttner, S.; Greenham, N. C.; Steiner, U.; Friend, R. H.; Huck, W. T. S. *Adv. Funct. Mater.* **2011**, 21, 139-146.
- (26) Coakley, K. M.; McGehee, M. D. *Chem. Mater.* **2004**, 16, 4533-4542.
- (27) Mayer, A. C.; Scully, S. R.; Hardin, B. E.; Rowell, M. W.; McGehee, M. D. *Materials Today* **2007**, 10, 28-33.
- (28) Gunes, S.; Neugebauer, H.; Sariciftci, N. S. *Chem. Rev.* **2007**, 107, 1324-1338.
- (29) Steinhart, M.; Wendorff, J. H.; Greiner, A.; Wehrspohn, R. B.; Nielsch, K.; Schilling, J.; Choi, J.; Gosele, U. *Science* **2002**, 296, 1997-1997.
- (30) Steinhart, M.; Wehrspohn, R. B.; Gosele, U.; Wendorff, J. H. *Angew. Chem. Int. Ed.* **2004**, 43, 1334-1344.
- (31) Moon, S. I.; McCarthy, T. J. *Macromolecules* **2003**, 36, 4253-4255.
- (32) Zhang, M. F.; Dobriyal, P.; Chen, J. T.; Russell, T. P.; Olmo, J.; Merry, A. *Nano Lett.* **2006**, 6, 1075-1079.

- (33) Feng, X. D.; Jin, Z. X. *Macromolecules* **2009**, 42, 569-572.
- (34) Chen, J. T.; Chen, D.; Russell, T. P. *Langmuir* **2009**, 25, 4331-4335.
- (35) Chen, D.; Park, S.; Chen, J. T.; Redston, E.; Russell, T. P. *ACS Nano* **2009**, 3, 2827-2833.
- (36) Wang, Y.; Gosele, U.; Steinhart, M. *Nano Lett.* **2008**, 8, 3548-3553.
- (37) Zhao, W.; Chen, D.; Hu, Y. X.; Grason, G. M.; Russell, T. P. *ACS Nano*. **2011**, 5, 486-492.
- (38) Masuda, H.; Fukuda, K. *Science* **1995**, 268, 1466-1468.
- (39) Chen, J. T.; Shin, K.; Leiston-Belanger, J. M.; Zhang, M. F.; Russell, T. P. *Adv. Funct. Mater.* **2006**, 16, 1476-1480.
- (40) Aryal, M.; Trivedi, K.; Hu, W. C. *ACS Nano* **2009**, 3, 3085-3090.
- (41) McCarthy, T. J. Private communication.

CHAPTER 5

FUTURE DIRECTIONS

5.1 Future Directions

5.1.1 Textured Organic Photovoltaic Devices Based on P3HT/PCBM

This thesis mainly treats the morphology of the photoactive layer of OPVs based on P3HT/PCBM system. The results quantitatively show the photovoltaic device performance is strongly affected by the nanoscopic morphology (*i.e.* a bicontinuous morphology with a characteristic length scale of ~ 10 nm domains.), crystal orientation, and the distribution of components within the photoactive layer.^{1, 2} In addition, we put forth an alternative mechanism, namely a competitive crystallization/diffusion argument, to describe the origin of the morphology.^{1, 2} These findings provide new insights and guidance into the generation of active layers in organic photovoltaics that are crucial in enhancing the device performance.

Although we intensively studied topics related to the morphology of the photoactive layer, to better understand the physics of entire organic photovoltaic device, it is necessary to gain a quantitative understanding of the physics of the device architecture, especially the nanostructures of the active layer, and the interfaces between the active layer and the electrodes.³

Sapphire templates were prepared as described previously⁴, and then were modified with a silicone (T22) to reduce the surface energy of the templates as described in Chapter 4. The surface energy of sapphire was dramatically reduced, the advancing contact angle and the receding angle were 110° and 90° , respectively. By thermal imprinting, as described in Chapter 4 (shown in Figure 5.1a), the templates

were easily lifted off, leaving P3HT or P3HT: PCBM replicas (the saw-tooth pattern) that have potential applications in OPV devices (Figure 5.1b). The saw-tooth pattern could reduce light reflection, extend the optical pathlength, and increase the interfacial area between the active layer and the electrode. Figure 5.1c shows the light reflection in the active layer based on the different surfaces (flat surfaces and textured surfaces). With a flat surface, light is reflected, while on the textured surfaced the reflected light is reduced and which translates into more light being absorbed by the organic active layer, which is can improve the device performance.

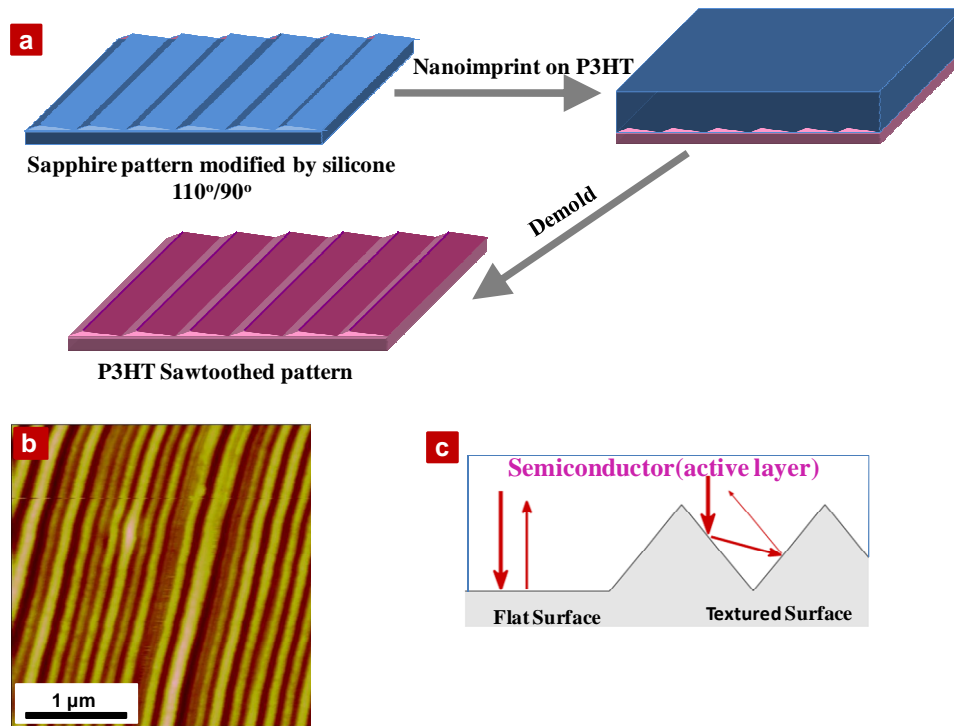


Figure 5.1 P3HT saw-tooth pattern preparation: **a**, scheme of the sawtooth pattern preparation procedure; **b**, SFM height image of P3HT sawtooth pattern; **c**, the light reflection in the active layer based on the different surface (flat surface and textured surface).

Another method, wrinkling, was also developed to texture the interface so as to reduce light reflection and increase the active layer light absorption. The following is our initial results:

Regioregular poly(3-hexylthiophene) ($M_w = 42.4$ k, $M_n = 21.2$ k, RR = 96.8%) and [6,6]-phenyl-C61-butyric acid methylester were obtained from Konarka Technologies. P3HT/PCBM in a 1:1 (w/w) ratio was dissolved in chlorobenzene to make a 20 mg/mL solution. The solution was spin coated onto the PEDOT:PSS coated substrates at 1000 rpm for 1 min. Different thicknesses of Al was thermally evaporated onto the top of the blend film, and the entire assembly was thermally annealed at 150 °C, then cooled back to the RT. Optical microscopy (OM) and scanning force microscopy (SFM), images were taken at different times during the heating process. Figure 5.2 shows the OM images of the samples with Al layers of different thickness. With increasing Al thickness, the wavelength of the P3HT/PCBM surface increased, as given in Table 5.1. The origin of the wrinkle formation was the difference in the thermal expansion coefficients of the active layer and the Al.⁵

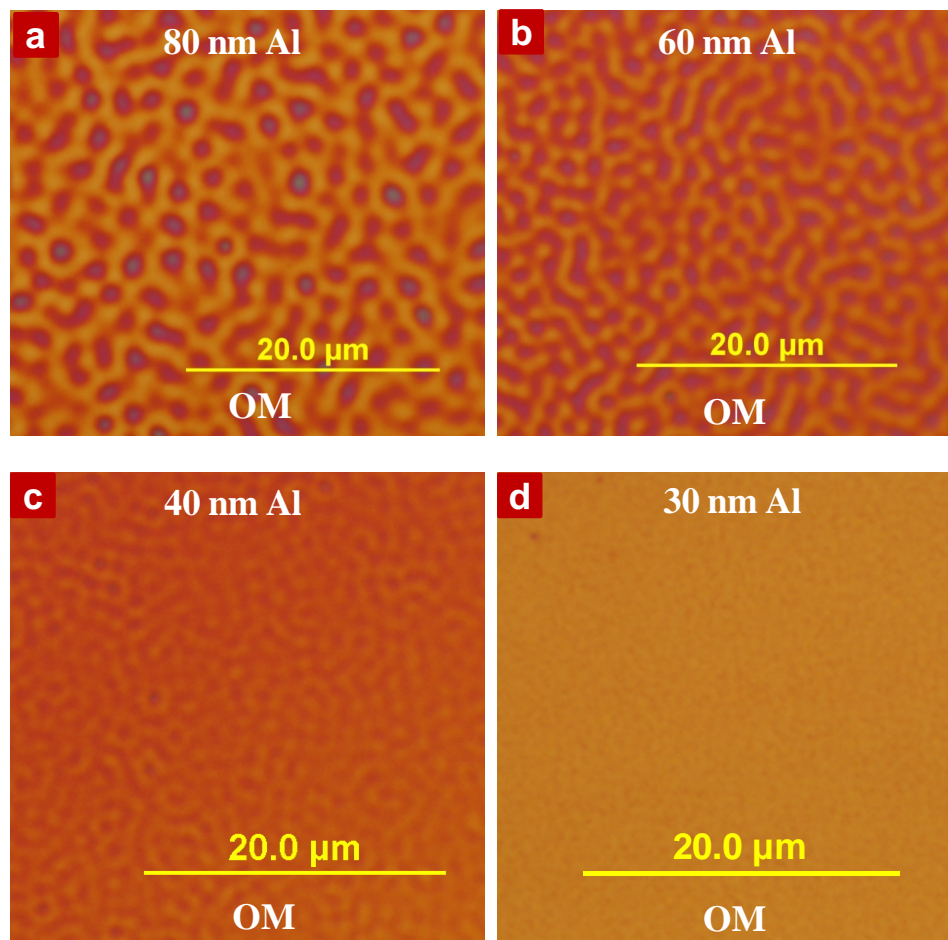


Figure 5.2 OM images (after dissolving Al): **a**, (P3HT/PCBM)/80 nm Al annealed at 150 °C for 30 min; **b**, (P3HT/PCBM)/60 nm Al annealed at 150 °C for 30 min; **c**, (P3HT/PCBM)/40 nm Al annealed at 150 °C for 30 min; (P3HT/PCBM)/30 nm Al annealed at 150 °C for 30 min.

Table 5.1 The wrinkle wavelength of P3HT: PCBM Vs the thickness of Al layer

Thickness of Al Layer	Wavelength of the wrinkles
80 nm	2.66 μm
60 nm	1.86 μm
40 nm	1.17 μm
30 nm	850 nm

Figure 5.3a and 5.3b show SFM images taken when the samples were heated to 150° C for 30 min. Fig. 5.3a shows the sample surface after dissolving the Al layer by using CuCl₂, while the sample surface before dissolving the Al layer is shown in Fig 5.3b. *In-situ* SFM was performed at 150° C and showed that the wrinkling took place immediately. Fig 5.3c shows an *in-situ* 3-D SFM image of (P3HT/PCBM)/60 nm Al annealed at 150° C for 6 min. As can be seen, wrinkles formed on the surface of the film. The wavelengths and amplitudes of the wrinkles are ~ 2.5 μm and 65 nm, respectively. The wrinkles will increase the interfacial area between the active layer and the cathode which is advantageous for electron collection and will also increase the absorption of light, due to the surface texturing. The interfacial area between the active layer and the cathode should be directly related to device performance. The surface texture (saw-toothed pattern or wrinkle pattern) of the active layer should be related to light absorption, which is one of the most important factors affecting the final device performance. These topics are interesting to explore, which maybe provide new insights and guidance into the generation of higher performance OPVs.

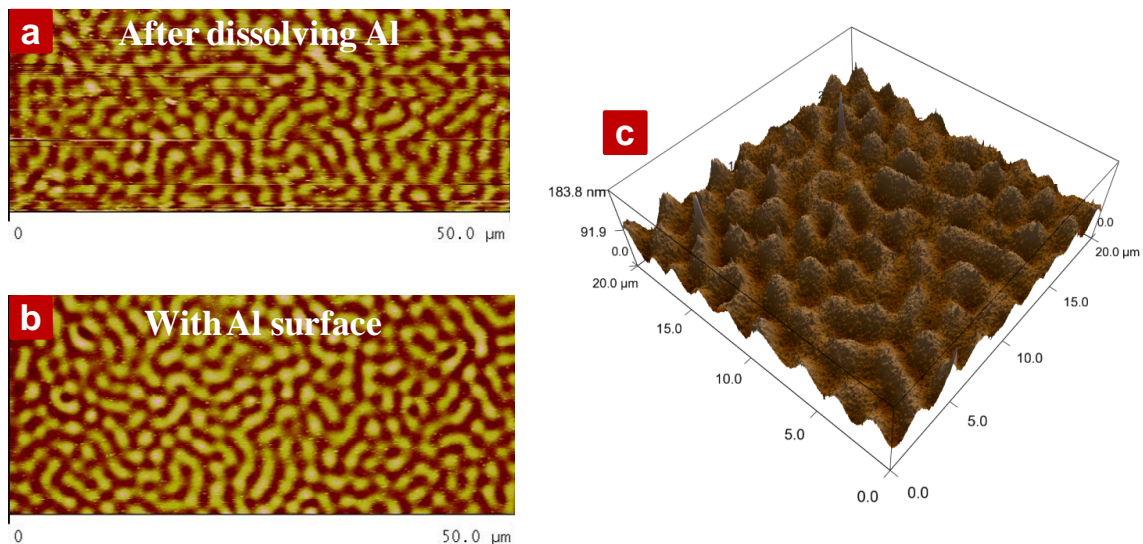


Figure 5.3 SFM height images: **a**, (P3HT/PCBM)/60 nm Al annealed at 150 °C for 30 min (after dissolving Al); **b**, (P3HT/PCBM)/60 nm Al annealed at 150 °C for 30 min (with Al); **c**, In-situ 3-D SFM image of (P3HT/PCBM)/60 nm Al annealed at 150 °C for 6 min (with Al).

5.1.2 Three Component Organic Photovoltaic Devices

All the devices described in this thesis are all based on the P3HT/PCBM system, but it is impossible to achieve a device efficiency with this system, above 10%. Driving the efficiency of bulk heterojunction (BHJ) organic photovoltaic (OPV) solar cells above the 10% barriers is absolutely essential to make these systems an economically viable technology. Achieving this goal requires the synthesis of new materials or developing strategies by which existing materials can be driven past current efficiencies. Controlling the morphology of the active layer, generally consisting of a mixture of a hole-transporting polymer, with an electron-transporting material, is essential in optimizing the morphology for device performance. Only recently have there been strides to understand the fundamental polymer physics governing the morphology and, as such, new routes to enhance efficiencies have been opened. Yet, is it clear that

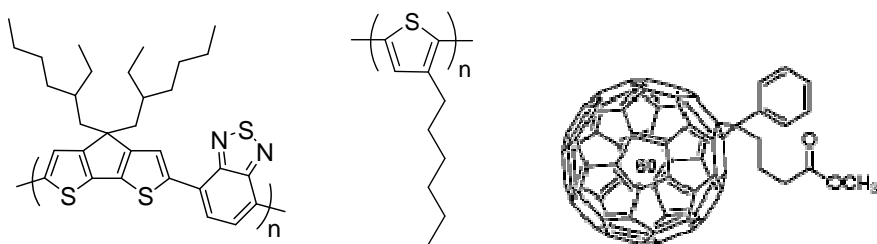
tandem type structures are the most likely route by which efficiencies will be pushed well past this 10% barrier. A tandem device is, essentially, two independent BHJ OPV devices where the absorption of one hole-transporting polymer is at a maximum in a spectral range that complements the other hole-transporting polymer so that a maximal amount of solar energy is absorbed. Overall efficiency of the device is enhanced simply because more photons are absorbed.⁶ Yet, producing tandem devices is a complex, multi-stepped process that will be difficult to realize commercially. Consequently, we have been taking an alternate one-step approach where we are preparing active layers consisting of three components, two hole-transporting polymers active in different wavelength ranges of the solar spectrum with one electron transporting material. It remains, though, a technical and fundamental challenge to design and control the morphology such that the two hole-transporting polymers can act independently.

We will investigate mixtures of two electron donors, one is the well-studied poly(3-hexylthiophene) (P3HT) and the other is a low bandgap material, such as poly[2,6-(4,4-bis(2-ethylhexyl)-4H-cyclopenta[2,1-b;3,4-b']-dithiophene)-alt -4,7-(2,1,3-benzothiadiazole)] (PCPDTBT) (Scheme 5.1). [6, 6]-phenyl C₆₁-butyric acid methyl ester (PCBM) is chosen as the electron acceptor. Then we spinning coat the mixture and make them into a three component random structure as shown in Scheme 5.2. Though this system could cover the wide wavelength ranges of the solar spectrum, the devices based on this system still have the possible problem that the device efficiency will be between the P3HT/PCBM system and PCPDTBT/PCBM system. The possible reason is the total photon absorption in the three components system is not maximized. In order to solve this possible problem and increase the total light

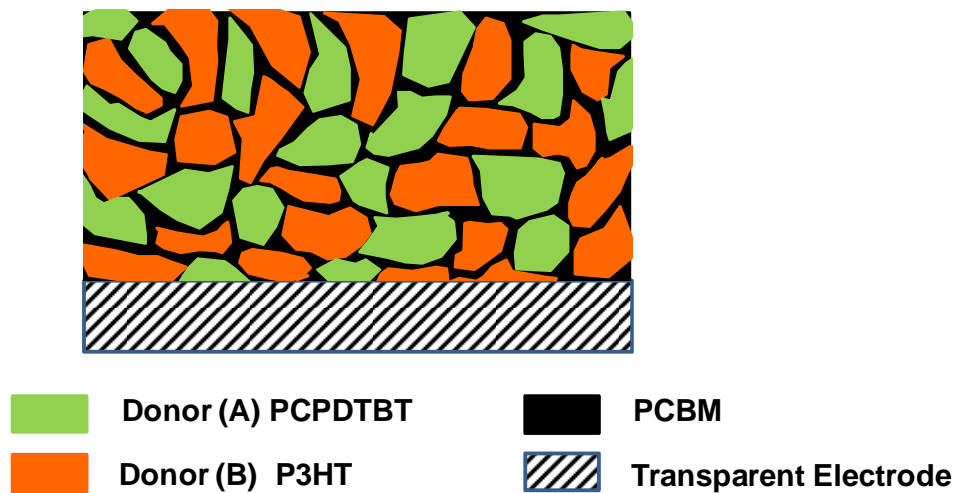
absorption of the active layer, we provide an alternative choice to make a gradient structure, as shown in Scheme 5.3. As we know, if the light shines on the transparent electrode, in order to maximize the photon absorption of the system, the short wavelength absorption layer should be put in front of the longer wavelength absorption layer. How to realize this possible ideal structure?

We can simply spin coat the PCBM on the transparent electrode and then float the P3HT and PCPDTBT layers sequentially. Then, thermal annealing can be used to cause an interdiffusion, generating a gradient structure. The disadvantage of this process is that the use of a floatation step is not commercially viable.

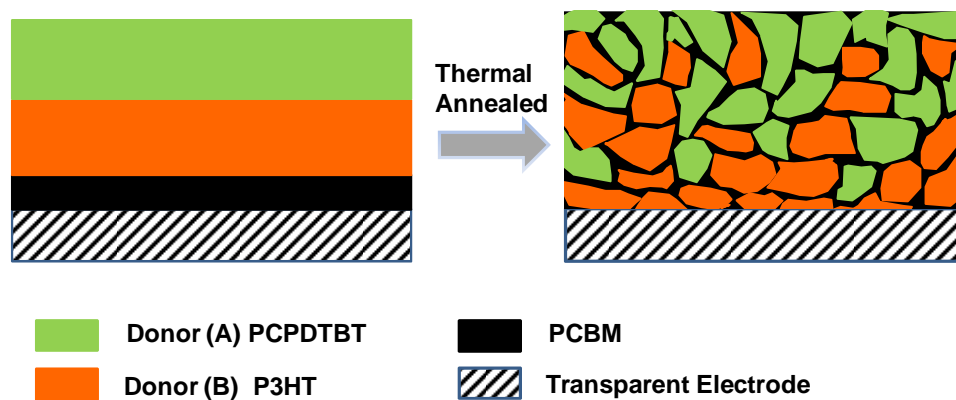
Scheme 5.4 shows an alternative strategy where we use a UV-crosslinkable P3HT (the chemical structure shown at the bottom of the scheme), as described in the literature,⁷ then spin coating a layer of PCPDTBT on top of this, followed by coating a PCBM layer on top of the PCPDTBT layer using a selective solvent. A thermal treatment can then be used cause the diffusion of the PCBM into both layers. The final gradient or bilayer structures are shown in Schemes 5.3 and 5.4, respectively. Either of these structures could, possibly, optimize the device performance.



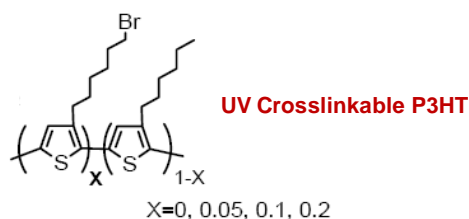
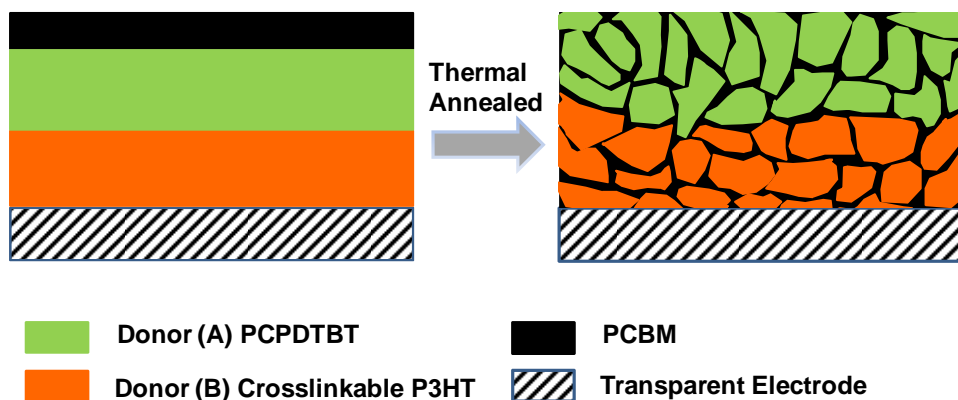
Scheme 5.1 Chemical structure of PCPDTBT, P3HT and PCBM.



Scheme 5.2 Preparation of the random structure from the PCBM/P3HT/PCPDTBT mixture.



Scheme 5.3 Preparation of the gradient structure from the PCBM/P3HT/PCPDTBT trilayer.



Scheme 5.4 Preparation of the bilayer structure from the crosslinked P3HT/PCPDTBT/PCBM trilayer.

To fully understand the possible efficiency improvement, investigation of and developing strategies to control the morphology of these systems are necessary. Resonant soft X-ray scattering (RSoXS) enables one to adjust the contrast by varying the incident x-ray energy to absorption edges characteristic of the chemical bonding of the different components. This, in turn, will enable the variation of the contrast of the different phases formed in the morphology of the active layer and, as such, with RSoXS the spatial correlations in the domains within the active layer can be probed. Based on chemical sensitivity, we can selectively highlight the different components and clarify the morphology of the thin film of the active layers. Due to the similarity of the electron densities of P3HT and PCPDTBT the contrast for hard x-rays is very low, and only limited information can be gleaned on the morphology. RSoXS, however, will be an ideal method to probe the domains of each component independently. PCPDTBT

contains nitrogen, P3HT has lots of sulfur atoms and PCBM is very rich in carbon atoms, the scattering contrast will be significantly enhanced by tuning X-ray energy to the nitrogen or carbon absorption edges.

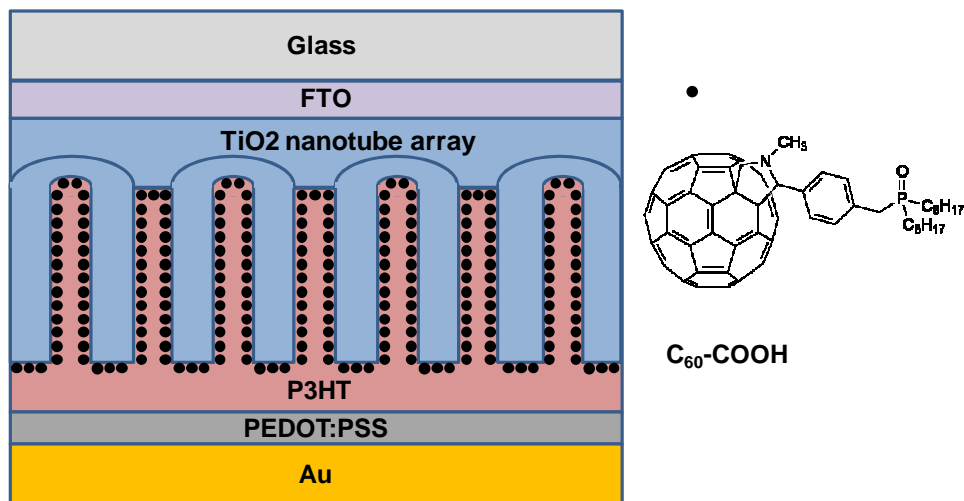
Our previous experiments on P3HT/PCBM thin films have already demonstrated the utility of RSoXS in characterizing the morphology of binary mixtures of a hole-transporting polymer with PCBM, the active layer in BHJ OPVs.² For the three-component systems of interest in future studies, the x-ray energy will be tuned to the absorption edges of the C-N bonding in the PCPDTBT, the C-S bonding in the P3HT, and the enhanced carbon content in the PCBM, so as to vary the contrast of the different components and enable the examination of the spatial correlations of the different components using grazing incidence RSoXS. These studies will provide information on the phase behavior of the ternary mixtures, in- and out-of-the-plane, in thin films that are comparable in thickness to typical active layers. Fully understanding the morphologies of the ternary mixtures is critical for understanding the physics of device based on the ternary mixtures, which we believe is the future of the OPVs with efficiency higher than 10%.

5.1.3 Hybrid Photovoltaic Devices

Another popular solar cell device is the hybrid photovoltaic device as, for example, based on TiO₂ which is a good electron conductor. The TiO₂ nanotube arrays with different lengths and pore sizes will be provided by Mallouk and coworkers.^{8,9} A device structure, like that shown in Scheme 5.5 is one possible strategy.

Before the modified C₆₀ is anchored to the TiO₂ surface, a surface treatment will be necessary. A 2M TiCl₄ is diluted to 0.05 M by the addition of water with constant

stirring, while the solution is cooled in an ice bath. Then the TiO₂ nanotube arrays are then dipped into the 0.05 M TiCl₄ solution for 20 -24 h, and cured at 500 °C for 1 h. Then the sample is immersed in a modified C₆₀ (the structures are shown in Scheme 5.5) solution for 4 hrs, and rinsed with ethanol and dried under vacuum. After this procedure, the modified C₆₀ is anchored to the inner wall of the tubes as a monolayer (Scheme 5.5). UV-Vis and contact angle measurement will be used to confirm whether the C₆₀ is successfully anchored. Then, P3HT is back-filled into the pores, PEDOT: PSS is then coated on top of this before a 50 nm Au layer is evaporated on the surface (Scheme 5.5). The advantage of this structure is that the interfacial area between the P3HT/C₆₀ will be enlarged; the charge transporting length can be shortened; and the electrons in C₆₀ could be immediately transported to TiO₂, then to the FTO electrode. Finally, the devices based on different size TiO₂ nanotube array will be tested and modified.



Scheme 5.5 Schematic of TiO₂ nanotube array assembled with modified C₆₀, and used for photovoltaic application.

5.2 References

- (1) Chen, D. A.; Nakahara, A.; Wei, D. G.; Nordlund, D.; Russell, T. P. *Nano Letters* **2011**, 11, 561-567.
- (2) Chen, D.; Liu, F.; Wang, C.; Nakahara, A.; Russell, T. P. *Nano Letters* **2011**, 11, 2071-2078.
- (3) Simon, J.; Andre, J. J. *Molecular Semiconductors: Photoelectrical Properties and Solar Cells*, Springer, **1985**.
- (4) Park, S.; Lee, D. H.; Xu, J.; Kim, B.; Hong, S. W.; Jeong, U.; Xu, T.; Russell, T. P. *Science* **2009**, 323, 1030-1033.
- (5) Yoo, P. J.; Lee, H. H. *Macromolecules* **2005**, 38, 2820-2831.
- (6) Sista, S.; Hong, Z. R.; Chen, L. M.; Yang, Y. *Energy & Environmental Science* **2011**, 4, 1606-1620.
- (7) Kim, B. J.; Miyamoto, Y.; Ma, B. W.; Frechet, J. M. J. *Advanced Functional Materials* **2009**, 19, (14), 2273-2281.
- (8) Prakasam, H. E.; Shankar, K.; Paulose, M.; Varghese, O. K.; Grimes, C. A. *Journal of Physical Chemistry C* **2007**, 111, 7235-7241.
- (9) Yoriya, S.; Paulose, M.; Varghese, O. K.; Mor, G. K.; Grimes, C. A. *Journal of Physical Chemistry C* **2007**, 111, 13770-13776.

BIBLIOGRAPHY

Ade, H.; Wang, C.; Garcia, A.; Yan, H.; Sohn, K. E.; Hexemer, A.; Bazan, G. C.; Nguyen, T. Q.; Kramer, E. J. *J. Polym. Sci., Part B: Polym. Phys.* **2009**, *47*, 1291-1299.

Aryal, M.; Buyukserin, F.; Mielczarek, K.; Zhao, X. M.; Gao, J. M.; Zakhidov, A.; Hu, W. C. *J. Vac. Sci. Technol., B.* **2008**, *26*, 2562-2566.

Aryal, M.; Trivedi, K.; Hu, W. C. *ACS Nano* **2009**, *3*, 3085-3090.

Audinot, J. N.; Leveque, P.; Bechara, R.; Leclerc, N.; Guillot, J.; Migeon, H. N.; Hadziioannou, G.; Heiser, T. *Surf. Interface Anal.* **2010**, *42*, 1010-1013.

Bjorstrom, C. M.; Nilsson, S.; Bernasik, A.; Budkowski, A.; Andersson, M.; Magnusson, K. O.; Moons, E. *Appl. Surf. Sci.* **2007**, *253*, 3906-3912.

Brabec, C. J.; Sariciftci, N. S.; Hummelen, J. C. *Adv. Funct. Mater.* **2001**, *11*, 15-26.

Brabec, C. J.; Zerza, G.; Cerullo, G.; De Silvestri, S.; Luzzati, S.; Hummelen, J. C.; Sariciftci, S. *Chem. Phys. Lett.* **2001**, *340*, 232-236.

Campoy-Quiles, M.; Ferenczi, T.; Agostinelli, T.; Etchegoin, P. G.; Kim, Y.; Anthopoulos, T. D.; Stavrinou, P. N.; Bradley, D. D. C.; Nelson, J. *Nat. Mater.* **2008**, *7*, 158-164.

Chen, D.; Liu, F.; Wang, C.; Nakahara, A.; Russell, T. P. *Nano Lett.* **2011**, *11*, 2071-2078.

Chen, D.; Nakahara, A.; Wei, D.; Nordlund, D.; Russell T. P. *Nano Lett.* **2011**, *11*, 561-567.

Chen, D.; Park, S.; Chen, J. T.; Redston, E.; Russell, T. P. *ACS Nano* **2009**, *3*, 2827-2833.

Chen, H. Y.; Hou, J. H.; Zhang, S. Q.; Liang, Y. Y.; Yang, G. W.; Yang, Y.; Yu, L. P.; Wu, Y.; Li, G. *Nature Photon.* **2009**, *3*, 649-653.

Chen, H. Y.; Yang, H. C.; Yang, G. W.; Sista, S.; Zadoyan, R. B.; Li, G.; Yang, Y. *J. Phys. Chem. C.* **2009**, *113*, 7946-7953.

Chen, J. T.; Chen, D.; Russell, T. P. *Langmuir* **2009**, *25*, 4331-4335.

Chen, J. T.; Shin, K.; Leiston-Belanger, J. M.; Zhang, M. F.; Russell, T. P. *Adv. Funct. Mater.* **2006**, *16*, 1476-1480.

- Chiu, M. Y.; Jeng, U. S.; Su, C. H.; Liang, K. S.; Wei, K. H. *Adv. Mater.* **2008**, *20*, 2573-2578.
- Coakley, K. M.; McGehee, M. D. *Chem. Mater.* **2004**, *16*, 4533-4542.
- Collins, B. A.; Gann, E.; Guignard, L.; He, X.; McNeill, C. R.; Ade, H. *J. Phys. Chem. Lett.* **2010**, *1*, 3160-3166.
- Dennler, G.; Sariciftci, N. S. *Proceedings of the Ieee* **2005**, *93*, 1429-1439.
- Erb, T.; Zhokhavets, U.; Gobsch, G.; Raleva, S.; Stuhn, B.; Schilinsky, P.; Waldauf, C.; Brabec, C. J. *Adv. Funct. Mater.* **2005**, *15*, 1193-1196.
- Feng, X. D.; Jin, Z. X. *Macromolecules* **2009**, *42*, 569-572.
- Germack, D. S.; Chan, C. K.; Hamadani, B. H.; Richter, L. J.; Fischer, D. A.; Gundlach, D. J.; DeLongchamp, D. M. *Appl. Phys. Lett.* **2009**, *94*, 233303.
- Gregg, B. A. *J. Phys. Chem. B* **2003**, *107*, 4688-4698.
- Gunes, S.; Neugebauer, H.; Sariciftci, N. S. *Chem. Rev.* **2007**, *107*, 1324-1338.
- Haberkorn, N.; Gutmann, J. S.; Theato, P. *ACS Nano* **2009**, *3*, 1415-1422.
- Halls, J. J. M.; Pichler, K.; Friend, R. H.; Moratti, S. C.; Holmes, A. B. *Appl. Phys. Lett.* **1996**, *68*, 3120-3122.
- Halls, J. J. M.; Walsh, C. A.; Greenham, N. C.; Marseglia, E. A.; Friend, R. H.; Moratti, S. C.; Holmes, A. B. *Nature* **1995**, *376*, 498-500.
- Hashimoto, T.; Kumaki, J.; Kawai, H. *Macromolecules* **1983**, *16*, 641-648.
- He, X. M.; Gao, F.; Tu, G. L.; Hasko, D. G.; Huttner, S.; Greenham, N. C.; Steiner, U.; Friend, R. H.; Huck, W. T. S. *Adv. Funct. Mater.* **2011**, *21*, 139-146.
- He, X. M.; Gao, F.; Tu, G. L.; Hasko, D.; Huttner, S.; Steiner, U.; Greenham, N. C.; Friend, R. H.; Huck, W. T. S. *Nano Lett.* **2010**, *10*, 1302-1307.
- Hoffmann, R.; Janiak, C.; Kollmar, C. *Macromolecules* **1991**, *24*, 3725-3746.
- Hoppe, H.; Sariciftci, N. S. *J. Mater. Chem.* **2006**, *16*, 45-61.
- Jo, J.; Na, S. I.; Kim, S. S.; Lee, T. W.; Chung, Y.; Kang, S. J.; Vak, D.; Kim, D. Y. *Adv. Funct. Mater.* **2009**, *19*, 2398-2406.

Joshi, S.; Pingel, P.; Grigorian, S.; Panzner, T.; Pietsch, U.; Neher, D.; Forster, M.; Scherf, U. *Macromolecules* **2009**, *42*, 4651-4660.

Keith, H. D.; Padden, F. J. *J. Appl. Phys.* **1963**, *34*, 2409-2421.

Kiel, J. W.; Kirby, B. J.; Majkrzak, C. F.; Maranville, B. B.; Mackay, M. E. *Soft Matter* **2010**, *6*, 641-646.

Kim, B. J.; Miyamoto, Y.; Ma, B. W.; Frechet, J. M. J. *Advanced Functional Materials* **2009**, *19*, 2273-2281.

Kim, D. H.; Park, Y. D.; Jang, Y. S.; Yang, H. C.; Kim, Y. H.; Han, J. I.; Moon, D. G.; Park, S. J.; Chang, T. Y.; Chang, C. W.; Joo, M. K.; Ryu, C. Y.; Cho, K. W. *Adv. Funct. Mater.* **2005**, *15*, 77-82.

Kim, Y.; Choulis, S. A.; Nelson, J.; Bradley, D. D. C.; Cook, S.; Durrant, J. R. *Appl. Phys. Lett.* **2005**, *86*, 063502.

Kim, Y.; Cook, S.; Tuladhar, S. M.; Choulis, S. A.; Nelson, J.; Durrant, J. R.; Bradley, D. D. C.; Giles, M.; McCulloch, I.; Ha, C. S.; Ree, M. *Nature Mater.* **2006**, *5*, 197-203.

Lee, J. K.; Ma, W. L.; Brabec, C. J.; Yuen, J.; Moon, J. S.; Kim, J. Y.; Lee, K.; Bazan, G. C.; Heeger, A. J. *J. AM. CHEM. SOC.* **2008**, *130*, 3619-3623.

Lee, K. H.; Schwenn, P. E.; Smith, A. R. G.; Cavaye, H.; Shaw, P. E.; James, M.; Krueger, K. B.; Gentle, I. R.; Meredith, P.; Burn, P. L. *Adv. Mater.* **2011**, *23*, 766-770.

Li, G.; Shrotriya, V.; Huang, J. S.; Yao, Y.; Moriarty, T.; Emery, K.; Yang, Y. *Nature Mater.* **2005**, *4*, 864-868.

Liang, Y. Y.; Xu, Z.; Xia, J. B.; Tsai, S. T.; Wu, Y.; Li, G.; Ray, C.; Yu, L. P. *Adv. Mater.* **2010**, *22*, E135- E138.

Ma, W. L.; Gopinathan, A.; Heeger, A. J. *Adv. Mater.* **2007**, *19*, 3656-3659.

Ma, W. L.; Yang, C. Y.; Gong, X.; Lee, K.; Heeger, A. J. *Adv. Funct. Mater.* **2005**, *15*, 1617-1622.

Malik, S.; Nandi, A. K. *J. Polym. Sci. B.* **2002**, *40*, 2073-2085.

Markov, D. E.; Amsterdam, E.; Blom, P. W. M.; Sieval, A. B.; Hummelen, J. C. *J. Phys. Chem. A* **2005**, *109*, 5266-5274.

Markov, D. E.; Tanase, C.; Blom, P. W. M.; Wildeman, J. *Phys. Rev. B* **2005**, *72*, 045217.

- Markov, D. E.; Tanase, C.; Blom, P. W. M.; Wildeman, J. *Phys. Rev. B: Condens. Matter.* **2005**, *72*, 6.
- Marks, R. N.; Halls, J. J. M.; Bradley, D. D. C.; Friend, R. H.; Holmes, A. B. J. *Phys.: Condens. Matter.* **1994**, *6*, 1379-1394.
- Masuda, H.; Fukuda, K. *Science* **1995**, *268*, 1466-1468.
- Mayer, A. C.; Scully, S. R.; Hardin, B. E.; Rowell, M. W.; McGehee, M. D. *Materials Today* **2007**, *10*, 28-33.
- Mayer, A. C.; Toney, M. F.; Scully, S. R.; Rivnay, J.; Brabec, C. J.; Scharber, M.; Koppe, M.; Heeney, M.; McCulloch, I.; McGehee, M. D. *Adv. Funct. Mater.* **2009**, *19*, 1173-1179.
- McCarthy, T. J. Private communication.
- Mihailetchi, V. D.; Koster, L. J. A.; Hummelen, J. C.; Blom, P. W. M. *Phys. Rev. Lett.* **2004**, *93*, 216601.
- Mihailetchi, V. D.; Xie, H. X.; de Boer, B.; Popescu, L. M.; Hummelen, J. C.; Blom, P. W. M.; Koster, L. J. A. *Appl. Phys. Lett.* **2006**, *89*, 012107.
- Moon, J. S.; Takacs, C. J.; Sun, Y.; Heeger, A. J., *Nano Lett.* **2011**, *11*, 1036-1039.
- Moon, S. I.; McCarthy, T. J. *Macromolecules* **2003**, *36*, 4253-4255.
- Moule, A. J.; Meerholz, K. *Adv. Mater.* **2008**, *20*, 240-245.
- Nishi, T.; Wang, T. T. *Macromolecules* **1975**, *8*, 909-915.
- Nunzi, J. M. *Comptes Rendus Physique* **2002**, *3*, 523-542.
- Osterbacka, R.; An, C. P.; Jiang, X. M.; Vardeny, Z. V. *Science* **2000**, *287*, 839-842.
- Park, S. H.; Roy, A.; Beaupre, S.; Cho, S.; Coates, N.; Moon, J. S.; Moses, D.; Leclerc, M.; Lee, K.; Heeger, A. J. *Nature Photon.* **2009**, *3*, 297-303.
- Park, S.; Lee, D. H.; Xu, J.; Kim, B.; Hong, S. W.; Jeong, U.; Xu, T.; Russell, T. P. *Science* **2009**, *323*, 1030-1033.
- Parnell, A. J.; Dunbar, A. D. F.; Pearson, A. J.; Staniec, P. A.; Dennison, A. J. C.; Hamamatsu, H.; Skoda, M. W. A.; Lidzey, D. G.; Jones, R. A. L. *Adv. Mater.* **2010**, *22*, 2444-2447.

- Peet, J.; Kim, J. Y.; Coates, N. E.; Ma, W. L.; Moses, D.; Heeger, A. J.; Bazan, G. C. *Nature Mater.* **2007**, 6, 497-500.
- Pivrikas, A.; Stadler, P.; Neugebauer, H.; Sariciftci, N. S. *Org. Electron.* **2008**, 9, 775-782.
- Prakasam, H. E.; Shankar, K.; Paulose, M.; Varghese, O. K.; Grimes, C. A. *Journal of Physical Chemistry C* **2007**, 111, 7235-7241.
- Rogers, J. T.; Schmidt, K.; Toney, M. F.; Kramer, E. J.; Bazan, G. C. *Adv. Mater.* **2011**, 23, 2284-2288.
- Russell, T. P.; Hadziioannou, G.; Warburton, W. K. *Macromolecules* **1985**, 18, 78-83.
- Samant, M. G.; Stohr, J.; Brown, H. R.; Russell, T. P.; Sands, J. M.; Kumar, S. K. *Macromolecules* **1996**, 29, 8334-8342.
- Sariciftci, N. S.; Braun, D.; Zhang, C.; Srdanov, V. I.; Heeger, A. J.; Stucky, G.; Wudl, F. *Appl. Phys. Lett.* **1993**, 62, 585-587.
- Sariciftci, N. S.; Smilowitz, L.; Heeger, A. J.; Wudl, F. *Science* **1992**, 258, 1474-1476.
- Shaheen, S. E.; Brabec, C. J.; Sariciftci, N. S.; Padinger, F.; Fromherz, T.; Hummelen, J. C. *Appl. Phys. Lett.* **2001**, 78, 841-843.
- Simon, J.; Andre, J. J. *Molecular Semiconductors: Photoelectrical Properties and Solar Cells*, Springer, **1985**.
- Sirringhaus, H.; Brown, P. J.; Friend, R. H.; Nielsen, M. M.; Bechgaard, K.; Langeveld-Voss, B. M. W.; Spiering, A. J. H.; Janssen, R. A. J.; Meijer, E. W.; Herwig, P.; de Leeuw, D. M. *Nature* **1999**, 401, 685-688.
- Sista, S.; Hong, Z. R.; Chen, L. M.; Yang, Y. *Energy & Environmental Science* **2011**, 4, 1606-1620.
- Spanggaard, H.; Krebs, F. C. *Sol. Energy Mater. Sol. Cells.* **2004**, 83, 125-146.
- Steinhart, M.; Wehrspohn, R. B.; Gosele, U.; Wendorff, J. H. *Angew. Chem. Int. Ed.* **2004**, 43, 1334-1344.
- Steinhart, M.; Wendorff, J. H.; Greiner, A.; Wehrspohn, R. B.; Nielsch, K.; Schilling, J.; Choi, J.; Gosele, U. *Science* **2002**, 296, 1997-1997.
- Stohr, J., *NEXAFS spectroscopy*. Berlin ; New York : Springer-Verlag: **1992**.

- Stohr, J.; Outka, D. A. *Phys. Rev. B.* **1987**, *36*, 7891-7905.
- Swaraj, S.; Wang, C.; Araki, T.; Mitchell, G.; Liu, L.; Gaynor, S.; Deshmukh, B.; Yan, H.; McNeill, C. R.; Ade, H. *Eur. Phys. J. Special Topics.* **2009**, *167*, 121-126.
- Swaraj, S.; Wang, C.; Yan, H. P.; Watts, B.; Jan, L. N.; McNeill, C. R.; Ade, H. *Nano Lett.* **2010**, *10*, 2863-2869.
- Sze, S. M.; Ng, K. K., *Physics of semiconductor device.* John. Wiley & Sons: New York, **1981**.
- Tai, Q. D.; Zhao, X. Z.; Yan, F. *J. Mater. Chem.* **2010**, *20*, 7366-7371.
- Tang, C. W. *Appl. Phys. Lett.* **1986**, *48*, 183-185.
- Thompson, B. C.; Frechet, J. M. J. *Angew. Chem. Int. Ed.* **2008**, *47*, 58-77.
- Treat, N. D.; Brady, M. A.; Smith, G.; Toney, M. F.; Kramer, E. J.; Hawker, C. J.; Chabinyk, M. L. *Adv. Energy Mater.* **2010**, *1*, 82-89.
- van Bavel, S. S.; Barenklau, M.; de With, G.; Hoppe, H.; Loos, J. *Adv. Funct. Mater.* **2010**, *20*, 1458-1463.
- van Bavel, S. S.; Sourty, E.; de With, G.; Loos, J. *Nano Lett.* **2009**, *9*, 507-513.
- Vaynzof, Y.; Kabra, D.; Zhao, L. H.; Chua, L. L.; Steiner, U.; Friend, R. H. *ACS Nano* **2011**, *5*, 329-336.
- Verploegen Eric ; Mondal Rajib ; Bettinger J. Christopher; Sok Seihout; Toney F. Michael; Zhenan, B. *Adv. Funct. Mater.* **2010**, *20*, 3519-3529.
- Wang, C.; Araki, T.; Ade, H. *Appl. Phys. Lett.* **2005**, *87*, 214109.
- Wang, C.; Araki, T.; Watts, B.; Harton, S.; Koga, T.; Basu, S.; Ade, H. *J. Vac. Sci. Technol., A.* **2007**, *25*, 575-586.
- Wang, C.; Garcia, A.; Yan, H. P.; Sohn, K. E.; Hexemer, A.; Nguyen, T. Q.; Bazan, G. C.; Kramer, E. J.; Ade, H. *J. AM. CHEM. SOC.* **2009**, *131*, 12538-12539.
- Wang, H. S.; Lin, L. H.; Chen, S. Y.; Wang, Y. L.; Wei, K. H. *Nanotechnology* **2009**, *20*, 075201.
- Wang, W. L.; Wu, H. B.; Yang, C. Y.; Luo, C.; Zhang, Y.; Chen, J. W.; Cao, Y. *Appl. Phys. Lett.* **2007**, *90*, 183512.

- Wang, X. J.; Ederth, T.; Inganas, O. *Langmuir* **2006**, *22*, 9287-9294.
- Wang, Y.; Gosele, U.; Steinhart, M. *Nano Lett.* **2008**, *8*, 3548-3553.
- Watts, B.; Belcher, W. J.; Thomsen, L.; Ade, H.; Dastoor, P. C. *Macromolecules* **2009**, *42*, 8392-8397.
- White, M. S.; Olson, D. C.; Shaheen, S. E.; Kopidakis, N.; Ginley, D. S. *Appl. Phys. Lett.* **2006**, *89*, 143517.
- Yan, H. P.; Swaraj, S.; Wang, C.; Hwang, I.; Greenham, N. C.; Groves, C.; Ade, H.; McNeill, C. R. *Adv. Funct. Mater.* **2010**, *20*, 4329-4337.
- Yang, X. N.; Loos, J.; Veenstra, S. C.; Verhees, W. J. H.; Wienk, M. M.; Kroon, J. M.; Michels, M. A. J.; Janssen, R. A. J. *Nano Lett.* **2005**, *5*, 579-583.
- Yao, Y.; Hou, J. H.; Xu, Z.; Li, G.; Yang, Y. *Adv. Funct. Mater.* **2008**, *18*, 1783-1789.
- Yoo, P. J.; Lee, H. H. *Macromolecules* **2005**, *38*, 2820-2831.
- Yoriya, S.; Paulose, M.; Varghese, O. K.; Mor, G. K.; Grimes, C. A. *Journal of Physical Chemistry C* **2007**, *111*, 13770-13776.
- Yu, G.; Gao, J.; Hummelen, J. C.; Wudl, F.; Heeger, A. J. *Science* **1995**, *270*, 1789-1791.
- Zhang, M. F.; Dobriyal, P.; Chen, J. T.; Russell, T. P.; Olmo, J.; Merry, A. *Nano Lett.* **2006**, *6*, 1075-1079.
- Zhao, W.; Chen, D.; Hu, Y. X.; Grason, G. M.; Russell, T. P. *ACS Nano*. **2011**, *5*, 486-492.
- Zhao, Y.; Xie, Z. Y.; Qu, Y.; Geng, Y. H.; Wang, L. X. *Appl. Phys. Lett.* **2007**, *90*, 043504.